Aix*Marseille université
Initiative d'excellence

THÈSE DE DOCTORAT

Soutenue à Aix-Marseille Université
le 19 juillet 2021 par

Adrien GANS

Rheology of cohesive powders : Experiments and modelisation

Spécialité
Mécanique et physique des fluides

École doctorale
ED 353 - Sciences pour l'ingénieur

Laboratoire IUSTI
Institut Universitaire des Systèmes Thermiques et Industriels

Composition du jury

Sébastion Kiesgen de Richter Université de Lorraine	Rapporteur
Pierre Rognon Sydney University	Rapporteur
Marie-Caroline Jullien Université de Rennes - CNRS	Examinatrice
Thierry Faug INRAé	Examinateur
Frédéric Restagno Université Paris-Saclay - CNRS	Président du jury
Lydie Staron Sorbonne Université - CNRS	Examinatrice
Maxime Nicolas Aix-Marseille Université	Directeur de thèse
Olivier Pouliquen Aix-Marseille Université - CNRS	Directeur de thèse
Alban Sauret UC Santa Barbara	Invité

I, undersigned, Adrien Gans, hereby declare that the work presented in this manuscript is my own work, carried out under the scientific direction of Maxime Nicolas and Olivier Pouliquen, in accordance with the principles of honesty, integrity and responsibility inherent to the research mission. The research work and the writing of this manuscript have been carried out in compliance with both the french national charter for Research Integrity and the Aix-Marseille University charter on the fight against plagiarism.

This work has not been submitted previously either in this country or in another country in the same or in a similar version to any other examination body.

Marseille, 05/31/2021

Résumé

Mots clés : Milieux granulaires, poudres, cohésion

Les milieux granulaires constituent une des ressources primaires les plus utilisées dans le monde, particulièrement dans l'industrie. Parmi la diversité de matériaux granulaires existants, les poudres cohésives constituent l'un des matériaux les plus délicats à manipuler. Comprendre le comportement de ces poudres en écoulement et développer des outils adaptés à leur manipulation constitue donc un enjeu industriel majeur. Cependant la difficulté d'étudier ces poudres cohésives réside dans la diversité des interactions cohésives entre les grains qui les composent. Dans le but de comprendre les effets de la cohésion sur les écoulements de poudres, une première étape consiste donc à concevoir un milieu cohésif modèle dont on peut contrôler la cohésion, et qui soit peu sensible aux conditions expérimentales. Le travail proposé dans cette thèse est de développer des méthodes permettant de caractériser et quantifier la cohésion inter-particules ainsi que la cohésion macroscopique d'un milieu granulaire cohésif modèle (CCGM), puis de concevoir des dispositifs expérimentaux permettant d'étudier le comportement du CCGM en écoulement. Les résultats expérimentaux seront comparés à des résultats obtenus grâce à des simulations numériques, basées sur un modèle de rhéologie granulaire continue à laquelle une contrainte seuil de mise en écoulement dépendante de la cohésion est ajoutée, réalisées par Pierre-Yves Lagrée et Anaïs Abramian, ainsi que des simulations de dynamiques des contacts réalisées par Lydie Staron et Sandip Mandal. La pertinence de cette modélisation continue sera discutée à travers les chapitres. Dans le chapitre 1 nous proposons une description de l'état des connaissances concernant les écoulements de milieux granulaires et de poudres. En particulier nous présentons une synthèse des connaissances actuelles sur les différents dispositifs expérimentaux utilisés pour étudier les milieux granulaires cohésifs.

Concernant l'élaboration d'un milieu granulaire cohésif modèle, dans le chapitre 2 nous présentons le processus de fabrication du CCGM, ainsi que les différentes méthodes utilisées pour quantifier la cohésion de ce milieu à l'échelle des grains aussi bien qu'à l'échelle macroscopique. Nous avons montré que la cohésion du CCGM n'est pas affectée par la température ou l'humidité environnante, les propriétés cohésives semblent rester stables sur une durée de 6 mois et nous avons également caractérisé l'effet de la cohésion sur la compacité.

Dans le chapitre 3 nous présentons les conditions nécessaires pour éroder les grains présents à la surface d'un lit de grains cohésifs par un jet d'air orienté perpendiculairement au lit granulaire. Nous avons montré qu'une expérience d'érosion d'un lit

granulaire cohésif permet de mesurer finement la cohésion inter-particules.

Dans le chapitre 4 nous étudions la vidange de silo d'un milieu granulaire cohésif. Une première étude nous a permis de déterminer d'abord le seuil d'écoulement du CCGM à travers l'orifice d'un silo axisymétrique, puis une première estimation de l'effet de la cohésion sur le débit de vidange. Une seconde étude sur le champ de vitesse du milieu granulaire à la sortie d'un silo rectangulaire a montré que l'effet de la cohésion sur la vidange modifie essentiellement la vitesse de sortie du matériau et non sa dilatance.

Le chapitre 5 présente les résultats d'expériences d'effondrements de colonnes granulairescohésives. Nous avons étudié la rupture de colonnes en fonction de leur hauteur et de la cohésion du milieu. Il semble qu'il est possible d'expliquer l'angle de rupture par un calcul de stabilité de la colonne et d'estimer la proportion de grains qui restent statiques. Les mesures d'étalement du CCGM lors de la chute sont comparées avec des simulations numériques continues. Nous avons montré qu'une rhéologie $\mu(I)$ cohésive capture correctement la tendance de l'étalement. Toutefois un travail plus fin sur l'effet de la cohésion sur les paramètres de la rhéologie semble nécessaire.

Enfin le chapitre 6 présente les futures projets en cours, ou envisagées, sur chacun des dispositifs expérimentaux utilisé dans cette thèse, ainsi que des résultats préliminaires concernant la rhéologie du CCGM.

Abstract

Keywords: Granular materials, powders, cohesion

Granular media is one of the most widely used primary resources in the world, particularly in industry. Among the diversity of existing granular materials, cohesive powders are one of the more challenging material to handle. Understanding the behaviour of these powders and developing adapted tools to their handling is therefore a major industrial challenge. However, the difficulty of studying these cohesive powders lies in the diversity of cohesive interactions between the grains. In order to understand the effects of cohesion on powder flows, a first step is to design a model cohesive medium whose cohesion can be controlled and which is weakly sensitive to experimental conditions. The work proposed in this thesis is to develop methods to characterize and quantify the inter-particle cohesion as well as the macroscopic cohesion of a model cohesive granular medium (CCGM), and then to design experimental devices to study the flow behaviour of the CCGM. The experimental results will be compared to results obtained through numerical simulations, based on a model of continuous granular rheology enhanced with a yield stress, carried out by Pierre-Yves Lagrée and Anaïs Abramian, as well as contact dynamics simulations by Lydie Staron and Sandip Mandal.

In Chapter 1 we provide a description of the state of knowledge regarding granular media and powder flows. In particular, we present a synthesis of the current knowledge on the different experimental devices used to study cohesive granular media.

Regarding the development of a model cohesive granular medium, in Chapter 2 we will present the manufacturing process of the CCGM, and the different methods used to quantify the cohesion of this medium at the grain scale as well as at the macroscopic scale. We showed that the cohesion of the CCGM is not affected by the surrounding temperature or humidity, the cohesive properties seem to remain stable over a 6 month period and we also characterized the effect of cohesion on the volume fraction.

In Chapter 3 we investigate the condition of erosion of the grains present on the surface of a bed of cohesive grains by an air jet oriented perpendicularly to the granular bed. We have shown that an erosion experiment of a cohesive granular bed allows to measure finely inter-particle cohesion.

In Chapter 4, we study the discharge of a silo filled with a cohesive granular medium. A first study allowed us to first determine the threshold of flowability of the CCGM through the orifice of an axisymmetrical silo as a function of the cohesion, then the measure of the flow rate during the discharge provides an initial estimate of the effect of cohesion on the flow. A second study on the velocity field of the granular medium

at the outlet of a rectangular silo showed that the effect of cohesion on the flow rate essentially modify the velocity of the material and has little to no effect on its dilatancy.

Chapter 5 presents the results of cohesive granular column collapse experiments. We studied the rupture of columns according to their height and their cohesion. It appears that it is possible to predict the fracture angle a stability criterion and estimate the proportion of grains that remain static. The column spread measurements during the fall are compared with continuous numerical simulations. We have shown that a $\mu(I)$ rheology enhanced with a yield stress correctly captures the spreading trend. However, a more detailed work on the effect of cohesion on rheology parameters seems necessary to capture the final state of the collapse.

Finally, Chapter 6 presents a summary of the future projects underway, or planned, on each of the experimental devices presented in this thesis, as well as preliminary results concerning the rheology of the CCGM.

Remerciements

Pour commencer je souhaiterais remercier mes directeurs de thèse, Maxime Nicolas et Olivier Pouliquen, pour leur soutien sans faille durant ces trois années. Maxime, merci d'avoir toujours anticipé aussi bien les aspects pratiques que les aspects scientifiques de la thèse. Olivier, merci de toujours avoir pris le temps de m'expliquer même les aspects les plus simples des sujets que nous avons abordé. Merci, à vous deux, de toujours avoir trouvé le temps de discuter lorsque j'en avais besoin malgré les circonstances. Je retire énormément des discussions que nous avons eu, autant sur le plan scientifique que personnel, votre pédagogie, votre rigueur et votre bienveillance resterons des sources d'inspiration pour moi.

Je voudrais aussi remercier les membres de mon jury de thèse : Sébastien Kiesgen De Richter et Pierre Rognon pour avoir accepté d'être rapporteurs, ainsi que Lydie Staron, Marie-Caroline Jullien, Frédéric Restagno, et Thierry Faug pour avoir accepté de faire partie de mon jury. J'apprécie grandement l'intérêt qu'ils et elles portent à ce travail de recherche et c'est avec le même intérêt que j'accueillerai leurs commentaires. Je remercie également Alban Sauret, d'abord pour m'avoir accompagné durant ma recherche d'un contrat de thèse depuis le master, puis pour m'avoir proposé une collaboration sur les sujets d'érosion et d'effondrement de colonnes cohésives. J'ai eu énormément de chance de le rencontrer et c'est avec plaisir que nous l'invitons à cette soutenance.

Je souhaiterais remercier Blanche Dalloz et Pascale Aussillous pour m'avoir énormément aidé durant cette thèse, notamment sur la vidange de silo, ainsi que Laurence Bergougnoux pour avoir toujours pris le temps de m'expliquer le fonctionnement de Polytech. Je tiens également à remercier Sandip Mandal pour toutes les discussions que nous avons eu et qui m'ont permis d'appréhender mon sujet de thèse. Merci plus généralement à l'équipe GEP du laboratoire, Henri, Yoël, Geoffroy, Joël, Bloen, vous êtes tous plus passionnant les uns que les autres.

Je remercie également l'ensemble des doctorants et post doctorants du laboratoire, Nina, Hamza, Alice, Nabila, Joris, Houssine, Naima, Enrico, Alain, Arnaud, Gabriel, Marie, Nikhil, Sanjeev, Jordan, Valentin, Jeong-Un, Chico, Ignacio, Bruno, Davide et toutes celles et ceux que j'oublie sûrement. Merci pour votre bonne humeur, votre soutien et votre amitié. Tout particulièrement je souhaiterais remercier Franco Tapia. Franco, cette thèse te dois énormément, tu as pratiquement été un troisième directeur de thèse pour moi, et ton amitié, ta bonne humeur et ta persévérance ont été une source de motivation durant ces trois ans.

Je dois évidemment remercier Anaïs Abramian et Pierre-Yves Lagrée pour leur aide sur les simulations numériques. Merci pour votre gentillesse et votre patience. Merci

Pierre-Yves d'avoir pris de ton temps pour discuter des silos et des collapses, et merci Anaïs pour tout le travail que tu as fourni sur le collapse, cette thèse te dois aussi énormément. Merci aussi aux différents membres du projet Coprint, Lydie Staron, Sébastien Pinson et Jean-Michel Drouin. Nos réunions ont été peu nombreuses mais toujours fructueuses.

J'exprime également toute ma reconnaissance aux stagiaires avec lesquels j'ai pu travailler, Amina Abbedou, Meriem Settaoui et Mingze Gong, vous m'avez tous bien aidé.

Je remercie aussi le personnel administratif de l'IUSTI, Elisabeth et Audrey pour leur aide concernant les voyages et conférences, ainsi que Pascal, le secrétaire de l'école doctorale, pour avoir été d'une aide inestimable pour tout les doctorants du laboratoire.

Enfin je souhaiterais remercier mes proches. Mes parents, mon frère et ma soeur, qui m'ont toujours soutenus. Et bien sûr je ne pourrais jamais assez remercier Mélanie, ma femme, qui est le meilleur soutien dont je puisse rêver. Pour finir je remercie ma fille, Diana, qui, depuis sept mois, me permet de rester éveillé tard dans la nuit pour travailler sur ce manuscrit.

Contents

List of Figures

Introduction

The comprehension of the physical properties of granular media is a broad field of research that encompasses several research areas. Understanding their behavior has various implications for the description of natural phenomena and industrial processes. For instance, particles are involved in geophysics to understand pyroclastic flows and sedimentation. Granular materials are used in material science and engineering to develop building materials, and in food and pharmaceutical industries to handle cereals and medicines. Since divided media constitute the second most used resource worldwide, after water, any improvement on the physical cost to handle it would have an important repercussion on many fields of applications.

Among all divided media, powders are particularly challenging to handle. Indeed, due to the small size of the particles composing it, powders tend to disperse in the surrounding air, form aggregates, and seem to flow randomly. Whereas our understanding of granular materials has improved significantly over the last 40 years, the behavior of powders remains elusive. In order to describe the ease of handling different types of powders, several tools and measurement methods have been developed to characterize the ability of a powder to compact and flow. However, most of these tools mostly rely on empirical parameters. All suffer from the same issue: there is no model powder to study the diversity of powder behaviour. This lack of knowledge and the necessity to improve the management of industrial powders require studying more deeply the physics of cohesive powders to develop tools that could be used to describe the flowability of powders, *i.e.* the ability of a powder to flow.

This PhD thesis is part of the ANR Cohesive Powders Rheology: Innovative Tools (Coprint) project, which regroups three research teams in three laboratories : Pierre-Yves Lagrée and Lydie Staron at The Institut Jean Le Rond d'Alembert in Paris, Sébastien Pinson and Jean-Michel Drouin at Saint-Gobain Research (SGR) Provence in Cavaillon, Maxime Nicolas, Blanche Dalloz and Olivier Pouliquen at the Institut Universitaire des Systèmes Thermiques et Industriels (IUSTI) in Marseille. The purpose of this project is to develop innovative tools to characterize powders. The project is composed of an experimental part where the objective is to develop and characterize a cohesion-controlled granular material that would model the behavior of cohesive powder, and perform experiments to test its flowing behavior in canonical configurations. These results would then be compared with continuous and discrete numerical simulations. The numerical part of the project, listed by Pierre-Yves Lagrée and Anaïs Abramian at Institut d'Alembert, consist in implementing a cohesive granular rheology in a continuous numerical simulation and compare it with experiments and discrete numerical simulations performed by Sandip Mandal and Lydie Staron.

The specific purpose of this PhD is to continue the work initiated by Maxime Nicolas and interns Ines Basses and Davide Di Giusto: the characterization of the cohesive properties of a new cohesion-controlled granular material developed at IUSTI. The second goal is to perform experiments to test and describe the rheology of this cohesive granular material. The results presented in this thesis are organized in 5 chapters. First a state of knowledge about granular materials and powders is presented in chapter 1. Then chapter 2 presents the methods of fabrication of the cohesion-controlled granular material developed at IUSTI. This chapter also reports the experiments performed to measure the bulk cohesion, the inter-particles cohesion, the friction coefficient and the volume fraction. Results regarding the erosion of the cohesive materials are presented in chapter 3. These first results constitute the first steps toward the comprehension of a flowability threshold at the particle scale of the cohesive granular material. Chapter 4 focuses on the discharge of cohesive grains from an axisymmetric silo and a rectangular quasi-2D silo. The study of the flow through the outlet of an axisymmetrical silo provides results on the threshold of flowability and an understanding of the flow behavior of cohesive granular materials. Then, Particle-image-velocimetry (PIV) performed at the outlet of the quasi 2D silo brings a new insight to understand the behavior of flowing cohesive granular materials. Chapter 5 considers the collapse of a cohesive granular column. First, the stability conditions of the cohesive column are investigated, then the spreading dynamics of the grains and the final state of the collapsed material are analysed in detail. This configuration is compared to continuous numerical simulations performed by Anaïs Abramian at Institut d'Alembert and provides an investigation on the cohesive granular rheology and a bulk flow threshold. More specifically, this configuration is used to focus on the frictional and cohesive behavior of the granular material. Finally, chapter 6 provides a summary of the investigations performed on the effect of cohesion on the behavior of cohesive granular materials, and opens new perspectives to study the rheology of the CCGM.

1 State of the art

In this chapter, we present a brief description of the state of knowledge concerning granular media, powders, and cohesive granular materials.

1.1 Granular media

1.1.1 Definition of a granular medium

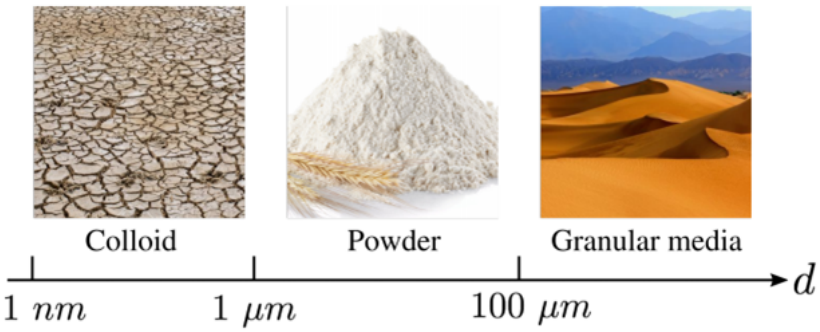

Figure 1.1 – Classification of granular materials as a function of the particle size.

Divided media correspond to an assembly of microscopic solid particles and exist in different aspects and shapes. They cover a broad category of materials from colloids (mud, paint) to granular media (sand, boulders, rings of Saturn), and can be classified by the particle size as shown in Fig. 1.1.

A granular medium is usually composed of solid particles larger than 100 µm [1, 2, 3, 4, 5, 6]. This classification corresponds to the limit where physical phenomena cannot be neglected as the particles become smaller. Usually, granular media are mostly governed by friction and contact forces. In this case moisture, Van der Waals interactions, and thermal agitation are negligible, but this is not the case for powders like flour [7].

Granular media are part of our daily life and are present in many industrial sectors. for instance, they are used in the chemical industry, cereal, and mining industries. Overall we estimate that granular materials are involved in more than 50% of all products sold worldwide [8], and are the second most used material in the industry after water [4]. Granular materials are also involved in a wide range of natural phenomena. The first example that comes to mind is the sand dunes, but describing the behavior of such

material is also needed to understand and model scree, pyroclastic flows, landslides, and snow avalanches. because of their wide range of industrial use and implication in geophysics, numerous studies have been carried out since the last century to establish the constitutive laws describing the behavior of granular media in different situations, from the simple sand pile to complex flows. In the following parts, we will present the different quantities that can be used to describe the behavior of granular materials.

1.1.2 Description of granular media

The first observation about granular media is the variety of behaviors obtained depending on the external solicitation [9] as illustrated in Fig. 1.2(a) where three different regions are observed by pouring grains on a pile of particles. The first region, at the bottom of the pile behaves as a solid : the grains are packed and motionless. The second region, above the solid region, is a dense granular flow which can be compared to a liquid. The third region at the surface is a gas-like region where the motion of the particles is not impeded by their close neighbour. From this behavior, we can assume that there is a condition of stability for a pile of grains to remain still, which implies that, above a certain pile angle, an avalanche is triggered and the grains start to flow. This maximal angle, called the angle of repose θ_c, is illustrated in Fig. 1.2(b). By analogy with the problem of a frictional block placed on an inclined plane, where the block slides when the inclination angle reaches a critical value, we can define a friction coefficient of the granular material $\mu_s = \tan\theta_c$. Therefore the stability criterion of a granular medium is frictional, and related to the maximum angle of repose of a sand pile. However, when the material starts to flow above this angle, the stress depends on the shear rate and cannot be described by a Coulomb's law.

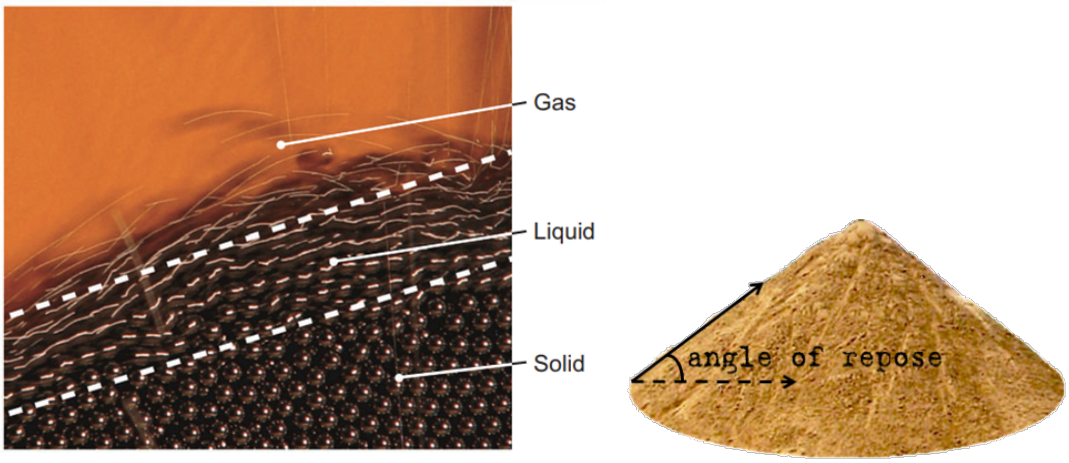

(a) (b)

Figure 1.2 – (a) The different states of granular media, extracted from Forterre *et al.* [10]. (b) A sand pile showing the definition of the angle of repose.

Another remarkable property of granular media is the ability to occupy more or less volume depending on the size and shape of the grains [11]. Moreover, the ability to dilate or compress depending on the applied stress and the initial disposition of the particles implies that the volume fraction, $\phi = V_p/V_{tot}$, with V_p the volume taken by the grains and V_{tot} the total volume of the system, is another parameter needed to fully describe the granular media. Several studies were performed to determine the value of ϕ depending on the nature of the particles used, and a large set of numerical simulations and experiments have shown that the random packing of monodispersed spheres is around $\phi = 0.59$ and can vary from random loose packing ($\phi = 0.55$) to random close packing ($\phi = 0.64$) [12, 13, 14, 15, 16].

From the apparent simplicity to describe a granular medium and the effective complexity to understand its flow behavior emerged the need to develop some tools to establish a rheology of granular media.

1.1.3 Rheology of granular media

Let us consider a plane shear flow of grains, as shown in Fig. 1.3(a). In this configuration, the spherical particles of diameter d and density ρ_p are sheared between two plates separated by a gap L. The bottom plate is motionless while the top plate imposes a pressure P and a velocity V. The roughness at the top and bottom plates ensures a no-slip boundary condition, and the shear rate $\dot{\gamma}$ is therefore V/L.

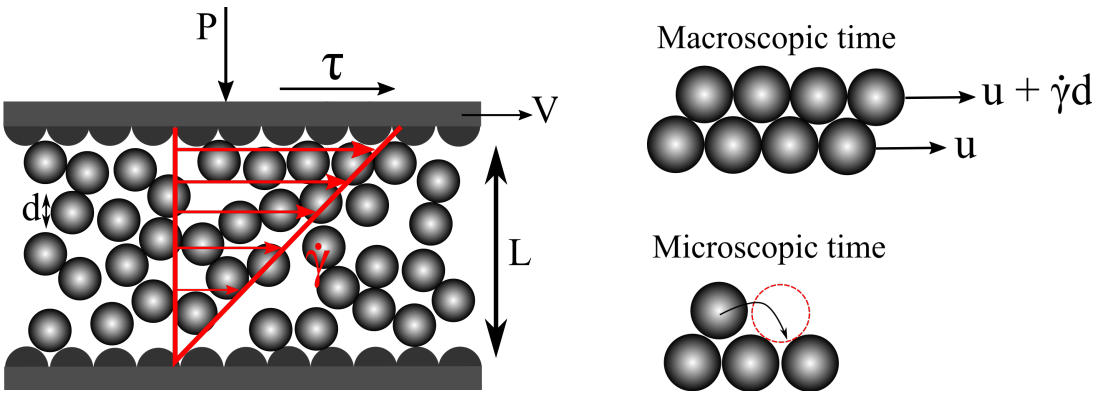

Figure 1.3 – (a) Plane shear flow setup. (b) Physical interpretation of the inertial number I as the ratio between the macroscopic time of deformation and the microscopic time of rearrangement due to confinement pressure, extracted from Andreotti *et al.* [6].

The possible motion of particles during the flow in absence of gravity are illustrated in Fig. 1.3(b). On one hand, we can see the flow of the granular material as a macroscopic deformation, and consider the characteristic time of deformation as $t_{macro} = 1/\dot{\gamma}$. On the other hand the characteristic time needed for a grain to fall

in the void between two of its bottom neighbours due to the confining pressure is $t_{micro} = d/\sqrt{P/\rho}$.

In this configuration, Da Cruz *et al.* [17] and Iordanov *et al.* [18] have shown that there is a single dimensionless number describing this system, called the inertial number I, corresponding to the ratio of t_{macro} and t_{micro} :

$$I = \frac{\dot{\gamma} d}{\sqrt{P/\rho_p}} \tag{1.1}$$

This dimensionless number describes the ability of a granular medium to flow under a shear stress and a confining pressure. The inertial number is sufficient to characterise and classify most of the flow regimes of granular media. Typically, a small value of $I < 10^{-3}$ is considered as a quasi-static regime, while $I > 0.1$ is considered as an inertial regime. This dimensionless number being the only one controlling the flow of granular media, the dimensional analysis gives the relation between the normal stress P and tangential stress τ, and also implies that the volume fraction ϕ only depends on the inertial number I, as follows :

$$\tau = \mu(I)P \tag{1.2}$$

and

$$\phi = \phi(I) \tag{1.3}$$

Therefore, μ can be interpreted as a friction coefficient of the granular material that depends on I. As can bee seen in Fig. 1.4(a)-(b), an increase in I leads to an increase in μ and a decrease in ϕ.

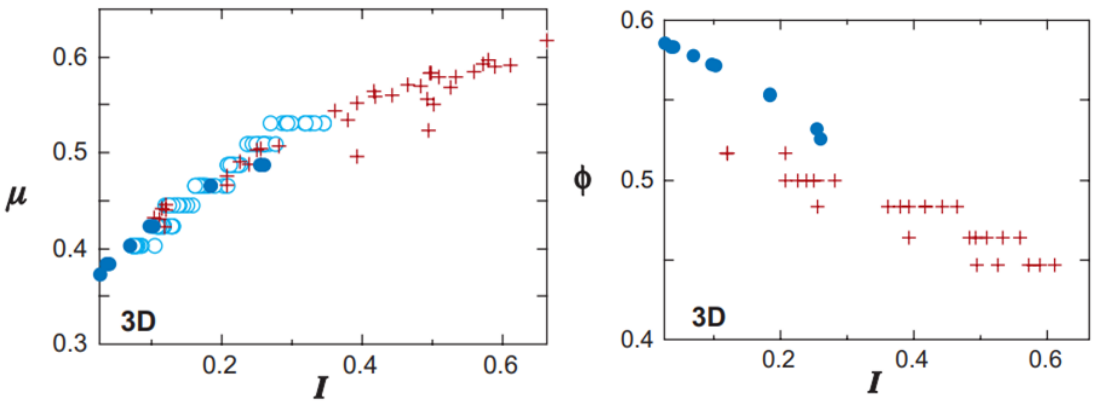

(a) (b)

Figure 1.4 – (a) Friction coefficient μ and (b) Volume fraction ϕ as a function of the inertial number I in three configurations : inclined plane experiments (∘), inclined plane simulation (•) and planar shear experiments(+), extracted from Forterre *et al.* [10].

Several authors have tried to fit an empirical expression for $\mu(I)$ and $\phi(I)$ [19, 20, 21, 22, 23]. The common accepted expressions are the following :

$$\mu(I) = \mu_s + \frac{\mu_2 - \mu_s}{I_0/I + 1} \tag{1.4}$$

and

$$\phi(I) = \phi_{max} - (\phi_{max} - \phi_{min})I \tag{1.5}$$

where μ_s, μ_2, I_0, ϕ_{max}, and ϕ_{min} are coefficients that depends on the material properties. For spherical monodisperse glass beads, we have $\mu_s = 0.4$, $\mu_2 = 0.65$, $I_0 = 0.3$, $\phi_{max} = 0.64$ and $\phi_{min} = 0.4$ [12, 24, 25, 26]. The value of μ_2 corresponds to the saturation of $\mu(I)$ for large value of I, typically $I > 0.5$, and often the difference between μ_2 and μ_s is noted $\Delta\mu = \mu_2 - \mu_s$. Later, Jop *et al.* [27] proposed a generalisation of the friction law for 3D flows. For a dense flow, the variations of the volume fraction can be considered negligible, therefore they assumed an incompressible flow, and an isotropic pressure leading to the relationship between the stress tensor σ_{ij} and the strain tensor τ_{ij} :

$$\sigma_{ij} = -P\delta_{ij} + \tau_{ij}, \tag{1.6}$$

with

$$\tau_{ij} = \eta_{eff}\dot{\gamma}_{ij}, \tag{1.7}$$

and

$$\eta_{eff} = \frac{\mu(I)P}{|\dot{\gamma}|}. \tag{1.8}$$

In these expressions, $\dot{\gamma}_{ij} = \partial u_i/\partial x_j$ is the strain rate tensor and $|\dot{\gamma}| = \sqrt{\frac{1}{2}\dot{\gamma}_{ij}\dot{\gamma}_{ij}}$ is the second invariant of the strain rate tensor. Hence, the dense flow of a granular medium can be described as the flow of a non-Newtonian visco-plastic fluid with an effective viscosity η_{eff} which depends on the pressure and the shear rate. As we will see in the next sections, this rheology has been successfully applied in various configurations to simulate or describe some complex granular flows [23]. For example, it was used to describe surface waves in a flow on an inclined plane [28], granular flows on a heap [22, 23], granular collapse [26, 29] and the discharge of silos [25, 30, 31]. Despite the strength of this approach, several questions remain concerning the description of the granular flows. Indeed, the start and stop of the flows are not well described by this model, as well as non-local effects, partially because one hypothesis of this model is the weak influence of the volume fraction on granular flows, which is relevant for dense flows, but not sufficient for dilated flows. Other approaches tried to introduce these missing elements, as described, for instance, by Pouliquen *et al.* [32] and Kamrin *et al.* [33] for a non-local rheology, and Borzonyi *it al.* [34] for diluted flows.

Despite these limitations, the past successes of the $\mu(I)$ rheology in various flows configurations support its use as a good description of the rheology of powders. However, this rheology must be modified to take account of the cohesion, which is not

negligible in the case of cohesive powders.

1.2 Powders

While granular media, like sand or ore are one of the most used material on Earth, powders also constitute a major part of the industrial use worldwide. Indeed, powders are widely used in the pharmaceutical industry (lactose powders, aggregates for tablets), in metallurgy, surface cleaning (baking soda), water treatments (chlorine), and food industry (flour). Considering the huge importance of powders, various studies have tried to describe their static and flowing behavior to improve our technique of storage and handling. While some studies focused on a statistical approach of powders behavior to define their entropy and cohesion energy linked to volume fraction and size of aggregates [35, 36], other studies have tried to characterise the macroscopic properties of powders: angle of repose, volume fraction, cohesion and flowing properties [1, 37, 38].

The lower size limits of 1 µm for the powder domain is not arbitrary. Usually, colloids are considered to be submitted to thermal agitation while powders are not [7]. considering a sphere of density ρ_g and radius r_g submitted to gravity at $T = 300K$ leads to a potential energy associated to a vertical displacement of order r_g equal to $E_p = (8\pi/3)\rho_g r_g^4$. This potential energy can be compared to the thermal energy $E_{th} = (3/2)k_b T$ where $k = 1.38.10^{-23}$ m^2.kg.s^{-2}.K^{-1} is the Boltzmann constant. The minimum radius for a particle to not be submitted to thermal agitation is then given by considering that $E_p = E_{th}$ and gives :

$$r_{th} = \left(\frac{9k_b T}{16\pi\rho_g g}\right)^{1/4} \sim 0.4\mu\text{m}, \tag{1.9}$$

for a glass particle of density $\rho_g = 2500$ kg.m^{-3}. The threshold at $d = 1$ µm between powders and colloids is therefore based on the physical parameter r_{th} which describes the effect of thermal agitation on particles.

Whereas powders are not submitted to thermal agitation, they are submitted to other interactions that are negligible for granular media. Indeed, whereas friction is the main interaction in granular media, powder particles are small enough to be submitted to inter-particle cohesive interactions. Some consequences can be visualized in Fig. 1.5. Whereas a sand pile tends to have a smooth surface and a well-defined angle of repose, powders may have a rough surface, a hardly definable angle of repose, and may be composed of aggregates.

(a) (b)

Figure 1.5 – (a) Sand pile and (b) Cacao powder pile

1.2.1 Different types of interactions

1.2.1.1 Van der Waals interaction

Even for dry, non-charged grains, an inter-particle attractive interaction exists due to atomic interactions. Various studies aimed at describing the forces involved for objects in contact (Van der Waals, dipole interactions, etc...)[39, 40, 41, 42, 43, 44].

Let us consider two identical elastic spheres of radius R, brought in contact by an external force F_{ext} (see Fig. 1.6) placed in a vacuum. Due to the balance between an elastic repulsive force F_{el} at small range and an attractive force F_{adh} at larger range, there is an equilibrium position for the spheres corresponding to an interpenetration length δ and a contact surface of radius a. A small displacement $\mathrm{d}\delta$ implies a variation of the contact surface $\mathrm{d}S = \mathrm{d}(\pi a^2)$, and thus a variation of the surface energy $\mathrm{d}E_{surf} = 2\gamma_S \mathrm{d}(\pi a^2)$, where γ_S is the solid-vacuum surface tension. Since the energy variation is the force work on a distance $\mathrm{d}\delta$, the change of surface energy also writes $\mathrm{d}E_{surf} = 2F_{adh}\mathrm{d}\delta$. By using the approximation of small deformations $a \sim 2\delta R$ [6, 45], the adhesion force scales as:

$$F_{adh} \sim \gamma_S R \tag{1.10}$$

It is noticeable that the adhesive force does not depend of the elastic properties of the spheres, but only on their radii. While this approach is relevant to understand the physical origin of the adhesive force observed for powders, it does not take into account other effects like the interaction of the surfaces close to the contact area or the local elastic deformations due to the forces involved.

The adhesion force between two identical spheres is shown to be constrained between two values [46, 47, 48] :

$$\frac{3}{2}\pi\gamma_S R < F_{adh} < 2\pi\gamma_S R \tag{1.11}$$

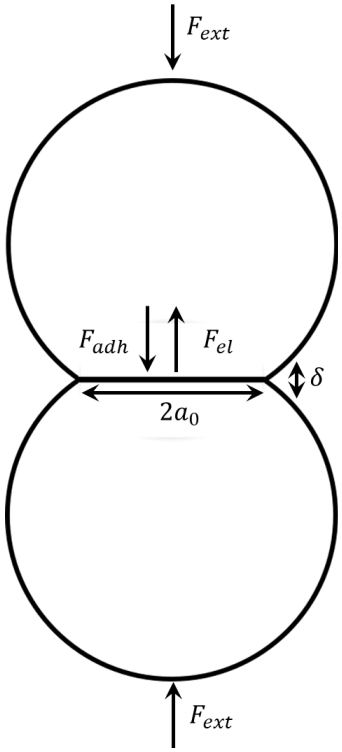

Figure 1.6 – Two elastic sphere in contact.

The lower limit of $3\pi\gamma R/2$ corresponds to the Johnson-Kendall-Robert (JKR) model [49] while the upper limit of $2\pi\gamma R$ correspond to the Derjaguin-Muller-Toporov (DMT) model [42]. To connect the two limits, Tabor [50] and Maugis [51] showed that the JKR limit corresponds to soft spheres while the DMT limit corresponds to rigid spheres. The transition between the two limits depends on the ratio δ^*/a_0 where δ^* is the length of the elastic deformation close to the contact surface, and a_0 is the range of the molecular interactions. Typically, the limit $\delta^*/a_0 << 1$ corresponds to a small elastic deformation and a long range of molecular interaction, therefore rigid spheres, while $\delta^*/a_0 >> 1$ corresponds to a large length of elastic deformation and a short range of molecular interactions, and therefore soft spheres.

A method to estimate the value of γ_S is to consider the energy of interaction of two planar surfaces separated by a distance s. Let us consider the interaction between two molecules separated by a distance r. The energy of interaction between these two molecules writes $w(r) = -C/r^6$ where C is a constant that depends on the molecules considered [52]. The energy of interaction w_{pw} per surface unit between a single molecule and a semi-infinite surface located at a distance s and having a molecular density ρ (see Fig. 1.7) is the sum of every interactions between the molecule and a volume $\mathrm{d}v = \mathrm{d}z\mathrm{d}x$ of the surface :

$$w_{pw}(s) = \int_{swall} -\frac{C}{r^6}\rho \mathrm{d}v = \int_{z=s}^{\infty}\int_{x=0}^{\infty} -\frac{C}{(x^2+z^2)^3}\rho 2\pi \mathrm{d}x\mathrm{d}z = -\frac{\pi\rho C}{6s^3} \tag{1.12}$$

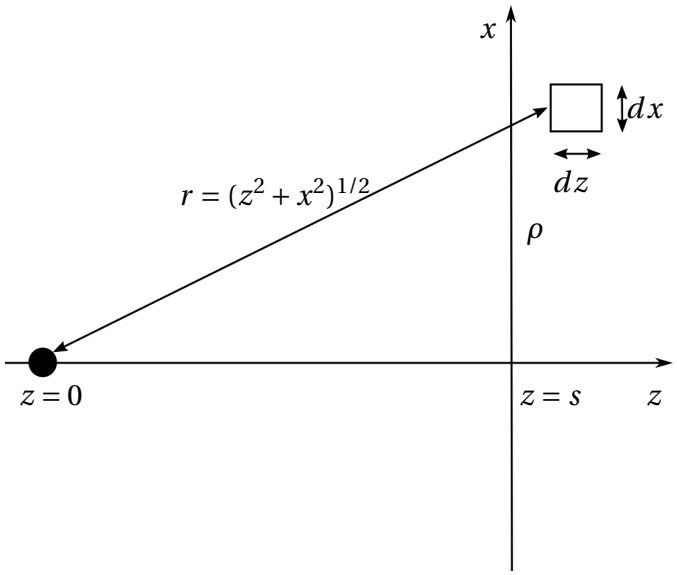

Figure 1.7 – Schematic of the Van der Waals interaction between a single molecule with a surface at a distance s.

The energy of interaction per unit length, w_{ww}, for two semi-infinite planar surfaces of molecular density ρ separated by a distance s then writes :

$$w_{ww} = \int_{z=s}^{\infty} -\frac{\pi\rho C}{6z^3}\rho dz = -\frac{\pi C\rho^2}{12s^2} = -\frac{A}{12\pi s^2} \tag{1.13}$$

where $A = \pi^2\rho C$ is the Hamaker constant [40]. Taking the distance s equal to the molecular distance s_{mol}, this energy per length unit corresponds to the energy needed to create two surface *i.e.* $-2\gamma_S$. This leads to an expression for the surface tension $\gamma_S = A/24\pi s_{mol}^2$. Using equation (1.10), we obtain an expression for the Van der Waals force $F_{VdW} = AR/12s^2$. The typical order of magnitude of s and A are usually taken as $s \sim R/100$, and $A \sim 10^{-19}$ J respectively. The Van der Waals force can then be compared to the weight of a particle $F_W = (4/3)\pi\rho_g g {r_g}^3$ and the radius satisfying the condition is given by:

$$r_{VdW} = \left(\frac{100A}{16\pi\rho_g g}\right)^{1/4} \simeq 5.3\mu\text{m} \tag{1.14}$$

Therefore, it seems relevant to take $r_g = 100\,\mu$m as the limit where Van der Waals forces are negligible compared to the weight of grains.

1.2.1.2 Capillary cohesion

Another important inter-particle interaction for powders is the capillary force between the grains. A humid environment is sufficient to significantly affect the flow of powders due to the effect of water at the contact points between particles [53, 54, 55, 56, 57]. Fig. 1.8 shows a capillary bridge between two particles of radius R and

density ρ_p. Due to the surface tension γ of the fluid, the interfacial energy of the fluid

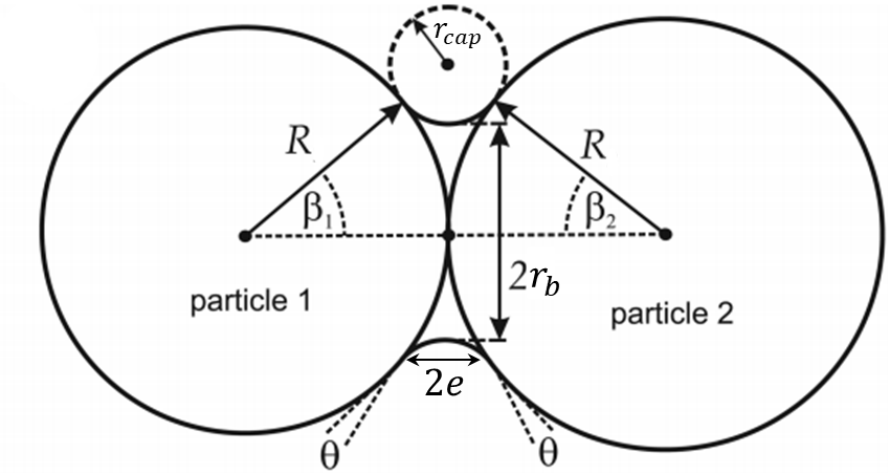

Figure 1.8 – A capillary bridge between two spherical grains, extracted from Gogelein *et al.* [58].

is: $E_i \sim \gamma\pi R^2$. This energy can be compared to the potential energy of the beads for a displacement of order R, thus giving the capillary radius r:

$$r_{cap} = \sqrt{\frac{3\gamma}{8\rho_p g}} \tag{1.15}$$

For water with surface tension $\gamma \sim 70$ mN.m^{-1}, and glass beads, the capillary radius is of order $r_{cap} \sim 1$ mm, which shows that the presence of water introduces a cohesive length scale that is non negligible compared to the size of the grains. However the force applied on the grains depends on the wetting properties characterised by the wetting angle θ.

The wetting angle θ is related to the surface tension γ through the Young-Dupré relation [59]:

$$\cos\theta = \frac{\gamma_{sg} - \gamma_{sl}}{\gamma} \tag{1.16}$$

where γ_{sg}, γ_{sl}, γ are the surface tension solid-gas, solid-liquid and liquid-gas, respectively. For a capillary bridge of thickness curvature radius r and width $2r_b$ and thickness e, and in the approximation $2e \ll R$ the capillary force applied by the bridge on the spheres is :

$$F_{cap} = 2\pi r_b \gamma \sin\theta + \pi {r_b}^2 \Delta P \tag{1.17}$$

The first term of this expression comes from the surface tension applied on a perimeter of radius r_b, and the second term comes from the pressure difference ΔP between the liquid bridge and the surrounding air. This pressure difference can be related to the

air-gas surface tension of the fluid through the Laplace equation :

$$\Delta P = \gamma \left(\frac{1}{r_{cap}} - \frac{1}{r_b} \right) \tag{1.18}$$

The limit of $2e \ll R$, implies that $r_{cap} \ll r_b$, therefore the contribution to the Laplace pressure mostly comes from r_{cap}. The term $2\pi r_b \gamma \sin\theta$ becomes negligible and the capillary force becomes $F_{cap} = \pi \gamma {r_b}^2 / r_{cap}$. Then, using the geometrical assumptions that $e \sim r_{cap} \cos\theta$ and ${r_b}^2 \sim 2eR$, the capillary force can be written as :

$$F_{cap} = 2\pi R \gamma \cos\theta \tag{1.19}$$

Surprisingly, the capillary force does not depend on the volume of the capillary bridge, which seems controversial with the sand castle experiment, where the water quantity seems to matter. Moreover, the capillary force between two beads is an order of magnitude than the adhesive force (equation 1.11) seen in section 1.2.1.1, which means that the adhesion due two the Van der Waals interactions should be strong enough to work as well as water bridges. This apparent paradox is solved by the fact that these results are only relevant for perfect spherical particles. Actual particles are always separated by the roughness at their surface, which is large enough to strongly decrease the Van der Waals interactions. As expected, for rough particles, the evolution of the capillary force depends on the volume of the liquid and on the roughness of the grains (Fig. 1.9). Halsey *et al.* [60] showed that for a very low water content, the roughness play the role of small particles, and introducing water increases the number of cohesive contact points, then the multiple bridges merge, and when the gap is filled the total force saturates at the value calculated from equation 1.19. In summary, the roughness shields the Van der Waals interactions, and a sufficient amount of water shields the roughness.

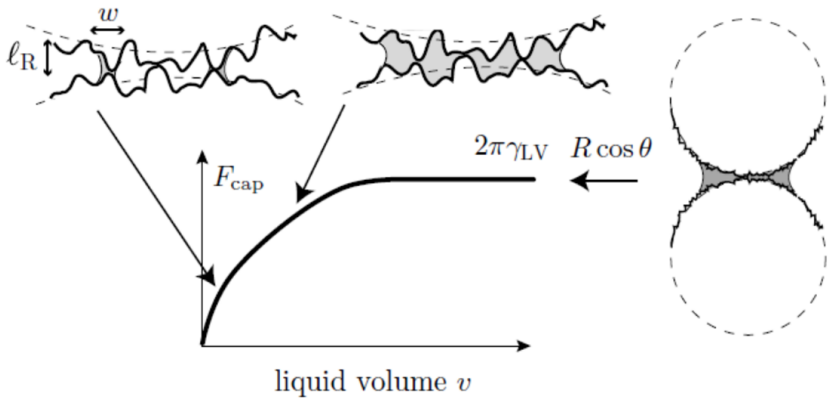

Figure 1.9 – Evolution of the capillary force between two rough surfaces, extracted from Andreotti *et al.* [6].

Therefore, the intuitive link between the cohesion and the volume of water added in

sand is recovered. However, anyone who has tried to make a sandcastle knows that too much water poured in sand tends to liquefy the granular bulk. Increasing the water quantity in a granular material changes its properties as seen in Fig. 1.10:

— Dry state : no water, the granular medium is not cohesive.
— Pendular : the liquid bridges are distributed at the granular contacts, the medium is cohesive.
— Funicular: the capillary bridges tend to merge, partially filling the void between the grains.
— Capillary : the medium is fully saturated , but is still cohesive due to the capillary pressure at the liquid/air interface.
— Suspension : the particles are fully immersed, the medium is not cohesive.

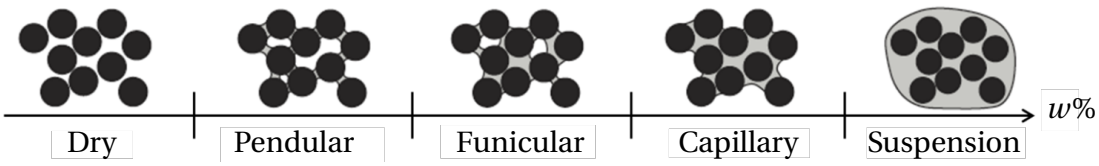

Figure 1.10 – States of wet granular materials as a function of the water content w.

For small enough particles, the effect of capillarity cannot be neglected and each powder may have its own interaction with moist environment [61, 62].

Another interaction is the electrostatic forces due to the triboelectric effect created when grains flow [55, 63]. This specific interaction is hard to model since it depends on several parameters, like the grains material, temperature and moisture, but is of first importance for industrial storage and manipulations. Indeed, without precautions to avoid these effects, powders may ignite or even explode. The aging of powders is also known to be a non-negligible parameter [64].

1.2.2 Interaction with air

A significant difference between powders and granular media is the volatility of powders, which tends to disperse in the surrounding air while flowing. Let us consider a spherical particle of diameter d and density ρ_p moving at the speed u_p in a fluid of dynamic viscosity η and density ρ_f. The particle Reynolds number is :

$$Re = \frac{\rho_f u_p d}{\eta} = \frac{u_p d}{\nu} \tag{1.20}$$

where ν is the kinematic viscosity of the fluid. In the limit of low Reynolds number $Re \ll 1$, the force applied on the particle by the fluid is governed by the viscosity. In this regime, the force applied to the particle is the Stokes force $F_{Stokes} = 3\pi\eta d u_p$, which can be balanced by the weight of the particle $F_p = (\pi/6)\rho_p d^3 g$ leading to the

limit diameter :

$$d_f = \left[18 \left(\frac{\rho_f}{\rho_p} \frac{\nu^2}{g} Re \right) \right]^{1/3} \simeq 40 \mu\text{m} \tag{1.21}$$

for a glass particle at a velocity $u_p \sim 1\ \text{m}.s^{-1}$ and $Re = 1$, which is the limit of the viscous regime. While this value of d_f is a correct order of magnitude, it is not comparable to what is observed experimentally. Indeed, we did not account for the collective effect of a bulk of particles, which may be seen as a porous media. Therefore, the correct fluid force applied on the particle comes from the Darcy law [65] and is written as $F_{Darcy} \sim (\eta/k) u_p d^3$, where k is the permeability of the porous media [66] and can be modelled through the Carman-Kozeny expression [67] as :

$$k = \frac{d^2}{180} \frac{(1-\phi)^3}{\phi^2} \tag{1.22}$$

where ϕ is the volume fraction of the material, usually close to 0.6 for granular media. Using this Darcy force, we estimate a new limit diameter :

$$d = \left[\frac{180\nu^2}{g} \frac{\phi^2}{(1-\phi)^3} \left(\frac{\rho_f}{\rho_p} \right) Re \right]^{1/3} \sim 160 \mu\text{m} \tag{1.23}$$

which is closer to what is observed experimentally. The limit of volatility is due to the size of the particle, even in a fluid at rest, therefore this effect constitutes one of the main issues during the handling of powders.

1.2.3 Empirical measurements on powders

Several studies have tried to measure the cohesion at the particle scale [55] or at the bulk scale [68, 69] and attempted to relate it to macroscopic properties like the angle of repose [70, 71], the packing fraction [1, 72] and the ability to flow [37, 73, 74, 75].

Some indicators of the behavior of powders were developed to account for the broad range of parameters necessary to describe powders [76]. First, at the micro-scale, powders are composed of grains of various shapes and densities. Two quantities are often measured to account for these parameters. The specific surface S_P corresponds to the ratio between the total surface of the grains and their mass. For a powder composed of particles of diameter R and density ρ, the specific surface writes $S_P = 3/\rho R$. The Sauter diameter $d_S = V_P/A_P$ is the ratio between the volume of a particle V_P and its surface A_P. This parameter represents the geometrical aspects of the particles composing the powder.

At a macro-scale, the behavior of powders may change depending on the method of preparation. Two consolitation parameters are often used to describe the ability of powders to compact. The first parameter is the Carr index $C = 100(V_b - V_t)/V_b$ where V_b is the aerated bulk volume and V_t is the tapped bulk volume of a powder. The second parameter is the Hausner ratio $H = \rho_t/\rho_a$, *i.e.* the ratio between the tapped density ρ_t and the aerated density ρ_a. The Haussner ratio is directly linked to the

Carr index : $H = 100/(100 - C)$. Often the consolidation parameters are presented as a function of the specific surface or the Sauter diameter to correlate the consolidation of powders with the geometry of the grains. Some examples of these parameters are given in appendix A.

Several studies have attempted to describe the flow properties of powders to describe the parameters governing the flow dynamics [77, 78, 79, 80]. The flowability is often a sought parameter [81, 82]. This parameter is supposed to describe the ability of a powder to flow and is essentially based on an intuitive appreciation of the behavior of a powder which is assumed to flow more easily if it can neither compact nor form aggregates. Therefore, most flowability measurements lean on consolidation tests or angle of repose measurements set for industrial equipment like the Hosokawa tester visible in Fig. 1.11(a).

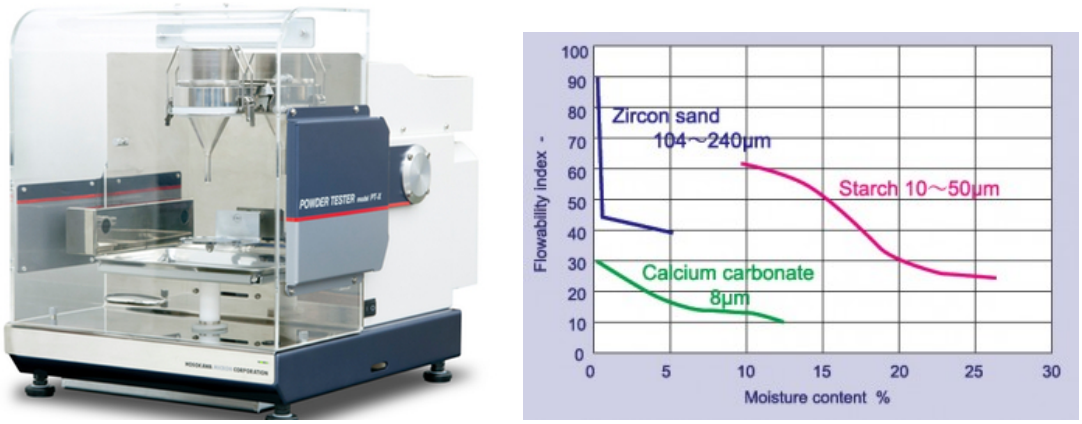

(a) (b)

Figure 1.11 – (a) The Hosokawa device. (b) Flowability measurements as a function of moisture content for three powders.

The Hosokawa tester provides a flowability index based on a succession of empirical experiments. The angle of repose of a powder is measured on a disc and on a spatula without tapping the powder. Then the same angles are measured with tapping after 180 vibrations. The last angle measured is the "fall angle". When the angle of repose is reached, it is possible to impose a hit on the disc. Then a certain amount of powder fall from the disc and the remaining amount form a "fall angle" with the disc. Each of these angles is associated to an index and the sum of these indexes gives a flowability index of the powder between 0 and 100. The higher the flowability index is, the easier it is supposed for the powder to flow. Examples of flowability measurements are given Fig. 1.11(b).

The main difficulties encountered when studying powders are that there are numerous types of powders with only a few generalizable results. A "model powder" is thus challenging to find, and every work on specific powders is hard to apply to a wide set of powders. These difficulties mainly comes from the difficulty to control

the adhesives forces between the grains since they mostly depends on the material used (Van der Waals and electrostatic forces), but also on the powder environment (capillary adhesion because of humidity).

Whereas various studies were carried out to understand the behavior of powders, the definition of powder flowability remains rudimentary. The major issues posed by the manipulation of powders, due to their great diversity, appeals the necessity to develop a model material with a controlled cohesion which could be used to simulate simplified powders behavior in order to get rid of some issues encountered while working on powders.

1.2.4 How to experimentally control cohesion ?

An approach to characterize the specific role of the inter-particle cohesive force, without the issues brought by air or electrostatic, would be to use larger grains and to control the cohesion. This section present the different methods found in the literature to add a cohesive force to granular materials.

1.2.4.1 Magnetic forces

A non intrusive method consists in applying a magnetic field on an assembly of ferromagnetic beads. For instance Peters *et al.* [83] used a vertical magnetic field $\vec{H}$ on iron beads to produce attraction between every grains. In this configuration, the cohesion force between a bead at the origin of the field, and a bead located at a position (r, θ) (see Fig. 1.12 (a)) writes :

$$\vec{F_{dip}} = \frac{d^6}{r^4} 12\pi\mu_0\mu_f \left(\frac{\mu_p - \mu_f}{\mu_p + 2\mu_f}\right)^2 H^2[(2cos^2\theta - sin^2\theta)\vec{e_r} + sin2\theta\vec{e_\theta}] \tag{1.24}$$

where d, μ_0, μ_f, and μ_p are the diameter of the grains, the vacuum permeability, the relative fluid permeability and the relative particle permeability, respectively, r is the distance between two beads, and H is the norm of the magnetic field.

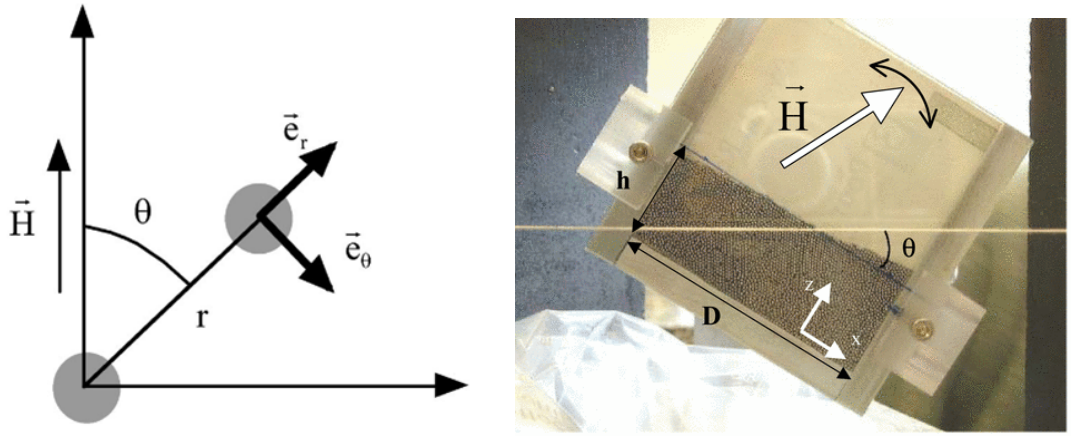

(a) (b)

Figure 1.12 – (a) Two iron beads interacting in a magnetic field. (b) Picture of the experiment used to quantify the flow of iron beads in a magnetic field $\vec{H}$, extracted from Peters *et al.* [83].

The strength of this approach is the non-intrusive way to create cohesion between grains, and its low sensitivity to the environment of the experiment. However, as seen in the expression on the cohesive force 1.24, the cohesion decreases rapidly from the origin of the magnetic field, therefore the cohesion is inhomogeneous in the granular medium, and changes when the particles start moving.Therefore the flowing properties of the grains are challenging to characterize in such a configuration. A strong disadvantage is also the cost of the equipment to create a strong enough magnetic field.

1.2.4.2 Solid bridges

Another method to introduce a cohesive force is to create solid bridges between the particles by using paraffin, epoxy or cross-linked PDMS bridges [84]. This configuration has mostly been studied to understand fracture in concrete-like materials [85] is illustrated in Fig. 1.13(a) or the failure of pseudo-2D granular systems [86]. The strength of this approach is the weak dependency on the environment, and, for pseudo-2D systems, the exact knowledge of coordination number Z and the packing fraction (see Fig. 1.13(b)).

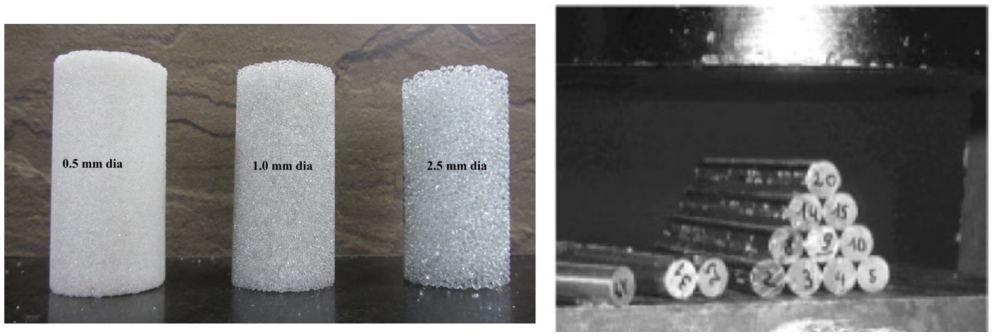

(a) (b)

Figure 1.13 – (a) Various set of beads glued together with epoxy, extracted from Singh *et al.* [85]. (b) Packed rod sticked with epoxy to study 2D granular materials, extracted from Delenne *et al.* [86].

While this approach is suitable to investigate the initial failure in cohesive granular materials, once the failure happens, the cohesion disappears. Another issue is the control of the cohesive force. Indeed, while it is possible to increase or decrease the number of solid bridges in the bulk by changing the compaction state, controlling the grain-to-grain cohesion seems tricky. Therefore, this type of cohesive material is not suitable to study of the flowing properties of cohesive powders where cohesive contacts can be recovered.

1.2.4.3 Wet granular materials

The most extensively studied cohesive granular material is probably wet grains. The low cost of the materials and the strong cohesive effect of capillary bridges has made it a perfect candidate to study cohesive granular materials. Additionally, several industrial processes require to mix water and grains, like plaster or concrete fabrication. Therefore, studying wet granular materials has not only a fundamental value, but also direct applications. As seen in section 1.2.1.2, a little amount of liquid is sufficient to create a strong cohesion due to capillary bridges between the grains. The properties of wet granular materials were studied in various configurations [87, 88, 89, 90, 91]. For instance, Tegzes *et al.* [92] used a rotating drum to measure the flow dynamics of wet grains (Fig. 1.14(a)). This setup consists of a rotating drum, filled with grains, rotating at a chosen velocity. Once the critical angle θ_c is reached, the granular material starts to flow until a new static state is reached. Then the avalanche rate and the depth of the flow provide indications on the flow properties of the granular material. This setup was used by Tegzes *et al.* [92] to show that avalanche rate and the shape of the free surface are correlated to the cohesion of the material. Xu *et al.* [93] also showed that the duration of the avalanches are linked to the viscous lubrication of the grains due to the capillary bridges. Moreover, this setup has been widely used to compare

experimental results with numerical simulations [94, 95, 96, 97].

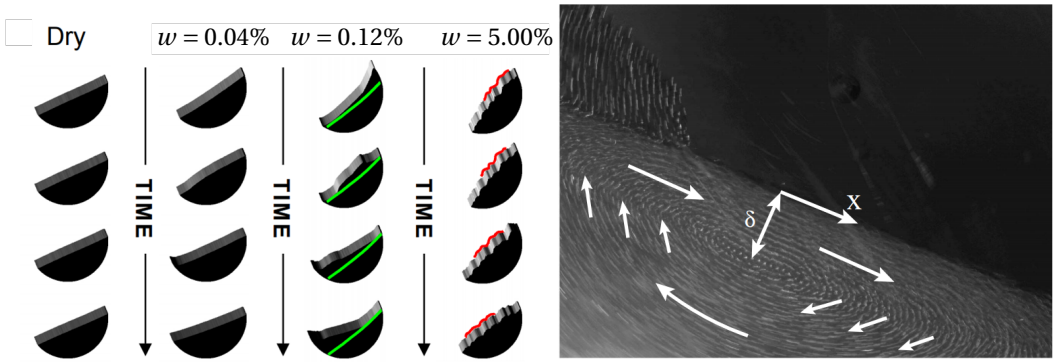

Figure 1.14 – (a) Angle of avalanche and surface roughness as a function of the amount of water in the granular material, extracted from [92]. (b) Layer of flow of a wet granular material in a rotating drum, extracted from [93].

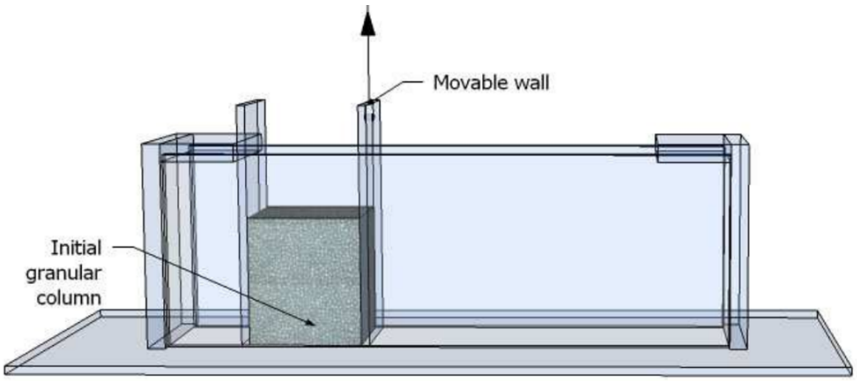

Figure 1.15 – Sketch of the experimental channel used for the granular column collapse experiment. Extracted from [98].

Another well-known configuration is the granular collapse, or dam break experiment. A rectangular pile of wet grains is prepared and held by a gate, as shown in Fig. 1.15. At the beginning of the experiment, the gate is lifted, the material spreads and stops at a given distance from its initial position (see Fig. 1.16). As we will present in section 5.1, this experiment is often used to characterize the frictional properties of dry granular materials [99, 100]. With wet granular materials, several authors focused on the effect of capillary cohesion on the stability conditions of a column [101, 102, 103, 104, 105], and on the spread of the material [98, 106, 107]. This setup, like the rotating drum experiment, has also been widely used as a benchmark for numerical simulations [**Fern2017**, 97, 108, 109].

While wet granular materials have been extensively studied, a specific care needs to be taken in order to conduct proper experiments. The bulk cohesion can be controlled

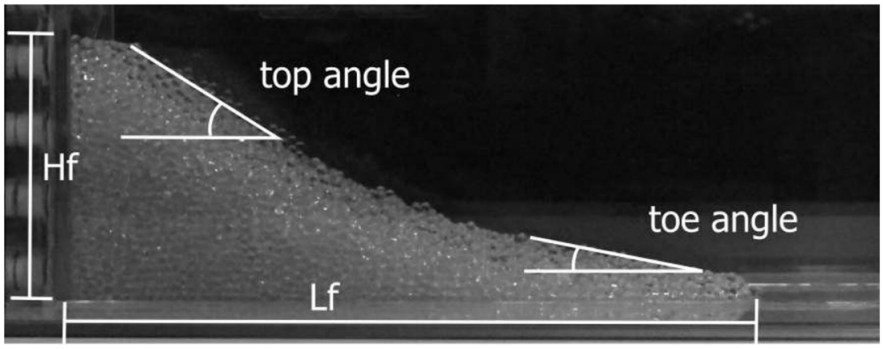

Figure 1.16 – Picture of a typical morphology of the deposit, after the collapse, with the parameters used to characterise the geometrical properties of the deposit. Extracted from [98].

through the quantity of water introduced in the media, and the cohesion is highly dependent of the environmental conditions (humidity, temperature, dirt, etc...), as well as the distribution of capillary bridges. Studying the cohesive flow in such a system is challenging because of the aging of contact bridges [110, 111] and by the migration and coalescence of the capillary bridges [112, 113]. Several works were carried out to describe the migration of water in granular materials [114, 115], for example Saingier *et al.* [113] studied experimentally the propagation of water into a dry granular material made of spherical beads, and Mani *et al.* [112] studied numerically the migration of water bridges in sheared unsaturated granular media. The wetting properties of the experimental apparatus also need to be known since they may affect the boundary conditions.

1.2.5 Continuum description and rheology of cohesive granular materials

1.2.5.1 Plasticity of cohesive granular media

As seen in section 1.1.2, the mechanical properties of a granular medium depends mainly on the frictional interactions between particles. This bulk friction effect can be estimated by measuring the pile angle of a granular material θ_c leading to the relation: $\mu_s = \tan\theta_c$. A classical approach to estimate θ_c is to consider the Mohr-Coulomb criterion of failure to determine the angle of stability of the granular material [6, 60]. In term of stress, the condition of stability of a granular material submitted to a normal stress σ and a tangential stress τ writes:

$$\tau < \mu_s \sigma \tag{1.25}$$

For a cohesive granular material, the equation 1.25 is modified as follows:

$$\tau < \mu_s \sigma + \tau_c \tag{1.26}$$

where τ_c is a threshold shear stress due to cohesion, sometimes written as $\tau_c = \mu_s \sigma_c$ where σ_c is a preload due to the cohesive forces between the grains. Considering an homogeneous distribution of the inter-particle forces, it is possible to estimate the value of σ_c as [6, 90, 116]:

$$\sigma_c = \frac{3\phi Z F}{2\pi d^2} \tag{1.27}$$

where F is the average inter-particle force, ϕ is the volume fraction and Z is the coordination number representing the average number of contact per grains. For instance, for wet granular materials, Fig. 1.17 shows that an increase of the amount of liquid also increases the number of cohesive contacts between the grains. Therefore,

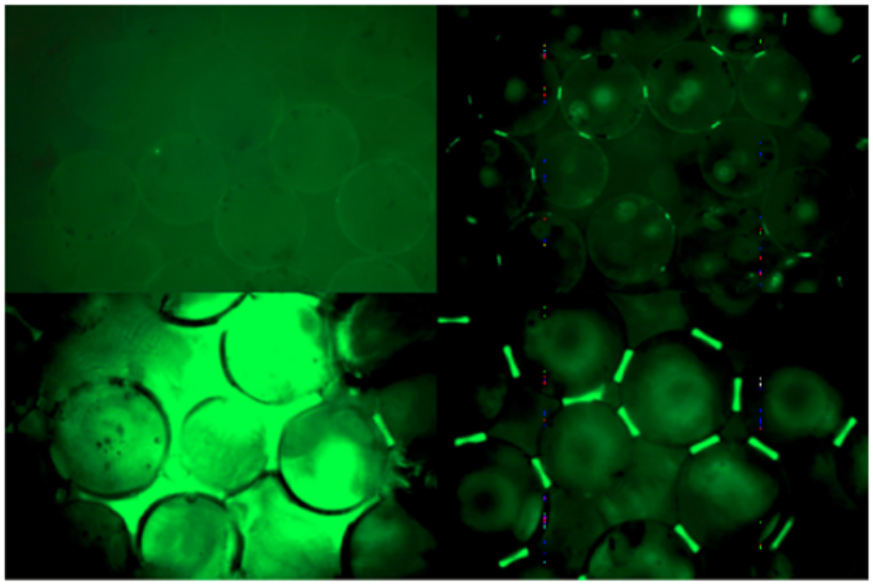

Figure 1.17 – Increasing quantity of liquid between glass beads, from top left and clockwise ($w = 0.1\%, 0.3\%, 3\%, 6\%$). The capillary bridges are made of water with fluorescein and oil and the visualisation is obtain by microscopic fluorescence, extracted from Moller *et al.* [117].

in the pendular state, increasing the volume of liquid corresponds to increasing the coordination number Z as well as the inter-particle force F, as illustrated in Fig. 1.18(a). Following equation 1.26, the cohesion $\tau_c = c = \mu_s \sigma_c$ represents the threshold tangential stress at rest ($\sigma = 0$). This cohesion can be measured experimentally, and is represented in Fig. 1.18(a), where the value of τ_c can be interpolated from the data for $\sigma = 0$.

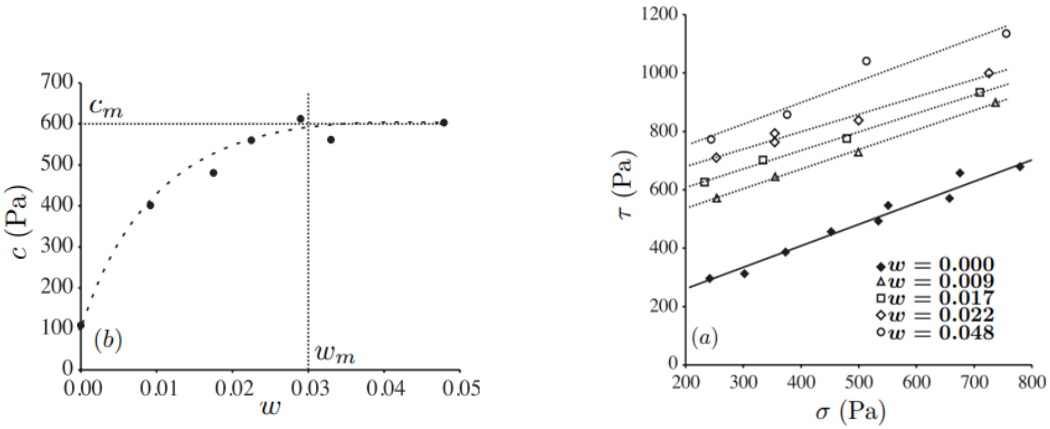

(a) (b)

Figure 1.18 – (a) Measurements of the cohesion c as a function of the water volume w and of (b) tangential stress τ as a function of the normal stress σ for several water ratio w in the granular media. The tangential stress at rest is τ_c and the slope is μ_s, extracted from Richefeu *et al.* [90].

The cohesive Mohr-Coulomb criterion of rupture has been widely studied for wet granular materials [53, 118, 119, 120, 121] mainly using pile angle, inclined planes and rotating drum experiments to characterise the effect of the cohesion on the critical angle θ_c. If we consider a layer of granular material of thickness h, volume fraction ϕ and density ρ_p inclined by an angle θ on a surface with a no-slip bottom condition, the failure criterion is reached when $\tau = \mu\sigma$. In this situation, the ratio between the normal stress $\sigma = \phi\rho_p g h\cos\theta$ and the tangential stress $\tau = \phi\rho_p g h\sin\theta$ gives :

$$\frac{\tau}{\sigma} = \tan\theta \tag{1.28}$$

Then the failure happens when θ reaches a critical value θ_c and the failure condition $\tan\theta_c = \mu_s$ is recovered. Following the same method that led to equation 1.28, we can write the critical angle θ_c for the cohesive Mohr-Coulomb criterion as:

$$\tan\theta_c = \mu_s\left(1 - \frac{\sigma_c}{\phi\rho_p g h\cos\theta_c}\right) \tag{1.29}$$

The static properties of cohesive granular medium is then quite well described, for wet granular media in the pendular regime, by a cohesive stress σ_c related linearly to the cohesive inter-particle interaction. For an applied stress beyond the plasticity threshold the cohesive material starts flowing and the rheology needs to be described to understand its behavior.

1.2.5.2 Constitutive law

Several studies have tried to extend the $\mu(I)$ rheology to cohesive granular media based on the understanding of the rheology of the flow of cohesionless grains, and the description of the cohesion based on the inter-particle force. First they focused on numerical simulations [122, 123, 124, 125] by implementing a short range attractive force between particles that rapidly decrease to zero when the grains are separated of an arbitrary distance s. More recently, Badetti *et al.* [125] used X-ray tomography and rheological experiments on wet granular media to investigate the rheology of cohesive granular media. They suggest to introduce a non-dimensional number P^* related to the cohesion.

$$P^* = \frac{Pd^2}{F}, \tag{1.30}$$

where P is the normal stress applied, F is the inter-particle adhesive force, and d is the grain diameter. Therefore, the rheological model needs to be slightly modified to account for this new parameter $\mu_{coh} = \mu(I, P^*)$ and $\phi_{coh} = \phi(I, P^*)$. They introduced the reduced cohesion c^* to generalise the Mohr-Coulomb criterion of failure :

$$c^* = \frac{cd^2}{F} = \frac{3\mu_s Z\phi(I, P^*)}{2\pi}. \tag{1.31}$$

Therefore the frictional rheology writes :

$$\mu_{coh} = \mu(I) + \frac{c^*(I, P^*)}{P^*} = \mu_s\left(1 + \frac{Z\phi(I, P^*)}{\pi P^*}\right). \tag{1.32}$$

This rheology has been tested by Badetti *et al.* [125] in a rheometric cell, and gives a good agreement between the experiments and the numerical simulations, as presented in Fig. 1.19.

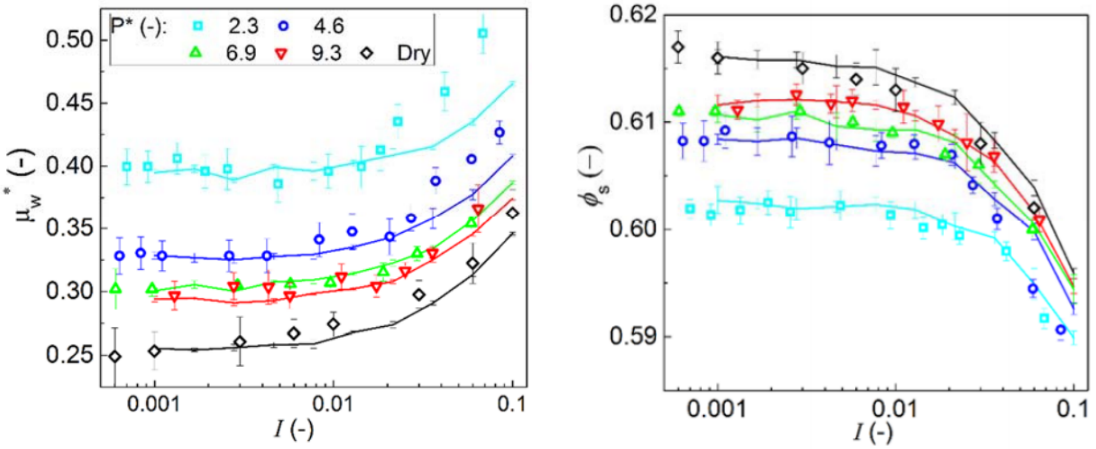

(a) (b)

Figure 1.19 – Evolution of (a) the internal friction coefficient μ and (b) the volume fraction ϕ (b) as a function of the inertial number I, for both experiments (round dots) and numerical results (data points joined by continuous line), extracted from Badetti *et al.*[126]

The rheology of the cohesive granular material based on the $\mu(I)$ constitutive law developed by Badetti *et al.* [126] seems to capture the statics and dynamics of wet granular media in the pendular regime. However, several questions have not been addressed. First, the interactions due to the migration of capillary bridges and the lubrication effects due to water are not accounted for and do not seem to have a significant impact on the rheology. Second, for the dry granular material, for low values of I (quasi-static regime), the friction coefficient μ_w tends to 0.25 which seems very low for polystyrene beads since most dry experiments tends to 0.4 [6, 10]. Also, the numerical simulation considers a particle-particle friction coefficient of 0.09 which also seems pretty low. Besides, other experimental measurements performed by Kuwano*et al.* [127] found an increase of the friction coefficient for low values of I (see Fig.1.20(a)). However the range of pressure used in these experiments are much larger than the ones used by Badetti *et al.* [126]. This trend suggests that other effects like instabilities or non-local effects are not well described by the standard $\mu(I)$ rheology.

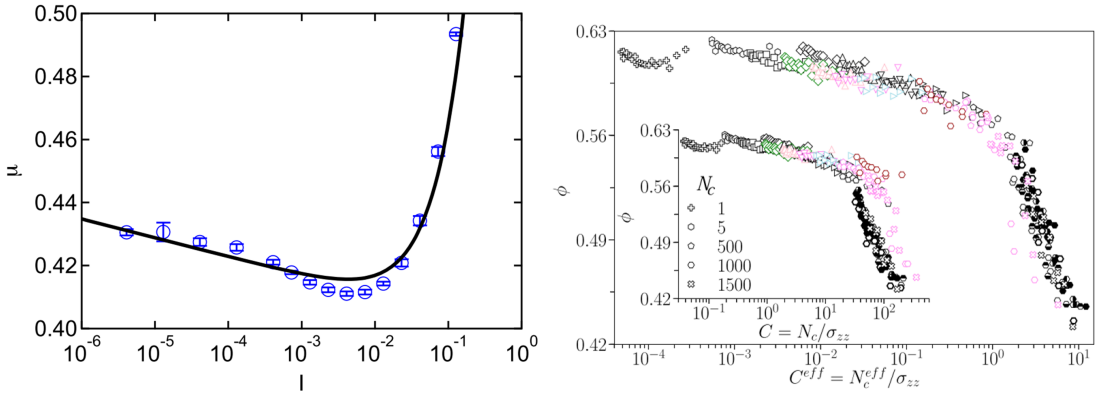

(a) (b)

Figure 1.20 – (a) Dependence of the steady state friction coefficient as a function of I, for an applied pressure of $P = 30$ kPa, extracted from Kuwano *et al.* [127]. (b) Variation of the volume fraction ϕ with the effective cohesion number C^{eff} in the case of a gravity-driven compaction. N_c correspond to the inter-particle force and σ_{zz} is the imposed pressure.

Other numerical simulations performed by Mandal *et al.* [128] using a plane shear geometry showed that other mechanical properties have a significant impact on the rheology of cohesive granular materials. They introduce an effective cohesion number $C^{eff} = \frac{F_c^{eff}}{Pd^2}$ to describe the volume fraction during the shear flow. In this expression, the effective adhesive force F_c^{eff} writes:

$$F_c^{eff} = F_c \left[\left(\frac{F_c}{k_n d} \right)^a \frac{1}{Q^b} \right] \tag{1.33}$$

where F_c is the inter-particle adhesive force, and k_n, d and Q are the stiffness, diameter and inelasticity of the particles, respectively. The value of a and b varies from 1/2 and 1/4, respectively, for a Hookean-JKR model, and to 1/3 and 3/4, respectively, for a Hertzian-DMT model. Mandal *et al.* showed that, for a given imposed pressure P, the volume fraction can be described by this effective cohesive number as depicted in Fig. 1.20(b). Their investigation on the rheology of cohesive granular media at low values of I showed a drastic increase of the effective friction coefficient and a decrease of the volume fraction (see Fig. 1.21). The deviation due to the transition to a shear-banded flow regime at low values of I is amplified by the cohesion and may be described by a non-local rheology [129].

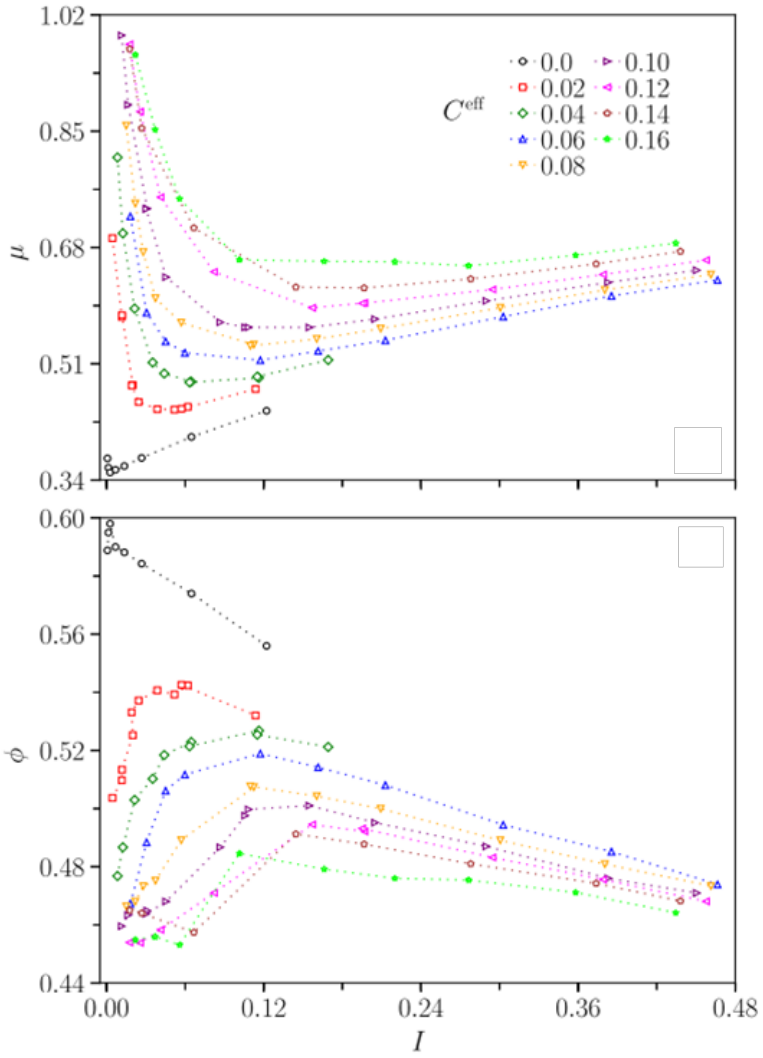

Figure 1.21 – $\mu(I)$ and $\phi(I)$ for different values of the cohesion C^{eff}. Data are obtained for different value of I in a plane shear geometry, extracted from Mandal *et al.* [129]

1.3 Objectives of the thesis

In this chapter, the state of the knowledge on the behavior of granular materials has been presented. The mechanical and dynamical properties of granular media mainly come from the frictional interactions, and a flowing granular material can be described as a fluid with rheological properties based on its internal friction. When cohesion is present, the dynamics becomes more complex. While some significant improvements have been made, most results come from numerical simulations and need to be validated through experimental investigations. Few methods allow to introduce a controlled cohesion in granular media. In particular, most experimental works have

been performed with wet granular materials, where the inter-particle cohesion is hardly controlled. Therefore, the characterization of the behavior of cohesive granular materials would strongly benefit from the elaboration of a simple cohesion-controlled granular material. In the following we will present the work performed to elaborate and test such a new controlled-cohesion granular material. First in chapter 2 we will present the methods of fabrication of the controlled-cohesion granular material (CCGM) developed at IUSTI and the experiments performed to measure the inter-particle and the bulk cohesions, the friction coefficient and the volume fraction. Results about the erosion of the cohesive materials by a turbulent jet of air will be presented in chapter 3. Chapter 4 will focus on the discharge of an axisymmetric silo and a rectangular quasi-2D silo filled with cohesive granular material. The study of the flow through the outlet of an axisymmetric silo will provide results on the threshold of flowability and an understanding of the flow behavior of cohesive granular materials. Then, Particle-image-velocimetry (PIV) performed at the outlet of the quasi 2D silo will bring new elements to understand the behavior of flowing cohesive granular materials. Chapter 5 will focus on the collapse of a cohesive granular column. First, the condition of stability of a cohesive column will be investigated, then the spreading dynamics of the grains and the final state of the collapsed materials will be analysed in details. This configuration will be compared to continuous numerical simulations performed by Anaïs Abramian at Institut Jean le Rond d'Alembert and will provide an investigation of the cohesive granular rheology. More specifically, this configuration will be used to focus on the frictional and cohesive behaviors of the granular material. Finally chapter 6 will provide a summary of the investigations performed on the effect of cohesion on the behavior of cohesive granular materials, and presents new perspectives and preliminary results on the rheology of the CCGM.

2 Characterization of a Cohesion-Controlled Granular Material (CCGM)

In this chapter we present a new method to prepare a cohesion-controlled granular material (CCGM) made from glass particles coated with polyborosiloxane (PBS), which suits many of the requirements to achieve experiments with a controlled cohesion. The main point is that the cohesion force between particles can be easily tuned through the PBS coating. The coating process of the particles is easy and does not require heavy chemical equipment. Furthermore, the CCGM is very stable on a long time scale, is insensitive to humidity of the ambient air, and is also insensitive to room temperature. The conception of this material was inspired by the kinetic sand toy, shown in Fig. 2.1, which is made of polymer coated sand. In order to control the cohesion, we decided to adapt this kinetic sand using spherical grains of controlled size, and to inject a chosen quantity of polymer inside the medium.

(a) (b)

Figure 2.1 – (a) The kinetic sand toy. (b) A sandcastle made with kinetic sand.

The preparation method is first presented in section 2.1. In section 2.2 the CCGM is tested in different classical configurations used for characterizing granular media : measurements of the bulk density, the pile angle and start angle measurements on an inclined plane experiment. Finally a detailed study of the inter-particle cohesive force

induced by the presence of the PBS coating is presented in section 2.3. Many results presented in this chapter have been already published in Phys. Rev. E [130].

2.1 Design of a cohesion controlled granular material

2.1.1 Preparation method

The coating material is a polyborosiloxane (PBS) made from a -OH terminated Polydimethylsiloxane (PDMS) cross-linked with boric acid (H_3BO_3) [131, 132]. Each batch of CCGM is prepared with a mass m_G of spherical glass beads (diameter d and density $\rho_G = 2600$ kg·m^{-3}) with a small polydispersity, a mass m_P of PDMS (density $\rho_P = 970$ kg·m^{-3}, viscosity 750 mPa·s and gyration radius $r_g = 17$ Å), and a mass m_A of boric acid. We kept a constant mass ratio of boric acid over PDMS $m_A/m_P = 0.14$. The boric acid is first dissolved in a small volume (50 ml) of purified water heated at 60 °C. The particles, the PDMS and the H_3BO_3 solution are then mixed together in a heating mixer (Kenwood Cooking Chef) at 110 °C during 90 minutes to ensure the evaporation of the water and a homogeneous PBS coating of the spherical particles. After 24 hours cooling, the batch is ready to use for experiments. The PBS has been characterized in a rheometer (MCR501 Anton Paar) using a plane-plane geometry. Fig. 2.2 shows measurements of the storage modulus G' and the loss modulus $G"$, evaluated at 35 kPa and 7.5 kPa respectively as a function of the pulsation of solicitation. The relaxation time constant has been evaluated at 3.8 s.

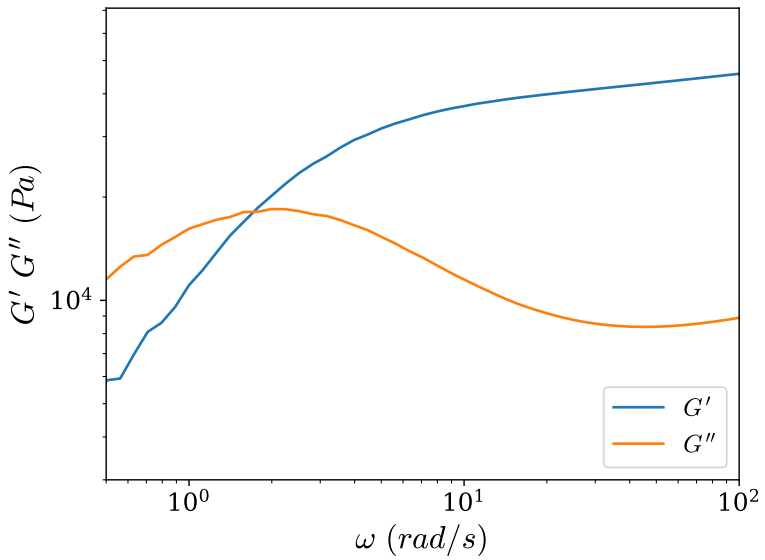

Figure 2.2 – Two measurements of the storage modulus G' and loss modulus $G"$ rescaled by the dynamic modulus G for the PBS.

The range of particle size used is $d = [0.2 - 1.4]$ mm in the macroscopic experiments of section. 2.2, and $d = [0.8 - 10]$ mm in experiments of section. 2.3 for the measurement of the inter-particle force. The effect of the PBS coating is qualitatively illustrated in Fig. 2.3 where a sample of 3 mm diameter coated glass beads reveals the cohesive nature of the material. The parameter controlling the cohesion in our study is the averaged thickness b. Assuming an homogeneous coating of a $\Omega_P = m_P/\rho_P$ volume of PBS over perfectly spherical particles of volume $\Omega_G = m_G/\rho_G$, the average thickness is

$$b = \frac{d}{2}\left[\left(1 + \frac{\Omega_P}{\Omega_G}\right)^{1/3} - 1\right]. \tag{2.1}$$

In the limit of a small coating averaged thickness ($b \ll d$), the PBS volume ratio Ω_P/Ω_G is approximately $6b/d$.

Figure 2.3 – Example of a cohesion-controlled granular material: a pile of glass beads $d = 3$ mm with a PBS coating layer of thickness $b = 2.2$ μm

.

2.1.2 Visualisation of the coating

An attempt to visualize the PBS layer using a confocal microscope is presented in Fig. 2.4. On the pictures, the PBS appears as a grey and foamy fluid, which is optically different from the clean glass surface. The pictures of the clean surfaces have been obtained after a careful removal of the PBS with a spray of heptane without touching or moving the particle. The iridescence seen in Fig. 2.4(b) indicates that the PBS layer is not perfectly uniform and may suffer from thickness variation, and that some "holes" in the coating layer may also exist Fig. 2.4(a). However, a statistical analysis of the inter-particle force discussed in section 2.3 shows that the presence of defects weakly

affects the cohesion between two particles. Since the coating layer is very thin, no capillary structure has been observed in optical microscopy when putting two beads in contact.

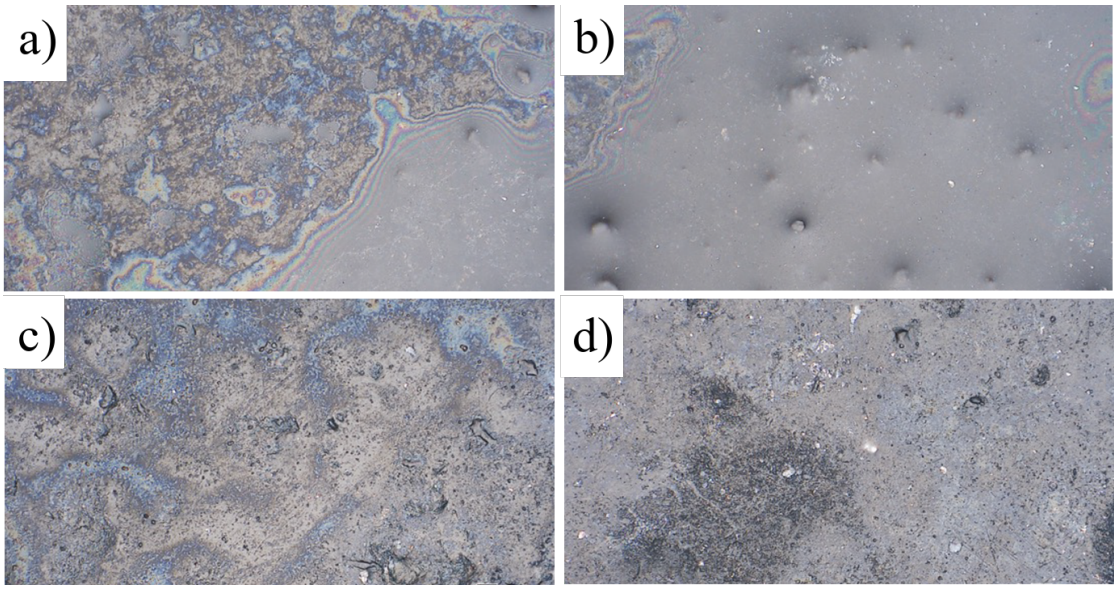

Figure 2.4 – Close-up visualization of the PBS coating on two different sample glass beads (d = 10 mm) with an optical microscope (magnification ×700). (a) A well coated area of particle 1 and (c) the same area after cleaning with a spray of heptane. (b) An irregularly coated area of particle 2 and (d) the same clean area. Iridescence can be seen where the PBS layer is not homogeneous.

We tried to observe the coating behavior for very large values of b ($b = 2$ µm) when separating two spherical beads. Fig. 2.5(a)-(b) show that little menisci appear when beads are slightly separated. Fig. 2.6(a) shows a closer look to one meniscus. We also performed some atomic force microscope (AFM) measurements of the coated surface of 800 µm beads thanks to Alain Ranguis at the Centre Interdisciplinaire de Nanoscience de Marseille (CINaM). Fig. 2.6(b) shows the surface of a coated bead of approximately 500 nm coating thickness. Some hexagonal shapes can me seen on several photograph of the surface, so we suspect these shapes to be some boric acid crystals that have not been diluted in the PDMS. Assuming this, it could imply that the quantity of boric acid used could be less.

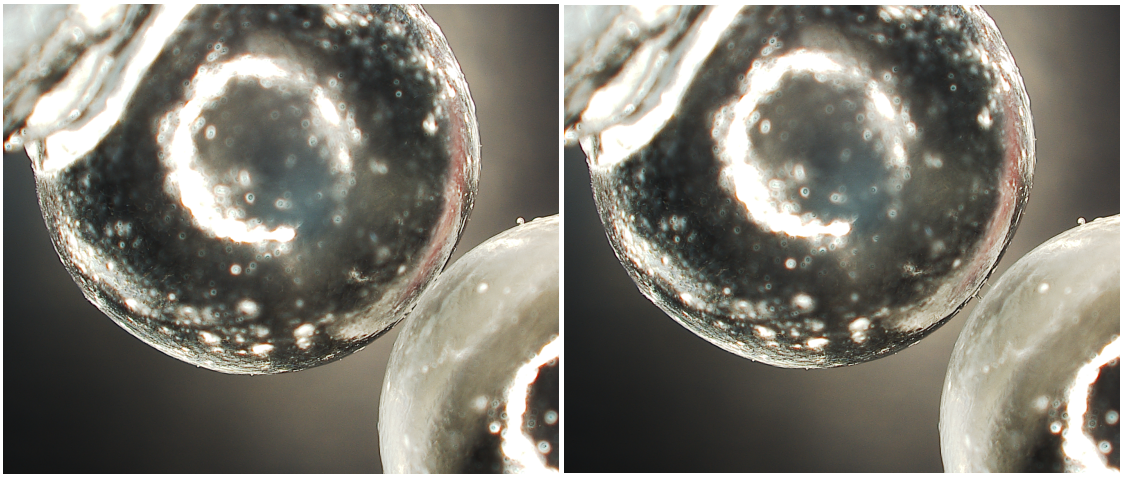

(a) (b)

Figure 2.5 – (a) Two spherical beads of diameter $d = 5\ mm$ and coating thickness $b = 2\ \mu m$ in contact and (b) slightly separated.

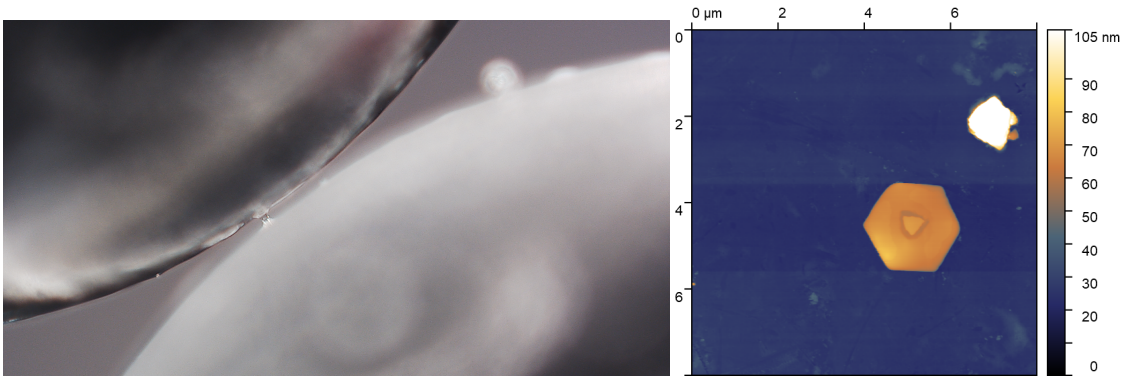

(a) (b)

Figure 2.6 – (a) Meniscus formed by pulling out two beads in contact. (b) AFM measurements of the coated surface an 800 µm. The coating thickness b is approximately 500 nm.

An important remark is that the strong Si-OH link between the polymer and the glass bead surface helps the PBS to stick permanently on the particles. No drainage of the fluid was observed even over a very long time (on the timescale of a year), leading to very stable material in time, as will be discussed in section section 2.2. Since the PBS is "glass-friendly", glass surface are avoided in experimental setups to prevent the particles from sticking to walls.

2.2 Bulk behavior of the CCGM

In this section we discuss the collective behavior of the coated particles in several classical configurations used in the literature for characterizing granular media. The goal is to show that the ability to accurately control the inter-particle cohesion force between the grains opens new perspectives to understand the behavior of cohesive granular media. This section presents experimental results for the angle of repose of static piles, for the bulk density, and for the onset of the flow of a layer of CCGM resting on an inclined plane.

2.2.1 Angle of repose

The measure of the slope angle of a granular heap is a simple way to emphasize the role of the cohesion powders or and granular materials [56, 71, 133, 118, 120, 134]. With our CCGM, static piles were made from a chute flow from a hopper on a 5 cm diameter rough disc. A side-view camera captured the image of a pile and the angle of repose θ_r is obtained from image analysis. Examples of images of piles are given in Fig. 2.7. Measurements are averaged over 20 iterations. The repose angle is observed to increase when increasing the PBS thickness. Without coating (Fig. 2.7(a)), the heap presents a smooth surface with a constant angle. Adding some cohesion gives rise to steeper slopes, and also to abrupt local variations of the local angle as illustrated in Fig. 2.7(b-d).

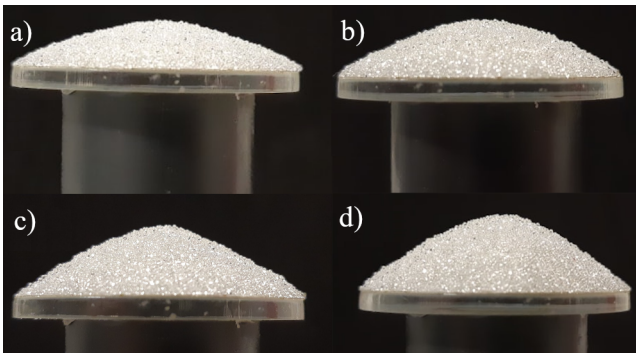

Figure 2.7 – Images of piles for a CCGM with $d = 480$ μm with increasing PBS coating: (a) no coating, $\theta_r = 27.7 \pm 0.8$, (b) $b = 31$ nm, $\theta_r = 30.1 \pm 0.9$, (c) $b = 52$ nm, $\theta_r = 40.3 \pm 1.9$, (d) $b = 62$ nm, $\theta_r = 42.5 \pm 2.2$

Fig. 2.8 shows that the angle θ_r increases with the coating thickness b, with a sharp increase for $b \approx 40$ nm and seems to saturate for coatings larger than 50 nm. We compare our results with the repose angle obtained with the crater method using vacuum pump oil coated particles [118, 120] in Fig. 2.8. For the crater method, grains are poured in a rectangular tank with an outlet at the bottom of the tank. After the fall of the grains through the outlet, the angle of repose is given by the slope made by the

remaining granular material between the borders of the outlet and the walls of the tank. While the heap formation methods are different, the CCGM presents a similar trend. It is important to note that we did note manage to obtain angle of repose for coatings larger than 80-100 nm for the grain sizes considered since at large coating thickness the shape of the material is very rough and therefore cannot be associated to a pile.

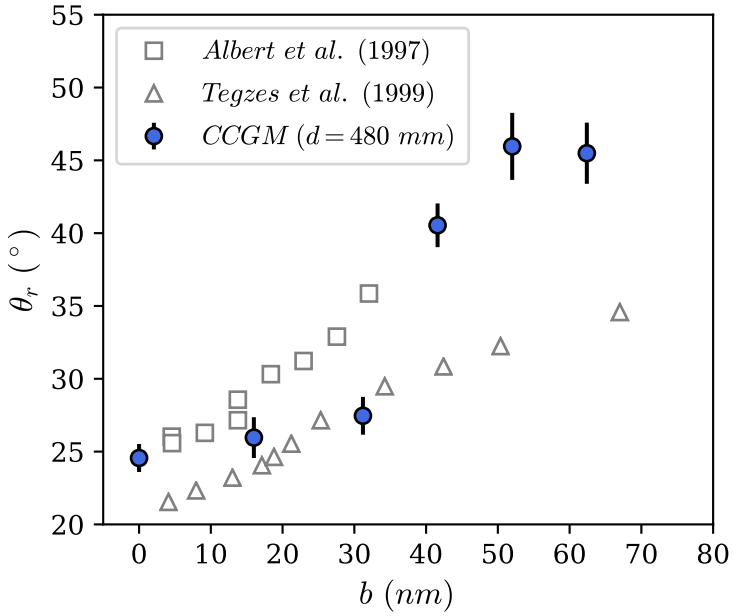

Figure 2.8 – Heap repose angle for $d = 480$ μm particles and various coatings. Empty symbols are data from the literature with capillary cohesion: $d = 800$ μm Albert *et al.* [118] (squares) and $d = 900$ μm Tegzes *et al.* [120] (triangles).

The heap angle experiment is also a benchmark test to assess the stability and the durability of the CCGM. The first test concerns the stability with temperature since the cohesion is based on a cross-linked polymer. Piles have been prepared with a CCGM stored in controlled-temperature devices. As shown in Fig. 2.9(a), the repose angle is nearly independent of temperature from 0°C to 60°C. No noticeable difference was found between experiments at 20°C and 60°C. This means that no specific care is needed for experiments at a standard room temperature.

We also investigated the role of ambient humidity on the pile angle. The repose angle θ_r is plotted in Fig. 2.9(b) as a function of the ambient humidity. For our experiments, no specific trend is observed and it is therefore quite safe to assume that cohesion is not affected by ambient humidity as the pile angle is not affected by it.

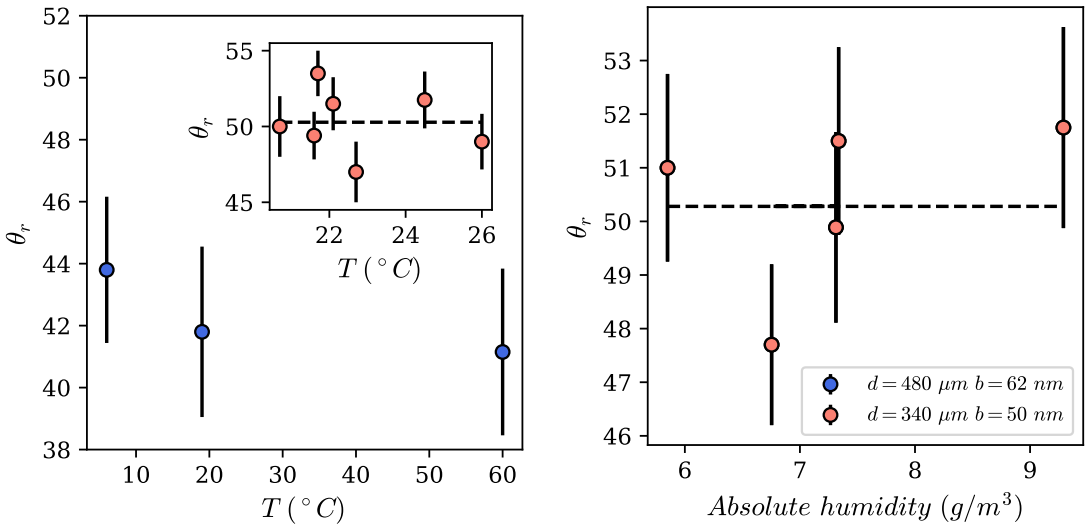

(a) (b)

Figure 2.9 – (a) Effect of the temperature on the repose angle of a CCGM ($d = 480\ \mu$m, $b = 62$ nm), Inset:($d = 340\ \mu$m, $b = 50$ nm). (b) Effect of humidity on the repose angle of a CCGM ($d = 340\ \mu$m, $b = 50$ nm)

We have also investigated the stability of the CCGM with time by measuring the heap repose angle for the same batch of particles at different ages. Fig. 2.10 shows the evolution of the repose angle θ_r for three different materials at different ages from preparation. This plot shows that for thin coatings ($b = 16$ or $b = 31$ nm), the heap angle remains identical even for sample prepared one year ago. Our experiments on aging of the cohesive effect were performed without humidity control across different temperature and humidity conditions over a year and no variation of the pile angle were observed within 6 months at least. For a thicker coating ($b = 62$ nm), a slow decrease of the repose angle has been observed. Nevertheless, the PBS-coated CCGM seems to be stable for months and large batches can then be prepared before performing large-scale experiments.

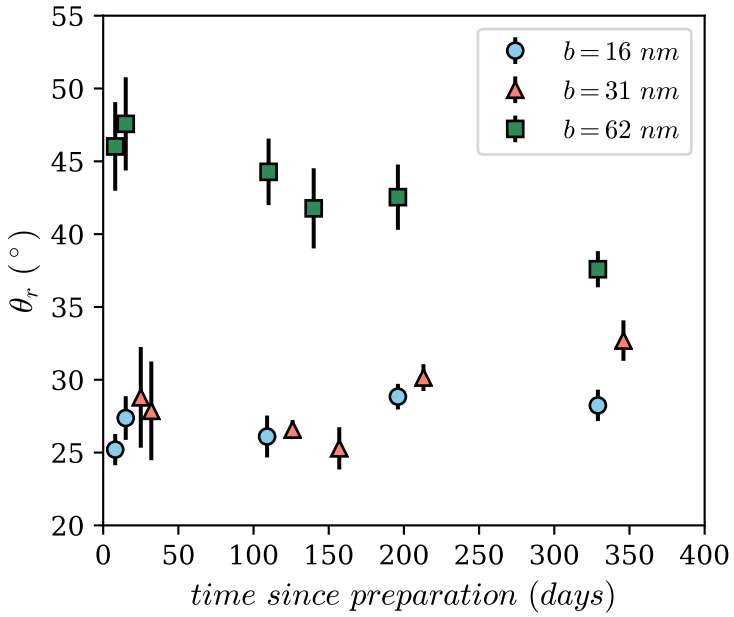

Figure 2.10 – Heap repose angle θ_r as a function of the time since the preparation of the CCGM. Experiments were made with $d = 480\ \mu$m particles.

While this measurement is relevant to qualitatively characterize the effect of cohesion on granular materials, as well as the effect of temperature or moisture on cohesion, it is limited to thin coating, thus small cohesion, due to the difficulty to define a pile angle for highly cohesive granular materials. However, other qualitative measurements allows to characterize strong cohesive effects, following some precautions.

2.2.2 Packing fraction

In many industrial processes, the bulk density of a granular assembly is a qualitative indicator of the cohesive property of the medium [74, 135]. The Haussner ratio or the Carr index are often used both implying the measurement of the bulk density in two different compaction states: the aerated density ρ_B (similar to the random loose packing state) and the tapped density ρ_T (similar to the random close packing). In the following, we investigate how the loose packing fraction changes for CCGM batches when varying the PBS coating. The random loose packing fraction ϕ_{rlp} was evaluated through mass and volume measurements in a 250 cm^3 and a 1000 cm^3 graduated cylindrical test tube where the granular material is poured in a narrow funnel above the tube. The test tube is made of plastic and not glass to avoid cohesive interactions of the particles with the walls.

(a) (b)

Figure 2.11 – (a) Highly cohesive granular material poured in a tube with intense stirring in the funnel above versus (b) no stirring in the funnel, $d = 340\mu m$ and $b = 440nm$.

Fig. 2.11(a) shows the main issue encountered when measuring the volume fraction for highly cohesive materials. The material is hardly flowing through the funnel and the strong cohesion creates aggregates, fractures and large voids, and therefore the average volume fraction is not relevant. To ensure an homogeneous material, the cohesive grains are strongly stirred in the funnel to break aggregates and measure the packing fraction of an homogeneous deposit. A picture of the stirred material is shown Fig. 2.11(b). The packing fraction is then obtained as follows:

$$\phi_{rlp} = \frac{m}{V_m \rho_g} \tag{2.2}$$

where m is the mass poured in the test tube, V_m is the volume measured and ρ_g is the

density of the grains material, $\rho_g \approx 2500$ for glass beads). The results are presented in Fig. 2.12 for coating layer thickness varying from 72 to 624 nm. The best collapse of experimental data is obtained with a plot of the packing fraction versus the ratio b/d which is proportional to the volume ratio Ω_P/Ω_G.

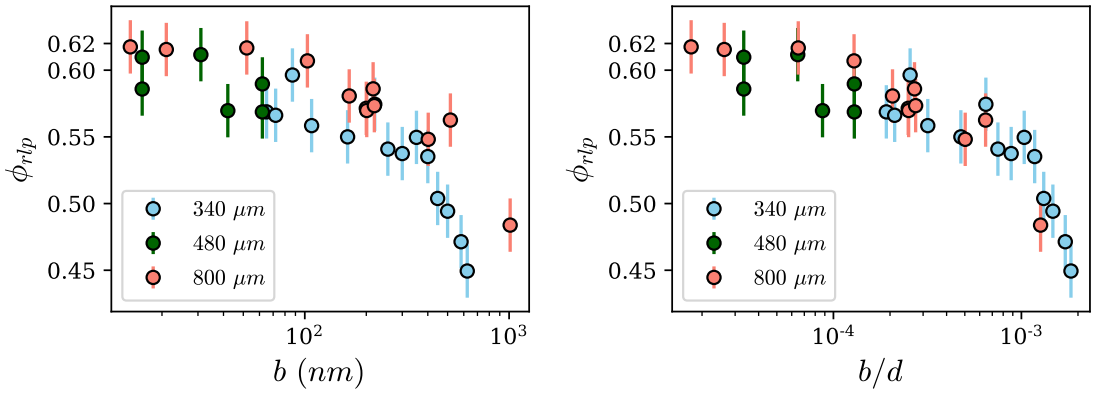

(a) (b)

Figure 2.12 – Random loose packing fraction of various CCGM with different particle sizes as a function of (a) the coating thickness b and (b) the ratio b/d.

For very low values of the coating ($b/d < 10^{-4}$), the packing fraction is equal to the packing fraction of clean and dry glass beads. The packing fraction decreases for an increasing PBS content, and a very low packing fraction $\phi_{rlp} \approx 0.45$ may be reached for a typical $b/d \approx 10^{-3}$ value. This can be explained by the existence of large-scale voids and arches in the bulk sustained by strong cohesive links between particles. Some sample were also tested in an Hosokawa powder tester at SGR Provence. Fig. 2.13 show the evolution of the Haussner ratio with the coating thickness, the trend observed is similar to the evolution of the packing fraction.

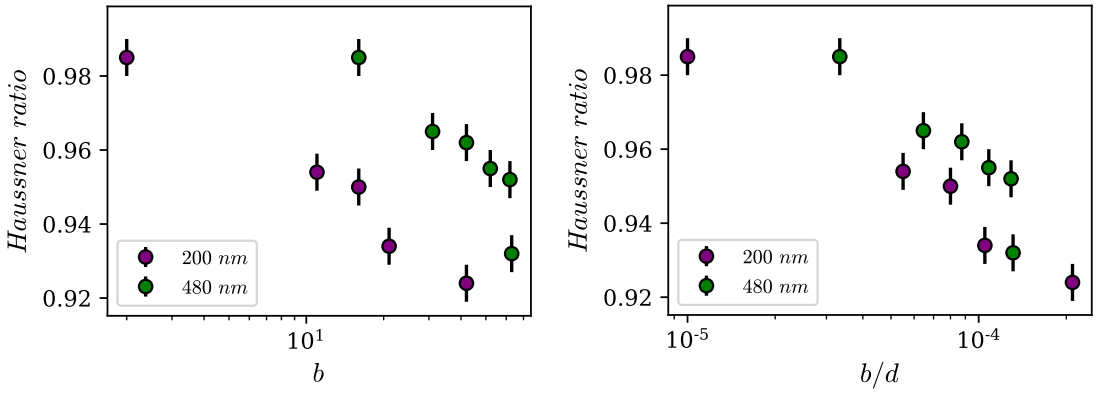

(a) (b)

Figure 2.13 – Haussner ratio of various CCGM with different particle sizes as a function of (a) the coating thickness b and (b) the ratio b/d.

2.2.3 Onset of flow on an inclined plane

Measuring the onset of flow of a layer of particles lying on a rough inclined bed is another way to investigate the friction and the cohesion of a material. The simplest description of the plasticity of a granular material assumes that the yield stress follows a cohesive Mohr-Coulomb criterion, presented in section 1.2.5.1, $\tau_{yield} = \mu P + \tau_c$, where μ is the friction coefficient, P the confining pressure and τ_c the cohesive stress. Starting from an horizontal plane and increasing progressively the inclination θ, a layer of thickness h will start to flow at a critical angle θ_{start} when the shear stress at the base reaches the yield stress value:

$$\rho_G \phi g h \sin\theta_{start} = \mu \rho_G \phi g h \cos\theta_{start} + \tau_c \tag{2.3}$$

where ϕ is the volume fraction of the layer. This equation can be simplified as

$$h \sin\theta_{start} = \mu h \cos\theta_{start} + \ell_c \tag{2.4}$$

where ℓ_c is a characteristic cohesive length, which represents the maximum thickness of a self-standing vertical layer of granular medium stuck to a rough surface under gravity :

$$\ell_c = \frac{\tau_c}{\phi \rho g} \tag{2.5}$$

Equation 2.4 shows that the cohesion length ℓ_c and the friction coefficient μ can be identified by systematically measuring the critical starting angle θ_{start} for different thicknesses h. We have conducted such a series of experiments with our model cohesive material. For seek of efficiency, we have not used a uniform layer as initial state, but rather a prismatic deposit, as sketched in Fig. 2.14(a). With this geometry, it

is possible with a single experiment to perform several measurements of (h, θ_{start}).

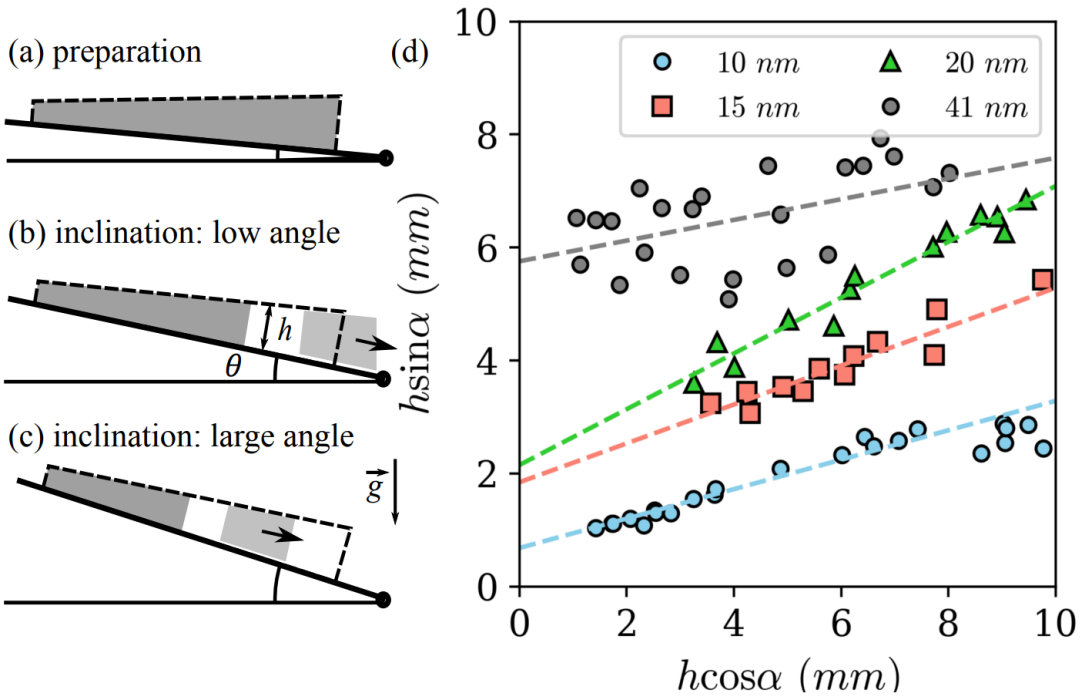

Figure 2.14 – (a)-(c): Sketch of the inclined plane setup with the variable granular thickness and a progressive inclination. (d): Inclined plane results for $d = 202$ μm CCGM particles with increasing coating thickness. Dashed lines are best fits using Eq. (2.4).

A typical experiment is conducted as follows. The CCGM is poured on a 20×10 cm^2 rectangular rough plate (the roughness is made with CCGM particles glued on a double sided adhesive tape) with two prismatic side walls. The free surface of the deposit is then leveled following the two side walls. The final prismatic volume has a thickness varying linearly from 15 to 25 mm (see Fig. 2.14(a)). The thickness of the granular layer is measured with a laser sheet technique and the angle with a clinometer. Starting from a very low angle of inclination (typically 10°), the setup is slowly inclined at a constant rate. A first avalanche occurs at the bottom thick side (Fig. 2.14(b)), leaving a thinner and shorter prism. When the angle is further increased, a second avalanche occurs (Fig. 2.14(c)), which corresponds to a different h, and so on. In one experiment, one can then extract the critical angle θ_{start} for 4 to 5 different thicknesses. For a single CCGM batch, this experiment is repeated several times. The collected data are then plotted in a $(h\cos\theta_{start}, h\sin\theta_{start})$ plane. According to equation 2.4, a linear fit of experimental data gives the slope μ and the intercept value ℓ_c for a given CCGM. Fig. 2.14(d) shows the $(h\cos\theta_{start}, h\sin\theta_{start})$ plot for small glass beads of diameter $d = 202 \pm 4$ μm. Results are given for 4 coatings of increasing thickness b. Despite some experimental noise, the linear expression 2.3 fits well the experimental data.

Increasing the coating thickness b increases the cohesive length ℓ_c (the intercept of the linear fit with the vertical axis), but does not significantly affect the friction coefficient (the slope of the lines). From the measure of ℓ_c, one can then estimate the cohesive stress τ_c. As we have seen in the previous section, the value of ϕ depends on the cohesion. While using $\phi \approx 0.6$ is quite straightforward and give a reasonable approximation, mostly for low cohesion, a more accurate method is to measure the weight of grains put on the inclined plane. Then, knowing its dimensions, the value of ϕ can be estimated using equation 2.2.

In this section we presented the process of fabrication of a cohesive granular material that is not affected by temperature, humidity and that keeps its cohesive properties for a long period of time. The macroscopic cohesion can be estimated using a simple inclined plane experiment and we managed to characterize the effect of cohesion on the bulk packing fraction. In the following, we will investigate the inter-particle cohesion force.

2.3 Inter-particle cohesion force measurements

The previous section was dedicated to the effect of cohesion on a macroscopic granular bulk. In this section we present the results of different experiments designed to measure the contact force between two particles due to the PBS coating. As presented in the previous sections, the control parameters are the size of the beads (diameter d) and the PBS averaged layer thickness b. We designed two methods to accurately measure the cohesion force.

2.3.1 Role of the pre-compression load

The cohesion force between two CCGM particles has been first measured using the rotating head of a Anton-Parr MCR501 rheometer. A sketch of the experimental set-up is given in Fig. 2.18(a). A coated particle is attached to a fixed rigid structure through a linear spring and a similar coated particle from the same batch is glued at the end of an arm attached to the rheometer head. The spring has two functions : first it adds a softness to the device, thus avoiding vibrations, and second, it ensures the alignment of the beads. The two particles are put in contact and a pre-compression torque T_{pc} corresponding to a pre-compression force F_{pc} is applied before slowly reversing the applied torque up to the point when the two particles suddenly detach. The critical torque when detachment occurs provides the measurement of the cohesion force F_c. The measurements are done on large beads (typically $d > 5$ mm) as smaller beads are more difficult to align. This method provides accurate measurements and is used to study the history of the system but performing a statistical analysis is tedious.

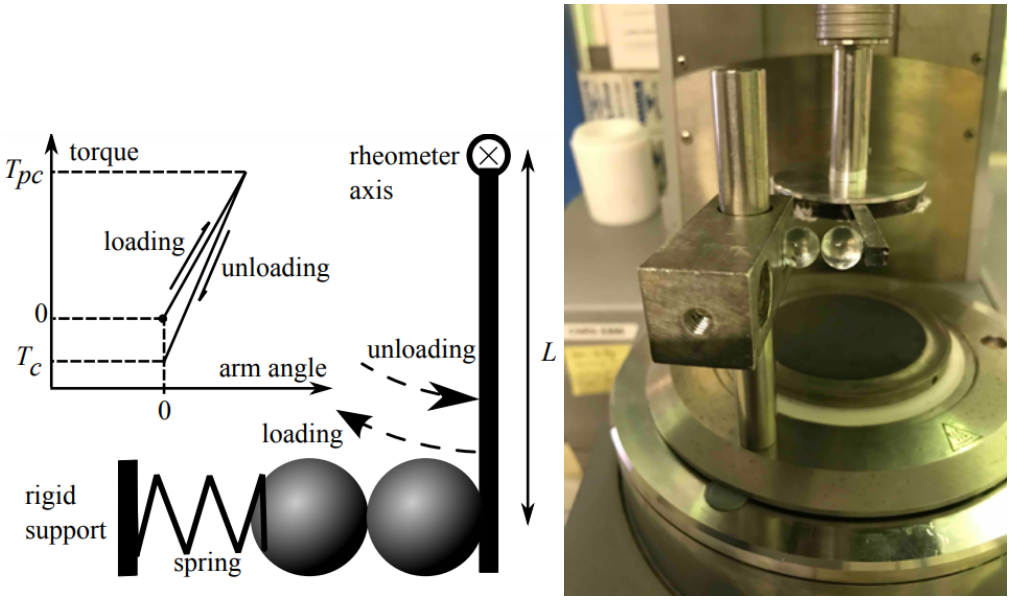

(a) (b)

Figure 2.15 – (a) Sketch and (b) picture of the setup to measure the cohesion force for different pre-compression force using the rheometer torque-meter. The two particles are put in contact with a pre-compression force $F_{pc} = T_{pc}/L$, where $L = 3.5$ cm is the arm length and the cohesion force $F_c = T_c/L$ is measured when the two particles detaches. The spring is not present on the picture.

A measurement of the inter-particle cohesion force is given in Fig. 2.16(a)-(b). The applied load is 1.57 N and the measured pulling force is close to 2 mN (see Fig. 2.16(b)). Note that for the same compression load, the pulling force rate do not change the measured cohesion force.

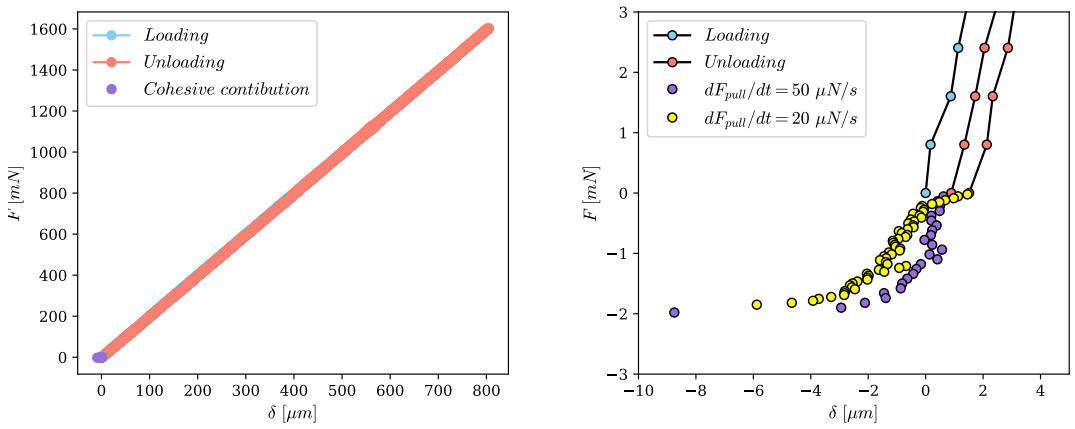

(a) (b)

Figure 2.16 – (a) Loading and unloading force applied by the rheometer on the system beads + string ($d = 10\ mm$, $b = 5\ \mu m$ and (b) zoom at the cohesion contribution when pulling out for two pulling force rates, δ is the displacement.

We measure the cohesion force using $d = 10$ mm particles and with a coating $b = 5$ μm, and the pre-compression force F_{pc} is varied from 0.08 N to 2 N. Fig. 2.17(a) shows that the cohesion force F_c does not depend on the pre-compression force F_{pc}, and that the order of magnitude of the cohesion force is $F_c \approx 5$ mN (dashed line). This independence of the cohesion with the compression force has been also observed in a different system by Kobayashi *et al.* [136]. With this setup, we also study if the cohesion force is affected by the number of successive contacts. One can wonder if the polymer layer can be altered after the first sticking contact. Fig. 2.17(b) shows for three different pre-compression forces that the cohesion force is independent of the number of successive contacts. We therefore conclude that the PBS layer is strongly attached to the glass bead surface and that the stick-pull process occurring for a binary contact is reversible. A last important remark is that variation in the mean cohesion force is observed in Fig. 2.17(b): the mean cohesion is $F_c = 4.3$ mN for the triangle symbols and $F_c = 3.7$ mN mean force for the star symbols. This is an indication that the cohesion force may vary from one pair of particle to another and that a statistical analysis is necessary. This has motivated us to develop a second experimental setup to measure in parallel the cohesion force for 10 pairs of particles.

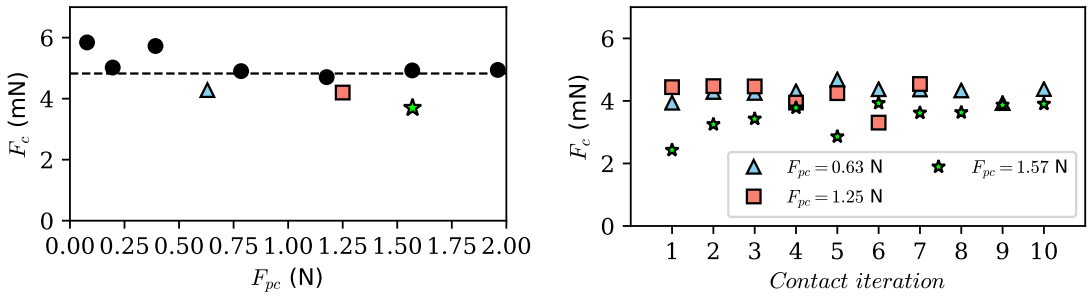

(a) (b)

Figure 2.17 – (a) Cohesion force measured for different pre-compression forces d = 10 mm, $b = 5$ μm. The dashed line indicates the mean cohesion force. Empty coloured symbols refer to the legend of (b). (b) Cohesion force for successive contacts, and for different pre-compression forces. The contact waiting time was kept constant equal to 10 minutes. If not visible, the error bars are smaller than the symbol size.

2.3.2 Role of the contact waiting time

The second method is a home-designed force measurement device sketched in Fig. 2.18, and consists in a set of 10 independent parallel pendulums. Each pendulum has one particle (B) attached at the bottom of the arm (Fig. 2.18(b)), which come into contact with a fixed particle (A). A third particle (C) is also glued on the other side of the pendulum arm and play the role of a counter-weight. The setup is mounted on a table that can be inclined. Starting from a nearly horizontal position (step 1 in Fig. 2.18(a), the table is slowly inclined with a rate $10°\cdot\text{min}^{-1}$ (step 2) until all the pairs of particles detach (step 3). The whole measurement process is recorded with a camera, and each time a pair of particles is detaching, the angle α_c is recorded and the cohesion force F_c is computed from the torque balance.

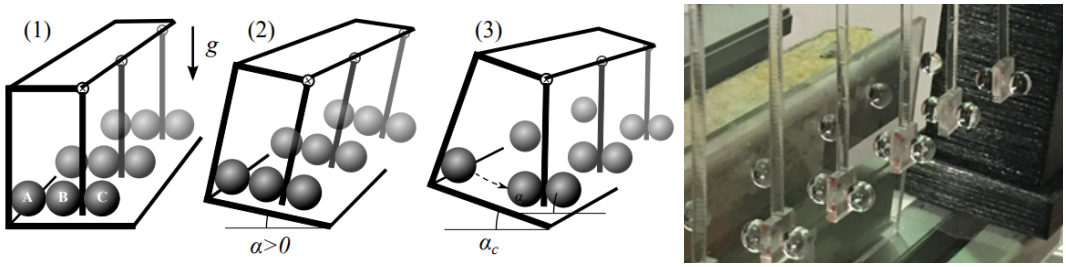

(a) (b)

Figure 2.18 – (a) Sketch and (b) picture of the pendulum experimental setup. Particle A is attached to a rigid structure, particle B and C are attached to the two sides of a pendulum. F_c is measured by inclining the setup. 10 pendulums were mounted in parallel.

With this second device, the influence of the contact waiting time between two coated particles has been investigated from 5 seconds to 2 hours. We also investigated a 24 hours waiting time but the results were not significantly different from the 2 hours results. Fig. 2.19 shows that the cohesion force varies with contact time t_c for $t_c \leqslant 600$ s) but eventually saturates for long contact times $t_c > 1000$ s. This confirms the qualitative observations made when handling the CCGM out of storage. A CCGM stored during a long time looks more cohesive, although a vigorous shaking of the packing which renews all the contacts seems to diminish the cohesive nature of the sample. In the following, we now refer to "short" waiting time experiments when $t_c = 10$ s, and "long" waiting time experiments when $t_c = 10$ min.

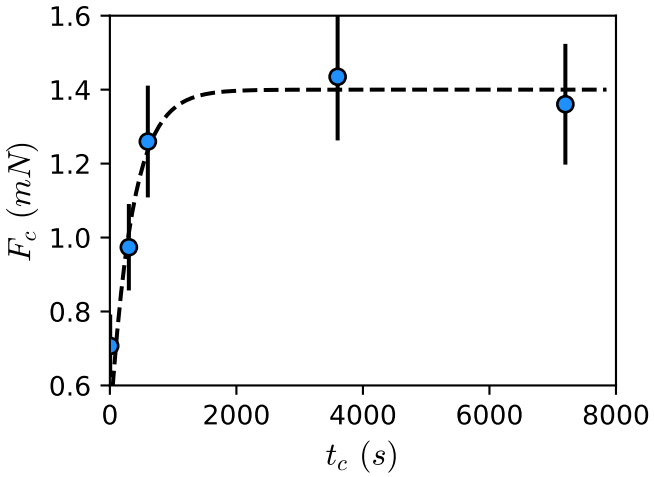

Figure 2.19 – Cohesion force as a function of the duration of the contact. The dashed line is a qualitative trend illustrating an exponential relaxation with time.

The cohesion force distribution has been measured for a hundred pairs of particles out of the same batch ($d = 5$ mm, $b = 2$ μm). The probability distribution function $p(F_c)$ is shown in Fig. 2.20 for short and long contact time. The averaged cohesion force is 0.56 ± 0.1 mN and 1.14 ± 0.3 mN for short and long contact time respectively. For $t_c = 10$ s the cohesion force distribution is narrower than for $t_c = 10$ min. We have not investigated in more details the influence of the contact time and the origin of the force distribution, which are certainly related to the coating property of the particle and to the entanglement dynamics of the polymer chains.

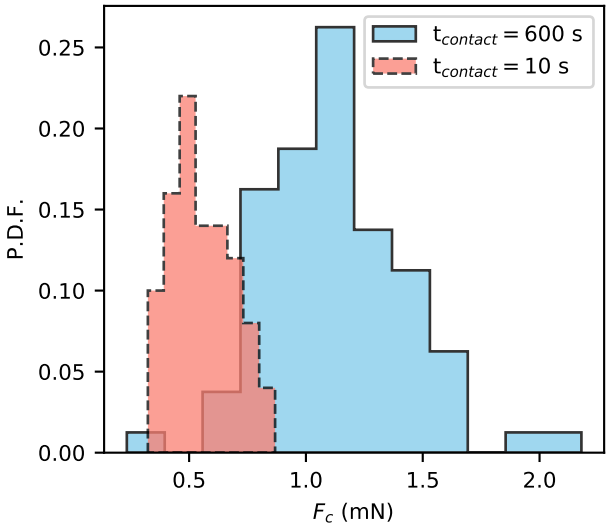

Figure 2.20 – Probability distribution function of the cohesion force measured for approximately 100 pairs of particles, for two different contact times (t_c = 10 s and t_c = 10 min) and for d = 5 mm, b = 2 μm coated particles.

2.3.3 Scaling of the cohesion force

To understand the physical origin of the cohesion force, we systematically study how it varies with the particle diameter d and the average PBS coating thickness b. In Fig. 2.21, the cohesion force is plotted as a function of the particle diameter d for a constant layer thickness $b = 2$ μm, and for the short and long waiting contact times. In the range $0.8 < d < 7$ mm the cohesion force increases with the particle diameter. The cohesion force varies linearly with the diameter for short contact time but exhibits a more rapid increase for long contact time. The linear variation can be well described by a capillary model at contact [49]

$$F_c = \frac{3}{2}\pi\gamma d, \tag{2.6}$$

where the surface tension is $\gamma \approx 24$ mN·m^{-1}, a relevant order of magnitude for PDMS. For long contact times, other molecular phenomena may occur, such as a slow polymer entanglement between PDMS polymers but we did not investigate further the long time correlation between the cohesion force and the particle radius. It is important to note that the contact time effect is more predominant for large particles than small ones. As an example, for $d = 7$ mm particles, the cohesive force is multiplied by 3 for a 10 minute contact time, while it is only multiplied by 1.2 for $d = 800$ µm particles. This element was crucial in the choice of particles used in the experiments presented in the further chapters, which used only small particle of diameter less than 1 mm.

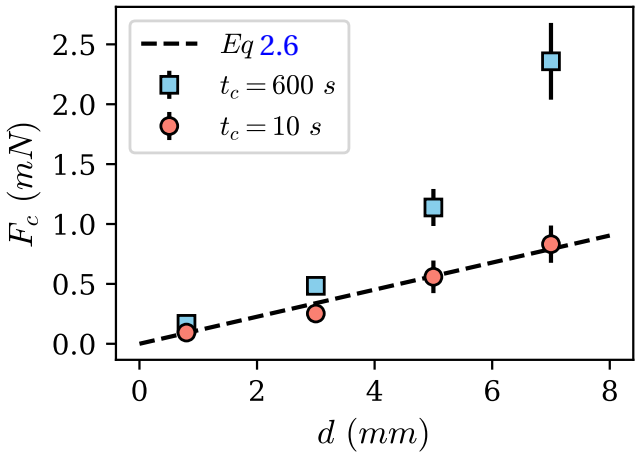

Figure 2.21 – The cohesion force F_c as a function of the particle diameter d for short (10 s) (circles) and long (10min) (squares) contact times. The dashed line is the linear expression (2.6).

The influence of the coating PBS thickness b on F_c is studied in Fig. 2.22(a) for different particle diameters d. The cohesion force normalized by the expression 2.6 is plotted as a function of b. We first observe that all the data obtained for different particle diameters collapse on a single curve. The normalized cohesion force starts from zero when there is no coating, increases and reaches a plateau equal to 1 when the averaged thickness of PBS is larger than 1μm. An ad-hoc expression for the cohesion force can be proposed:

$$F_c = \frac{3}{2}\pi\gamma d\left(1 - \mathrm{e}^{-b/B}\right), \tag{2.7}$$

where $B \approx 230$ nm is a fit parameter which might be related to the roughness of the beads. Indeed, an AFM measurement of the surface of the 800 µm beads (see Fig. 2.22) shows an average roughness of 30 ± 2 nm and a maximum value of 240 nm which corresponds to the order of magnitude of B. This behavior is reminiscent of what is observed with liquid capillary bridges. In this latter case the cohesion force increases when increasing the amount of liquid, up to the point where the liquid screens the surface roughness and that a single bridge exists, giving rise to the saturated force given by equation. 2.6 [60].

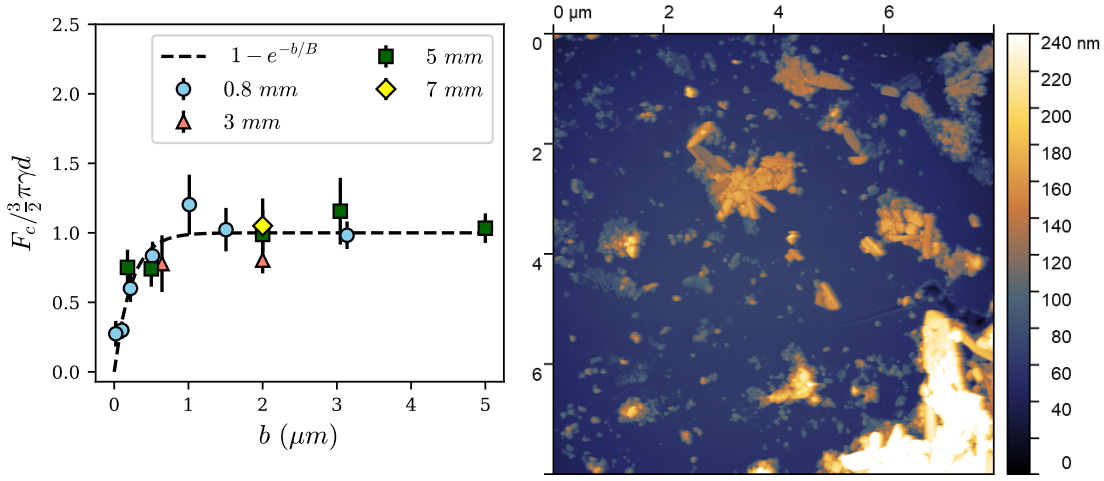

Figure 2.22 – (a) Cohesion force normalized by $\frac{3}{2}\pi\gamma d$ as a function of the mean PBS layer b for short contact times and for different particle sizes. (b) AFM visualisation of the surface of an 800 µm particle.

From equation 2.7, we can write the expression for a Bond number, *i.e.* the ratio of the weight of the particle over the cohesion force, a dimensionless number that will be useful in the following :

$$Bo = \frac{1}{9}\frac{\rho_G g d^2}{\gamma\left(1-\mathrm{e}^{-b/B}\right)}. \tag{2.8}$$

The threshold value $Bo = 1$ gives a critical particle size for which the weight is balanced by the cohesion force. A typical example of $Bo \approx 1$ is given by a coating thickness $b = 2$ μm with particles $d = 3$ mm, illustrated in Fig. 2.3. The stress τ_c measured in section 2.2.3 is a macroscopic measurement of the cohesion, which can be compared to the inter-particle cohesion force measured in section 2.3. From a dimensional analysis, the scaling between the cohesive shear stress and the cohesion force is $\tau_c d^2 \propto F_c$. As presented in section 1.2.5.1, we can use the theoretical expression of Richefeu *et al.* [90] to relate the macroscopic cohesion τ_c to the cohesion force:

$$\tau_c = \mu\sigma_c = \frac{3\mu\phi Z F_c}{2\pi d^2}, \tag{2.9}$$

with μ the friction coefficient, ϕ the volume fraction and Z the averaged coordination number (number of contacts per particle). Fig. 2.23(a) gathers our data for different particle sizes and different PBS coatings and shows a linear trend between $\tau_c d^2$ and F_c although it is not perfect. Choosing the experimental averaged value $\mu = 0.4$ and $Z = 6$, along with the measured ϕ, the theoretical prediction is plotted and gives indeed a good estimate of the measured cohesion. Fig. 2.23(b) also shows that the macroscopic friction coefficient μ, measured using the slope of the linear fit shown Fig. 2.14, seems independent of the coating property of the particles.

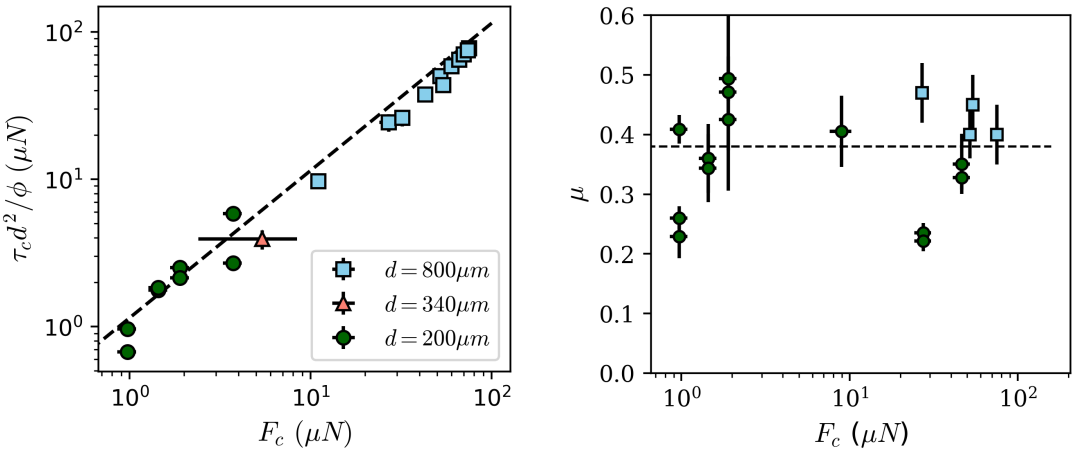

(a) (b)

Figure 2.23 – (a) The macroscopic cohesion force $\tau_c d^2$ measured from inclined plane experiments as a function of the inter-particle cohesive force F_c. The dashed line is the prediction from Eq. (2.9). (b) Friction coefficient μ of the material measured for several F_c.

In this section, we measured the grain to grain cohesion force using 2 setups. First the cohesion of the contact was studied by using the rotating head of a Anton-Parr MCR501 rheometer to measure the pulling force needed to separate two cohesive beads. It appears that the cohesion force do not depends on the pulling force rate, the precompression load or the history of the contact. Then we used a home-designed force measurement device to characterize the distribution of cohesive forces in a prepared sample and to investigate the role of the contact waiting time. These results show that the distribution is pretty homogeneous and the cohesion force increase with time mainly for large beads. We then showed that the inter-particle cohesive force can be modelized by a capillary model at contact and seems to depends on the roughness of the grains. These measured cohesive forces were then introduced in the model of Richefeu *et al.* [90] provide an analytical expression of bulk cohesive stress τ_c measured with the inclined plane experiment in section 2.2.3.

2.4 Conclusion

In this chapter, we presented a method to design a model cohesive granular material made of spherical particles and a polymer coating. Several properties of the material were characterized : angle of repose sensibility to moisture and temperature, durability, and packing fraction. It appears that this cohesion-controlled granular material is not affected by its surrounding environment at usual lab conditions. The cohesive interactions of this material have been characterized through a variety of methods. First at the grain scale we used the high precision of the torque measurement of a

rheometer to measure the inter-particle cohesion force and explore the reversibility of the contact and the role of the precompression load. Then a force balance apparatus was developed to investigate the cohesive force distribution in a sample of grains both at short contact time and long contact time. The link between the inter-particle cohesion and the macroscopic cohesive stress has been investigated and, according to the variation of the cohesive force over time, the $d = 800\mu$m particles seems to be the most appropriate to study the behavior of this cohesive material in flowing configurations. The work of characterization presented in this chapter will be used and tested in the next chapters to investigate the parameters governing the flowability of cohesive granular materials. This method of cohesion control may be extended to other shapes of particles (polydisperse beads or sand grains) provided that silicium is present at the surface of the grains to ensure the sticking of the PBS.

3 The Jet Erosion test as a method to probe the inter-particle cohesion

In this chapter we present the Jet Erosion Test using the cohesion-controlled granular material (CCGM). This work was made in collaboration with Alban Sauret and Mingze Gong at the University of Santa-Barbara (UCSB), and Philippe Gondret at Université Paris-Saclay. Section 3.1 recalls general results on the erosion of a cohesionless granular materials. Section 3.2 presents the experimental methods used to study the erosion of CCGM. The threshold of erosion for various cohesion is presented in section 3.3, followed in section 3.4 by a model to rationalize the effect of the cohesion on the erosion phenomenon.

3.1 Introduction to erosion

The erosion of granular soils is ubiquitous in many fields ranging from civil engineering [137] to aerospace engineering [138]. In these applications, soil stability and the modification of the local topography when the soil is subjected to a fluid stress is a significant issue [139]. For example, this situation is encountered when a rocket takes off or lands due to the turbulent jet induced by the propulsion [140]. This situation is also encountered during measurements of soil cohesion prior to the construction of civil structures [141]. Jet erosion is also of great interest in clean-up processes, such as at nuclear sites that use this process to rid reactor surfaces of harmful particles [142].

In the case of a non-cohesive medium, the erosion of grains by a fluid flow is controlled by the balance of gravity forces, which tend to prevent erosion, and the stress exerted by the flow, which induces erosion and grain transport. The ratio of the force exerted by a fluid stress $\tau_f d^2$ and the apparent weight of a grain $(\rho_g - \rho_f) g d^3$, where ρ_g and ρ_f are the density of a grain and the fluid, respectively, and d is the diameter of a grain leads to the Shields number [143]:

$$Sh = \frac{\tau_f}{(\rho_g - \rho_f) g d} \tag{3.1}$$

Various experimental observations have shown that there is a critical value of fluid stress below which the granular medium is stable, and no erosion takes place. Above this critical value, grains are eroded and transported by the flow [143]. The threshold

value of the Shields number depends on the nature of the flow, laminar or turbulent, but also on the particle Reynolds number, $Re_p = u\,d/\nu$, where u is the characteristic velocity of the flow and ν is the kinematic viscosity of the fluid. Note that in the case of turbulent flows, the transport of grains can also be described by the Rouse number $Rs = U_s/(\kappa\,u)$, which compares the fluid velocity u to the settling velocity U_s of the grain in that fluid [144], where $\kappa = 0.41$ is the Von Karman's constant. Beyond the erosion threshold, the grains are transported by the flow by rolling, or by saltation, or by suspension. A large part of the studies on erosion has considered the erosion of grains subjected to a unidirectional and homogeneous (translation invariant) tangential flow [145, 146, 147]. This is relevant for dune formation in the desert, or for sediment transport in rivers. When the pile of grains is subjected to a flow that is no longer homogeneous, as in a jet, the erosion becomes localized, and it is possible to observe the formation of a crater. In this situation, it is necessary to characterize the complex flow induced by the jet to quantify its impact on the granular environment. A particularly interesting case for civil engineering is the jet erosion test, which consists of impacting a jet perpendicularly to a surface and measuring the depth eroded by the jet over time. Using empirical laws, it is then possible to obtain information on the erodibility of the sediment layer. To refine this model, different studies have considered laboratory configurations of a perpendicular jet impacting a granular bed [148]. Recently, various experimental studies on non-cohesive granular media in air or underwater have shown that the erosion threshold can be predicted using a free jet model, taking into account the position of the virtual origin of the jet [149, 150]. Numerical studies have also shown the relevance of the Shields number to describe the erosion threshold of the granular bed [151]. Whereas the jet erosion test configuration has been considered recently for cohesionless granular material, the influence of cohesion between the grains on the erosion threshold and the shape of the asymptotic crater, *i.e.* the steady morphology observed at long time, remains more elusive since most studies deal with real cohesive soils. Recently, an experimental study by Brunier *et al.* [152] has considered solid cohesive bonds between millimetric grains sizes. Indeed, the use of capillary bridges between the grains is not suitable for erosion experiments since the evolution of the bonds depends on the application time of the hydrodynamic stress and is not suitable in this configuration. The drawback with solid bonds is that once the erosion threshold is reached, the solid bonds break irreversibly and the grains are not cohesive anymore.

Using the knowledge acquired for cohesionless granular material in this field, and the ability to precisely control and measure the cohesion of the CCGM, added to its strong robustness to air condition, studying the erosion threshold of this CCGM constitutes an interesting way to probe the cohesion. Besides, such experiments could help understanding the threshold of transport of cohesive granular materials at the grain scale, which constitutes a first step toward the understanding of flowability.

In this chapter we consider experimentally the erosion of a flat granular bed made of cohesive spherical beads by an impacting turbulent jet. The influence of the cohesive force between the grains is captured through the ratio of the cohesive force F_c to the

gravitational force acting on the particle F_W, $Co = F_c/F_W$. Note that this ratio could also be described through the cohesive Bond number, which is the inverse of the cohesive number. The threshold value $Bo = 1$ corresponds to the situation where the weight is balanced by the cohesive force. The cohesion-controlled granular material allows us to tune finely the cohesive force F_c thus varying the cohesive number at fixed grain size. Using equation 2.3.3, the cohesive number can be defined as:

$$\mathrm{Co} = \frac{1}{9}\frac{\gamma\left(1-e^{-b/B}\right)}{\rho_g\, g\, d^2} \tag{3.2}$$

When the turbulent jet impacts the bed cohesive granular bed at a sufficiently large velocity, the erosion of the grains is observed and leads to the formation of a crater. In this section, we focus on the effects of the cohesion on the erosion threshold. We present in section 3.2 the experimental apparatus. We then focus on the erosion threshold in section 3.3, first considering cohesionless grains ($Co = 0$) and then adding cohesion between particles. We show that the erosion threshold can be rescaled when accounting for the additional force induced by the cohesive bonds, without any adjusting parameter.

3.2 Experimental methods

3.2.1 Experimental setup

The experimental system used to characterize the erosion threshold of a cohesive granular medium is shown in Fig. 3.1. The granular medium is placed in a metallic cylindrical container of diameter 20 cm and height 5 cm. The granular medium fills the container completely, and the surface is flattened before each experiment. A nozzle with an internal diameter of $D = 3.8$ mm and a length of 50.8 mm is centered at the vertical of the granular bed. This nozzle is connected to compressed air via a PVC tube. The experiments are carried out at room temperature ($23.5 \pm 1\ ^o$C) and in this condition the air has a density $\rho_a = 1.19$ kg.m^{-3} and a kinematic viscosity $_a = 1.50 \times 10^{-5}$ m^2.s^{-1}. The distance between the outlet of the nozzle outlet and the surface of the granular bed is varied in the range $H = [1-15]$ cm. The tubing is connected to a valve, which allows us to adjust the flow rate Q_J of the jet, which is measured with a flowmeter. The flow rate is varied in the range $Q = [10^{-5} - 10^{-3}]$ m^3.s^{-1}, leading to an average velocity of the jet at the outlet of the nozzle of $U_J = 4\,Q_J/(\pi\, D^2)$ in the range $[0-50]$ m/s, measured with an accuracy of $\pm 2\%$. The granular samples used for this study are 775 µm spherical glasse beads coated with a polyborosiloxane polymer. The range of coating thickness used is $b = [0-300]$ nm which correspond to cohesive number $Co = [0-9.1]$

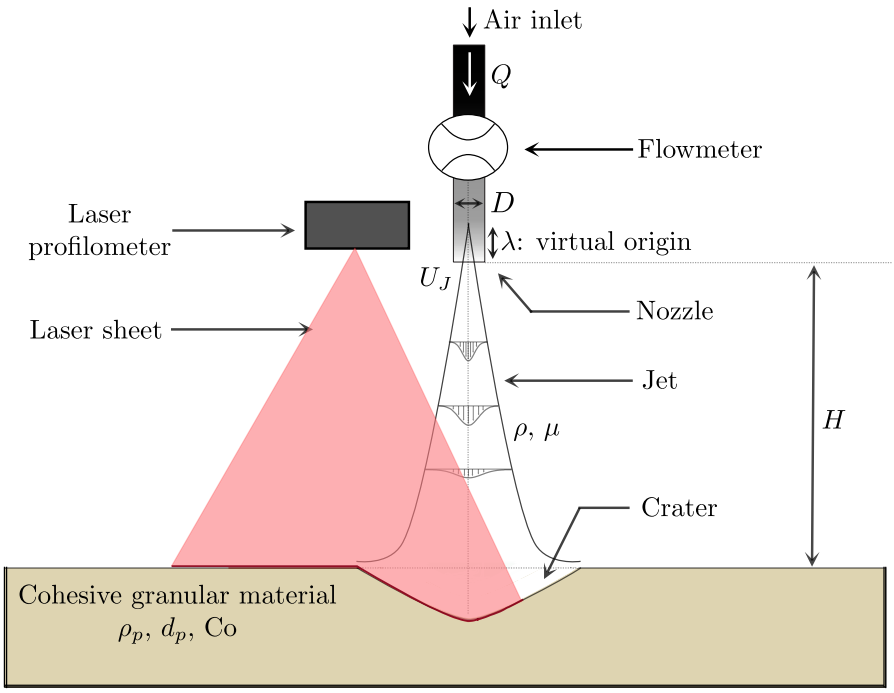

Figure 3.1 – Schematic of the experimental setup. A turbulent jet exits the nozzle of diameter D at the mean velocity U_J and impacts the cohesive granular bed at a distance H.

3.2.2 Experimental protocol

To systematically determine the erosion threshold for different values of the cohesion between the grains and varying distances to the granular bed, we initially prepare the granular bed by pouring a large quantity of grains in the container. We then move a squeegee along the diameter of the container so that the excess grains are removed. The resulting granular material fills the box and exhibits a flat surface, without any noticeable compaction effect. We then place the nozzle at a distance H from the granular bed. The nozzle is then turned on at a low flow rate, well below the erosion threshold. The vertical jet impacts the horizontal surface of the granular bed, and we increase the flow rate, and thus the velocity of the jet, in small increments until the first grains are eroded. The erosion threshold is then determined as the average of the last velocity where no erosion is visible and the first velocity where grains are eroded. The uncertainty on the erosion threshold measurement is the difference between these two velocities.

3.3 Erosion Threshold

3.3.1 Erosion of cohesionless grains

We first consider the erosion of the granular bed made of cohesionless grains to compare our experimental method to the results obtained in the literature. We report in Fig. 3.2(a) the evolution of the threshold velocity of the jet U_J beyond which the jet erodes the grains at the surface of the granular bed as a function of H the distance from the jet. As expected, U_J increase with the distance to the granular bed H. We also notice that, similarly to any erosion process, the threshold velocity increases with the grain diameter. Finally, similarly to in Badr *et al.* [149], we observe a plateau value below a distance $H \lesssim 2.5$ cm for the threshold velocity of the jet, caused by the structure of the turbulent jet.

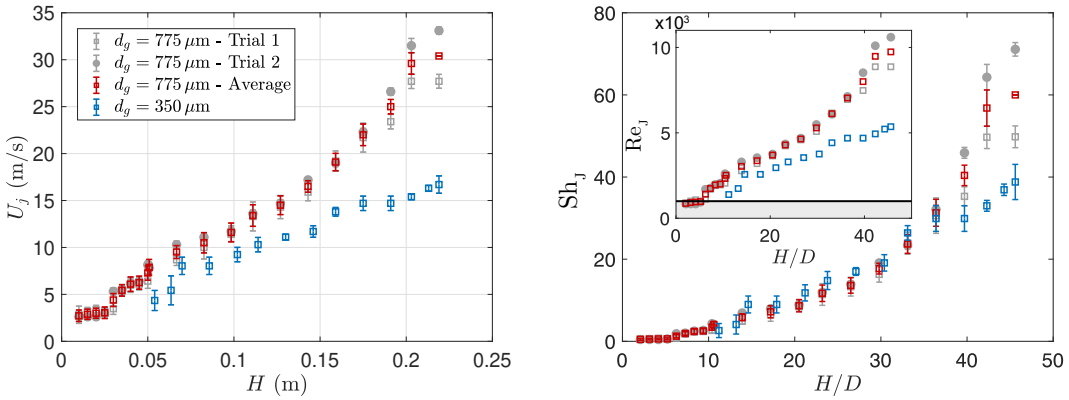

(a) (b)

Figure 3.2 – (a) Mean velocity threshold of the jet at the outlet of the nozzle U_J as a function of the distance between the nozzle and the granular bed H for glass beads of diameter $d = 350\,\mu$m (blue squares) and $d = 775\,\mu$m (red squares). The empty and filled grey symbols show two repetition of the experiments with the $d = 775\,\mu$m grains to illustrate the dispersion of the results. (b) Threshold Shields number based on the velocity at the outlet of the jet, Sh_J, as a function of the dimensionless distance to the granular bed H/D. Inset: Evolution of the Reynolds number of the jet at the onset of erosion as a function of H/D. The horizontal solid black line shows $Re_J = 1000$ delimitating the region of a fully turbulent jet and the region of laminar jet regime.

The relevant dimensionless numbers for this problem are the Reynolds number of the jet at the outlet of the nozzle, $Re_J = U_J D/\nu$, the dimensionless nozzle to bed distance $H^* = H/D$, the particulate Reynolds number $Re_p = u\,d/\nu$, where u is the local velocity evaluated in H, and the Shields number $Sh = \tau_f/[(\rho_g - \rho_f)\,g\,d]$.

We report in the inset of Fig. 3.2(b) the evolution of Re_J with the dimensionless distance to the granular bed H^*. The Reynolds number associated with the jet Re_J is larger than 1000 for all experiments. Therefore, the jet is turbulent, and following the approach of Badr *et al.* [149], we can consider an inertial stress on the particles $\tau_f = \rho_a U_J^2$. The inertial Shields number based on the velocity of the jet at the exit of the nozzle, later referred to as the global Shields number, is

$$Sh_J = \frac{\rho_a {U_J}^2}{(\rho_g - \rho_f) g d}. \tag{3.3}$$

The evolution of the global Shields number is reported in Fig. 3.2(b) for the different sizes of non-cohesive grains considered here. We observe a good collapse of the data, in agreement with the model of Badr *et al.* [149]. We will use this approach in the following section where we are looking for the influence of the cohesion on the erosion threshold.

3.3.2 Erosion of cohesive grains

We now consider the influence of the cohesive force on the erosion threshold. Using the cohesion-controlled granular material (CCGM) we can obtain a range of cohesive numbers, calculated using the equation (3.2), $0 \leq Co \leq 10$ for grains of diameter $d = 775$ µm. We focus on the erosion threshold, *i.e.*, the minimum velocity of the jet U_J such that the first cohesive grains are eroded from the surface of the granular bed. We also report the results for the non-cohesive grains for comparison. Note that the cohesive granular medium considered here does not exhibit temporal variation for the determination of the erosion threshold. Either the grains are eroded at the beginning of the experiments or not at all. Moreover, the repeatability of the experiments is excellent and quantitatively comparable to the cohesionless grains reported in Fig. 3.2(a). We use the same protocol as before: the flow rate Q_J, and thus the velocity of the jet U_J, are gradually increased until the erosion of the first grains at the surface of the granular bed is seen. This delimitates the erosion threshold.

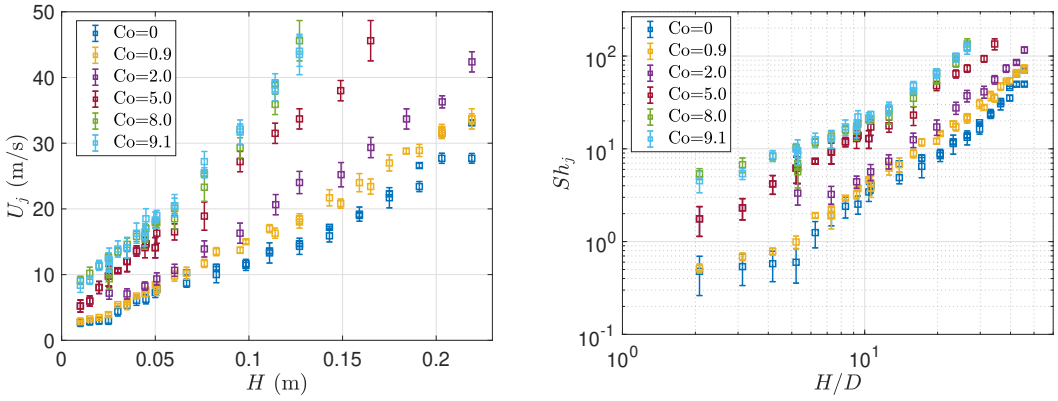

(a) (b)

Figure 3.3 – (a) Mean velocity threshold of the jet at the outlet of the nozzle U_J as a function of the distance between the nozzle and the granular bed H for glass beads of diameter $d = 775$ µm and increasing cohesive number $Co = 0$, 0.9, 2.0, 5.0, 8.0, and 9.1. (b) Corresponding global Shields number, Sh_J, as a function of $H^* = H/D$.

The evolution of the threshold velocity for various cohesion and distance to the granular bed is shown in Fig. 3.3(a). For all cohesive number Co, the velocity of the jet at the outlet of the nozzle increases when increasing the distance to the granular bed. This observation is similar to what we reported above for cohesionless grains. We also observe that for a given distance H to the granular bed, the threshold velocity of the jet U_J increases with the cohesion between the grains. For example, when the nozzle is located at a distance $H = 10$ cm from the granular bed, the velocity of the jet required to erode the cohesive granular medium is between 2 and 3 times larger for non-cohesive grains ($Co = 0$) than for strongly cohesive grains ($Co = 9.1$). Nevertheless, the global trend seems similar with and without cohesion, except a small difference when the nozzle is close to the granular bed where the plateau value seems to disappear for cohesive grains.

We report in Fig. 3.3(b) the evolution of the global Shields number Sh_J as a function of the dimensionless distance to the granular bed H/D. The evolution of the global Shields number for the range of cohesive number studied here exhibits the same trend but seems to be shifted vertically. An increase of the cohesive number Co leads to a global increase of the Shields number. This result is expected since the Shields number is the ratio of the forces eroding the grain, *i.e.*, the drag, and the forces stabilizing it. The weight of the grain stabilizes the grain on the granular soil but if the cohesive number is not zero, it is now necessary to add this stabilizing force F_c. Thus, to reach the same value of the local Shields number allowing the erosion of the grains, the destabilizing force must increase. The velocity at the outlet of the nozzle must be larger, and the global Shields number based only on the gravitational force does not allow to capture this difference. The influence of the cohesive force on the definition

of the Shields number has to be rationalized.

3.4 Cohesive Shields number

3.4.1 Global Shields number

The Shields number is the ratio of the drag force, and the stabilizing forces. For cohesive grains, the stabilizing force is now the sum of the weight of the grains and of all inter-particle cohesion forces acting on a grain. A global cohesive Shields number can be defined as

$$\mathrm{Sh_{J,c}} = \frac{F_J}{F_W + F_{c,\,\mathrm{tot}}} = \frac{\mathrm{Sh_J}}{1 + F_{c,\,\mathrm{tot}}\,/F_W} \tag{3.4}$$

The resulting cohesive force acting on a grain can be estimated as:

$$F_{c,\,\mathrm{tot}} = \sum_{i=1}^{N} \vec{F_{ci}}.\vec{n_i} \tag{3.5}$$

Where, $\vec{F_{ci}}$ is the cohesive force, N is the number of contacts of the eroded grain and $\vec{n_i}$ is a unit vector pointing from the center of the eroded grain in the direction of the drag force. Assuming a homogeneous cohesion, the resulting cohesive force can be estimated [6, 153]:

$$F_{c,\,\mathrm{tot}} = \sum_{i=1}^{N} F_c \cos\theta_i = \alpha F_c \tag{3.6}$$

where θ_i is the angle between the cohesion force vector at the contact of the grains F_{ci} and the drag force. The coefficient α is the resulting prefactor accounting for the number of cohesive contacts and the orientation of the drag force and is of order 1. Assuming a classical disposition of the grains at the surface (thetraedric, pyramidal,etc...), α can be estimated between 1 and 1.5. Using the expression of the cohesive force between two grains (equation 2.7) and the definition of the cohesive number Co, we then obtain a global cohesive Shields number:

$$\mathrm{Sh_{J,c}} = \frac{\mathrm{Sh_J}}{1 + \alpha \mathrm{Co}} = \frac{\rho_a {U_J}^2}{(\rho_g - \rho_a)\, g\, d} \frac{1}{(1 + \alpha \mathrm{Co})}. \tag{3.7}$$

Fig. 3.4 shows the rescaling of the experimental data reported previously. We observe that for all cohesion levels, we can collapse the results on a master curve for $\alpha = 1$. We can also account for the increase in the global Shields number $\mathrm{Sh_J}$ with the distance $H^* = H/D$. To do so, we consider a turbulent jet exiting the nozzle at the velocity U_J. The flow velocity on the axis at a dimensionless distance $x^* = x/D$ from the nozzle is then given by [149]:

$$u_0(x) = U_J \frac{K_u}{x^* + \lambda^*} \tag{3.8}$$

where $\lambda^* = \lambda/D$ is the virtual origin of the turbulent jet, and K_u is a constant [149]. Both parameters depend on the Reynolds number of the jet but can be kept constant at first order. The experiments performed with cohesionless grains of different diameters suggest that the dimensionless virtual origin in the present case is around $\lambda^* \simeq 2$. Therefore, since the flow velocity at the surface of the granular bed is related through the velocity at the outlet by a factor $x^* + \lambda^*$, one expects that the global cohesive Shields number will scale as

$$\mathrm{Sh_{J,c}} = \frac{1}{1+\alpha Co}\frac{\rho_a}{(\rho_g-\rho_a)gd}\frac{u_0(H)^2}{{K_u}^2}(H^*+\lambda^*) = \frac{C\,(H^*+\lambda^*)^2}{(1+\alpha \mathrm{Co})}, \tag{3.9}$$

where C is a fitting parameter that captures the structure of the turbulent jet through K_u, and the local erosion threshold velocity through $u_0(H)$. We observe in Fig. 3.4 that such a prediction captures the evolution of the erosion threshold with the distance to the granular bed for all cohesion levels for $C = 0.029$ and $\alpha = 1$. Note that this expression is valid only sufficiently far from the nozzle when the turbulent jet has a self-similar profile and is thus not expected to be accurate for $H^* \lesssim 10$.

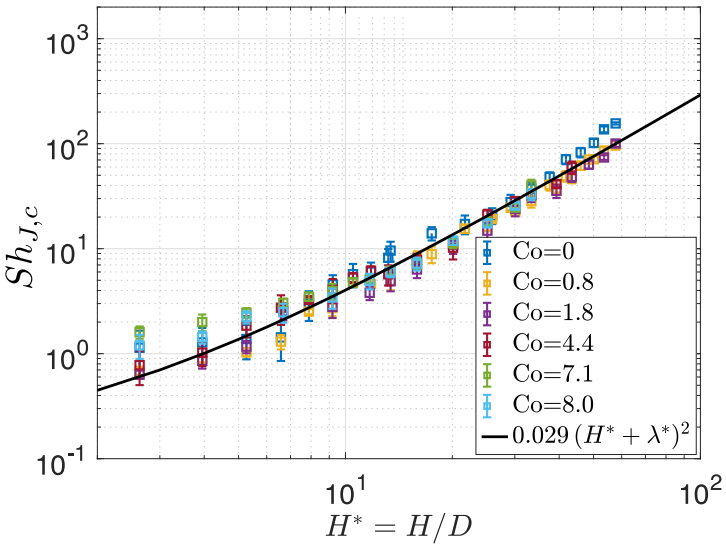

Figure 3.4 – Global cohesive Shields number, $Sh_{J,c}$, as a function of $H^* = H/D$ for the cohesion considered in Fig. 3.3. The solid line is given by Eq. (3.9) for $\alpha = 1$ and $C = 0.029$.

3.4.2 Local Shields number

The local threshold velocity must be the same for a given cohesion whatever the distance of the nozzle to the granular bed is. Therefore, we can also build a local Shields number based on the velocity in the vicinity of the granular bed. The velocity at the surface of the granular bed is given by Eq. (3.8) evaluated at $x^* = H^*$. Note that

this assumes that an order of magnitude of the velocity could be obtained assuming that the granular bed do not modify the jet. This approach was specifically used by Badr *et al.* [149] who have shown that for a cohesionless granular material a local Shields number can be obtained through the expression

$$\mathrm{Sh}_\ell = \mathrm{Sh}_J \frac{(K_u)^2}{(H^* + \lambda^*)^2} \tag{3.10}$$

where K_u depends on the structure of the turbulent jet. Here, we also need to take into account the inter-particle cohesive force to obtain the local cohesive Shields number. As a result, the governing parameter to characterize the erosion of cohesive particles is

$$\mathrm{Sh}_{\ell,\mathrm{c}} = \frac{\rho_a U_J^2}{(\rho_g - \rho_a)\, g d} \frac{(K_u)^2}{(1 + \alpha \mathrm{Co})\,(H^* + \lambda^*)^2} \tag{3.11}$$

and is expected to be of order 1 [149]. We rescaled the experimental data using this expression in Fig. 3.5, and we indeed observe that sufficiently far from the nozzle, typically for $H^* \gtrsim 10$, the experimental results for varying cohesion and nozzle-to-bed distance rescaled on a constant value $\mathrm{Sh}_{\ell,\mathrm{c}} \simeq 1$. Therefore, this dimensionless number catches both the effect of the distance between the nozzle and the granular bed, but also the role of the inter-particle cohesive force on delaying the threshold.

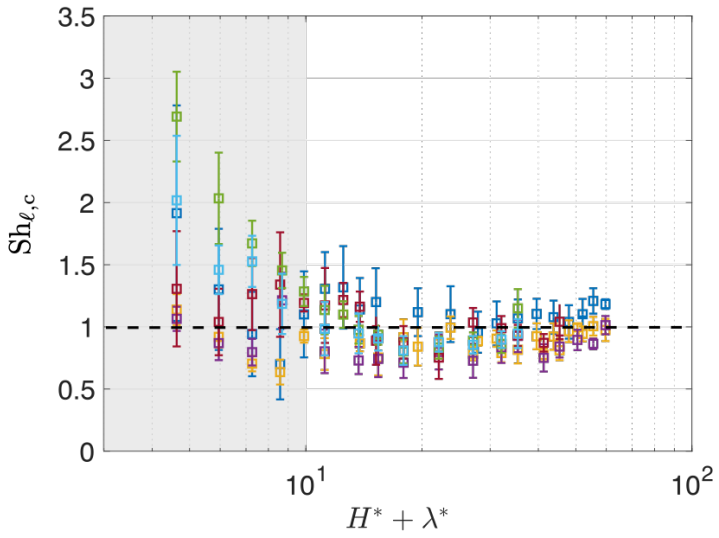

Figure 3.5 – Local cohesive Shields number $Sh_{\ell,c}$ for varying inter-particle cohesion. The color code is the same as in Fig. 3.4 and the horizontal dashed line is $Sh_{\ell,c} = 1$.

3.5 Conclusion and perspectives

In this chapter the CCGM was tested in a Jet Erosion Test configuration. The purpose of this experiment was to understand the threshold of erosion of cohesive grains. We managed to probe the inter-particle cohesion by using a cohesive Shield number that characterizes the threshold at which cohesive grains are eroded when submitted to a fluid stress. This approach constitutes a first test to use the CCGM as a model cohesive granular material, and suggests a deeper investigation to develop a macroscopic transport threshold of cohesive materials. First the velocity threshold of erosion as a function of the distance from the nozzle has been studied for several cohesions. As expected the velocity threshold increases with the cohesion, however the global trend with the distance to the granular bed remains identical. Following the work of Badr *et al.* [149] on cohesionless granular materials, the introduction of the cohesive force as a stabilising force in the Shield number allows to account for the cohesive effect both for a global and a local cohesive Shield number. The fact that we were able to probe the cohesion in a standard configuration suggests that studying the behavior of the CCGM in several configurations, like the discharge of a silo or the collapse of a column, may constitute important steps toward the comprehension of the behavior of cohesive grains, and also bring some innovative tests for the cohesive rheology.

4 The Silo discharge experiment

4.1 Silo Discharge

Another extensively studied experimental configuration for granular materials is the discharge of a silo due to its interest for industrial applications, such as food industry, pharmaceutical industry or storage of granular materials. Since the first studies by Hagen (see the original translation by Tighe [154]), a vast amount of research has focused on the discharge of silo, first with an experimental approach [2, 31, 155, 156, 157, 158, 159, 160, 161], then with numerical simulations [162, 163, 164, 24, 30]. In this section, we will present an overview on the knowledge about the silo discharge for a 2D silo and an axisymmetrical silo.

4.1.1 The Janssen model for a static silo

The classical shape is the cylindrical container filled with a granular material, as seen in Fig. 4.1(a). In 1895, Janssen observed that the pressure at the bottom of a silo saturate when a mass of corn is continuously poured into the silo. He considered a cylinder of diameter D filled with grains of density ρ_p and volume fraction ϕ homogeneous in the silo. To simplify the problem, the following assumptions are made:

— The vertical stress σ_{zz} depends on height and is homogeneous across the section.
— The friction on the side walls is mobilised, so that the upward tangential stress at the wall writes $\tau = \mu_w \sigma_{rr}$, where μ_w is the friction coefficient between the grains and the wall and σ_{rr} is the radial stress.
— The radial stress is proportional to the vertical stress : $\sigma_{rr} = K\sigma_{zz}$, where K is a constant value.

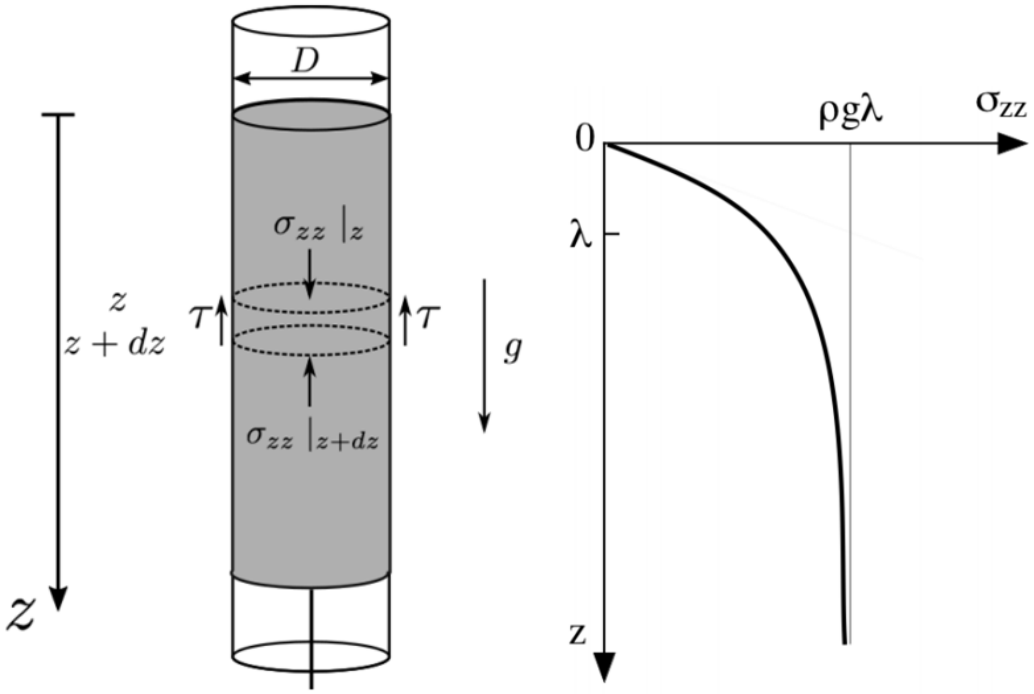

Figure 4.1 – (a) Janssen model : pressure equilibrium on a horizontal slice of the silo. (b) Normal stress as a function of the altitude in a silo filled with granular material, extracted from Andreotti *et al.* [6]

These assumptions lead to the equation of the equilibrium of a slice of granular material :

$$\frac{d\sigma_{zz}}{dz} = \phi\rho_p g - \frac{4K\mu_w}{D}\sigma_{zz} \tag{4.1}$$

Since the vertical stress σ_{zz} depends on z only, and that the stress is zero a the top of the cylinder where $z = 0$, equation 4.2 can be integrated:

$$\sigma_{zz} = \phi\rho_p g\lambda\left(1 - e^{-z/\lambda}\right) \tag{4.2}$$

where $\lambda = D/(4\mu_w K)$ corresponds to a characteristic shielding length above which the normal pressure saturates. In the approximation $z \ll \lambda$ the normal stress increases linearly as $\sigma_{zz} = \phi\rho_p g z$, while for $z \gg \lambda$, the pressure saturates at a constant value $\sigma_{zz} = \phi\rho_p g\lambda$, as illustrated in Fig 4.1(b). This result supports the idea that above a given altitude, the force chains in the granular material creates arches that redistributes the normal stress on the walls, thus fully supporting the weight by wall friction. This model has been confirmed experimentally in various studies [165, 166, 167, 168].

4.1.2 The silo discharge flow rate

The flow of grains through an orifice exhibits different regimes depending on the size of the particles d and the outlet size D. For small orifices $D/d < 4$, there is a high probability for the particles to form an arch at the outlet blocking the flow (see Fig 4.2 (a)). This regime is called the jamming regime, and several studies characterised the conditions required to enter the jamming, and how a perturbation (shaking or tapping) may break the arch and restart the flow [169, 170, 171, 172, 173]. For $D/d > 4$, the flow is irregular, and blocking and flowing phases alternates until the end of the discharge [174, 175]. For a sufficiently high ratio $D/d \gg 4$, the flow can be considered as continuous, and different flow regions appear within the silo as observed in Fig. 4.2. The zone near the outlet of typical size $z \leqslant 3D$ is an acceleration zone where the streamlines are pinched, leading to dead zones at the corners of the silo. Above this acceleration zone, the flow is homogeneous along the silo and the streamlines are vertical. In the following, we will mostly describe this regime.

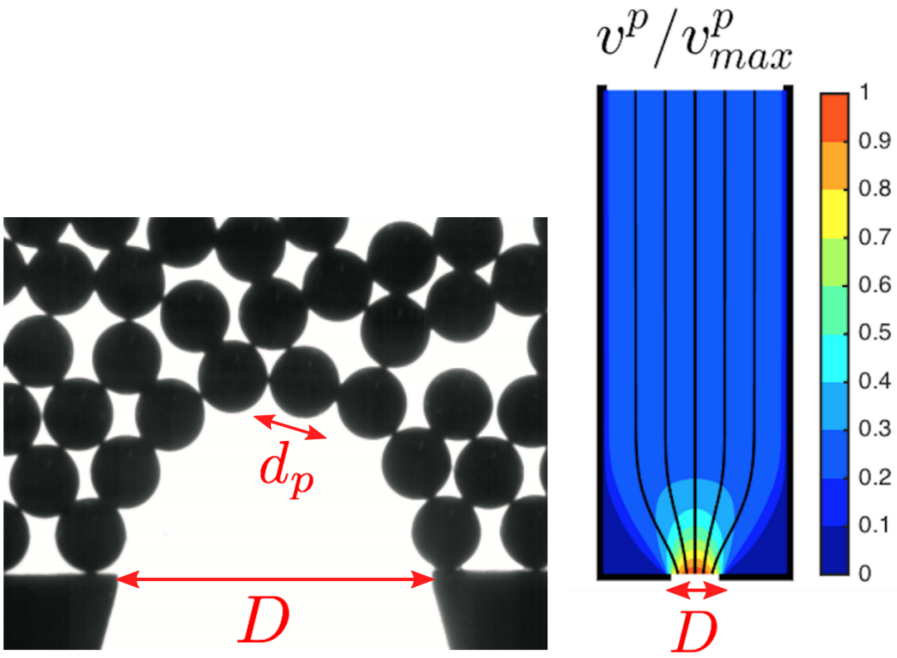

(a) (b)

Figure 4.2 – (a) An arch blocking the flow at the outlet of a 2D silo, extracted from [176]. (b) Velocity field of a continuous simulation of a silo discharge, extracted from [177]

A well known property of the silo discharge is that the mass flow rate is constant over time independently of the height of granular media above the orifice, contrary to liquids, which explains why it can be easily used to measure time in hourglasses. While this hourglass-effect has often been explained by the Janssen model where the stress at the bottom of the silo is independent on the granular height, several experiments

suggest that it is more complex. While the shielding effect still exist when the granular material flows [178, 179], the mass flow rate has been proven to be independent of the pressure at the bottom of the silo [179, 180], therefore the Janssen effect is not the only reason for a constant mass flow rate. Another property of the silos is that the mass flow rate does not depend on the width of the silo as long as it is wide enough compared to the outlet size [2]. Therefore, the only relevant quantity controlling the mass flow rate is the size of the orifice D, whether the silo is 2D or axisymmetric. With a simple dimensional analysis, we can estimate the velocity of the grains at the outlet:

$$v \propto \sqrt{gD} \tag{4.3}$$

Then, considering that the density of the granular media is $\phi_b \rho_p$, and the surface of a circular orifice is $S = \pi D^2$, the mass flow rate Q writes:

$$Q = C\rho_p \phi_b \sqrt{gD^5} \tag{4.4}$$

with ρ_p the density of the particles, ϕ_b the bulk volume fraction of the granular material, and C an empirical coefficient. This formula can be adapted for a rectangular silo of width W [158, 181], the surface then writes $S = WD$, thus the mass flow rate writes:

$$Q = c_D \rho_p \phi_b W \sqrt{gD^3} \tag{4.5}$$

where c_D is also an empirical coefficient. This behavior can be interpreted as the existence of a dynamical arch of characteristic size D below which the particles enter a free-fall regime [1, 154, 182]. While this approach has proven to be relevant for large outlets, several experiments have shown that particles does not exactly enter a free-fall regime. The entire dense medium accelerates continuously along the typical length D above the orifice. This picture is supported by a set of numerical simulations based on the $\mu(I)$ rheology to study the discharge of a continuous granular medium [24, 25, 30, 183, 184] that shows that a visco-plastic rheology based on frictional properties of granular media is sufficient to explain the constant flow rate (see Fig. 4.3).

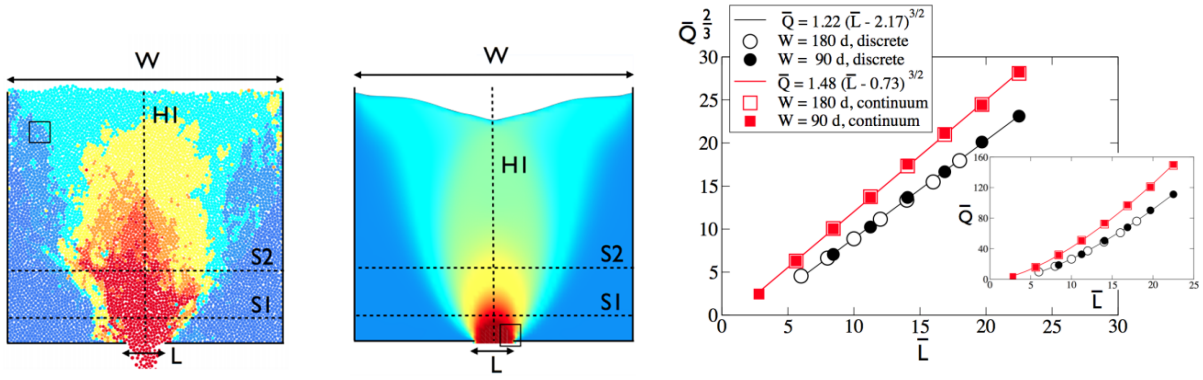

(a) (b)

Figure 4.3 – (a) Discrete silo simulated by Contact Dynamics versus continuum silo simulated by Gerris software. (b) Normalized flow rate $\overline{Q} = Q/gd^{3/2}$ as a function of the normalized outlet size $\overline{L} = L/d$, extracted from Staron *et al.* [25].

4.1.3 Dilation of the medium at the outlet

While the Hagen's law works for $D/d \gg 4$, a deviation from the model is observed when the outlet size is reduced. In this situation, Beverloo *et al.* [155] suggests that particles at the boundary of the orifice are mostly blocked, thus slightly reducing the effective outlet's size. To account for this effect, they propose to modify equation 4.4 as follows :

$$Q = C\rho_p\phi_b\sqrt{g(D-kd)^5} \tag{4.6}$$

where k is a coefficient that depends on the geometry of the silo and on the granular material. This modification can be interpreted as the existence of a "quasi-static circle" of particles jammed at the border of the orifice reducing the effective surface of the outlet. While this approach is quite intuitive, it suggests that the flow at the outlet cannot be considered as a plug flow, but that gradients of velocity and volume fraction exist in the flow trough the orifice. This has been experimentally investigated by Janda *et al.* [158] who measured the velocity and volume fraction directly at the outlet of a 2D silo filled with a monolayer of particles. They observed that the velocity and volume fraction follow self-similar profiles where the value at the center of the orifice is governed by the radius of the silo R :

$$v(x) = v_0\sqrt{1-(x/R)^2} \tag{4.7}$$

and

$$\phi(x) = \phi_0(1-(x/R)^2)^{0.22} \tag{4.8}$$

where v_0 and ϕ_0 are the velocity, volume fraction at the center of the orifice respectively and x represents the horizontal position (see Fig 4.4).

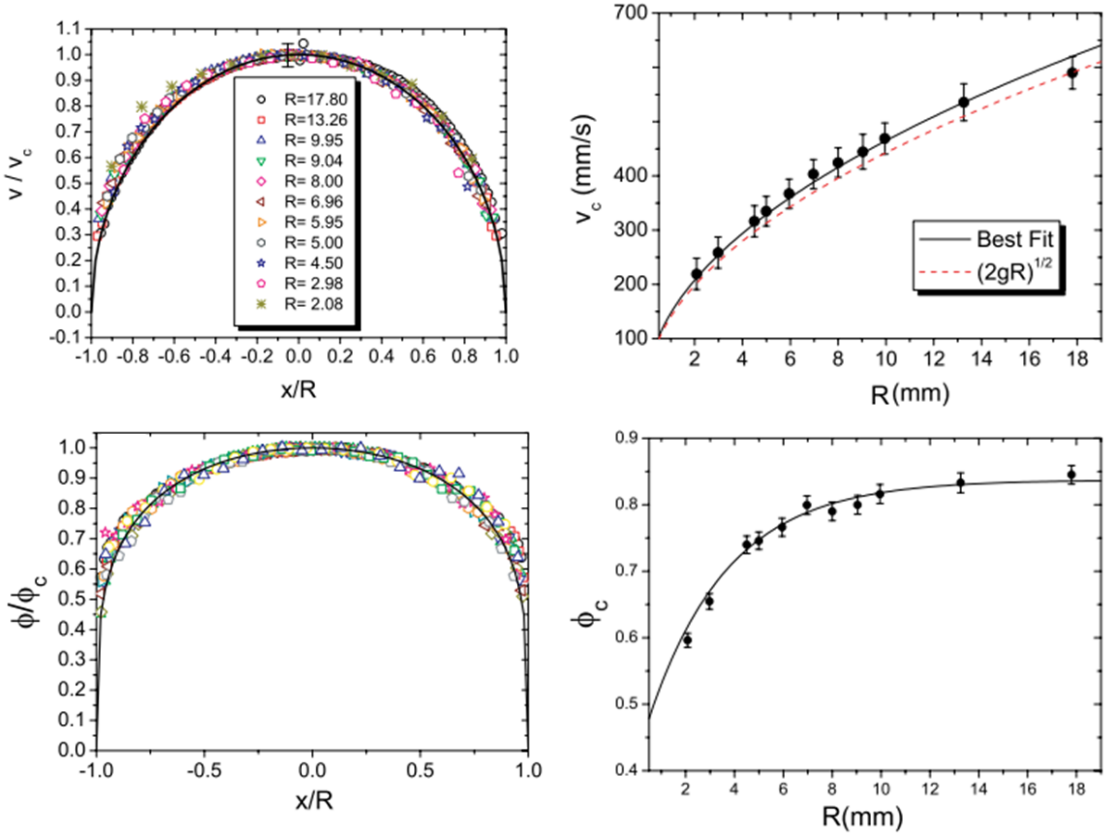

(a) (b)

Figure 4.4 – (a) Velocity and volume fraction profiles at the outlet of a two-dimensional silo and (b), evolution of the velocity and volume fraction at the center of the orifice as a function of its size, extracted from Janda *et al.* [158]

Janda *et al.* [158] observed that the velocity v_0 at the center of the orifice only depends on the orifice size D:

$$v_0 = \sqrt{\gamma g D} \tag{4.9}$$

with an empirical factor $\gamma = 1.1$.

Concerning the volume fraction ϕ_0, several authors observed that the granular media dilates when the ratio D/d becomes too small [157, 158, 181]. They suggest an empirical expression for ϕ_0:

$$\phi_0 = \xi_\phi \phi_b \left[1 - \alpha e^{-\beta \frac{D}{d}}\right] = \xi_\phi \phi_b G\left(\frac{D}{d}\right) \tag{4.10}$$

where ϕ_b is the initial bulk volume fraction, and ξ_ϕ, α and β are fitting parameters.

From an empirical self-similar profile and equations 4.9 and 4.10, one can write the following expression for the mass flow rate for any ratio $D/d > 4$ and every geometry taking into account the dilation of the granular media :

$$Q = c_D \phi_b \rho_p \left[1 - \alpha e^{-\beta \frac{D}{d}}\right] S_0 \sqrt{gD} \tag{4.11}$$

where S_0 is the orifice surface and c_D is a constant. This expression for the flow rate correctly describes experiments for cylindrical and rectangular silos [30, 31, 181, 185] and discrete numerical simulations [31, 161, 186]. As discussed above, the discharge of a silo has been widely studied for granular materials. This experiment has also been used to characterize powders flowability through various methods. For example, Brown *et al.* [37] measured the angle of the "dead-zone" at the corner of the silo, Berry *et al.* [187] and Cannacciuolo *et al.* [188] focused on the arch formation, and Freyssingeas *et al.* [189] investigated the dynamics of the free surface at the top of a circular silo. Other experiments focused on the possibility to facilitate the flow of powders using air flow [188, 190, 191] or vibration [192].

4.2 Preliminary results : characterization of the wall friction

Before the study of the discharge of the silo, we investigate the role of the PBS coating of the CCGM on the wall friction. This section presents a preliminary experiment that characterizes the wall friction of the grains. Fig. 4.5 shows the setup used to characterize the wall friciton of the grains. A PMMA plate is placed on an inclined plane. Cohesive grains are glued on a mobile of mass m and placed on the PMMA plate at the beginning of the experiment. The plate is inclined until the mobile starts to move at an angle θ_c. The friction coefficient μ_w is given by the start angle : $\mu_w = \tan\theta_c$. Start angles are measured for cohesionless grains and cohesive grains of coating thickness b from 50 nm to 155 nm. The angle measurements are averaged over 15 experiments.

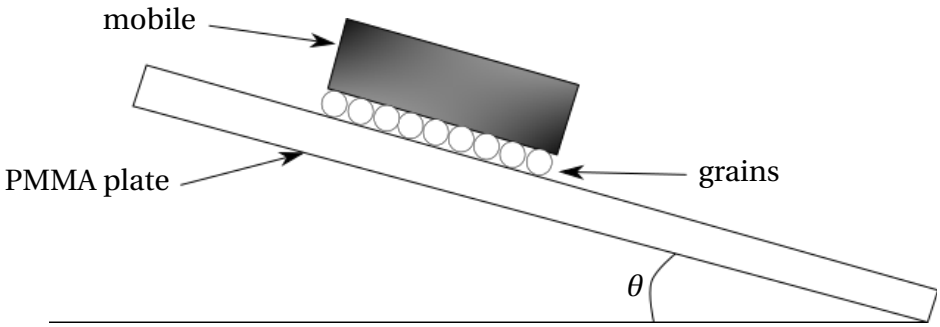

Figure 4.5 – Schematic of the set up used to measure the wall friction of the grains.

The angle measured are quite similar for all batches of grains. The cohesionless

grains starts at an angle $\theta_c = 10.2° \pm 0.5°$ and the cohesive grains starts approximately at $\theta_c = 8.1° \pm 0.4°$. This little difference is hardly significant and shows that cohesive grains do not stick to the PMMA walls at all. This information will be useful in the further PIV experiments.

4.3 Experimental and numerical methods

In this section, we present an experimental and numerical investigation on the flow of cohesive granular materials in a silo. First we will present an experimental work on the effect of cohesion on the threshold of flow. Then we will focus on how cohesion affect the mass flow rate during the discharge of the silo. In order to understand how the velocity of the material and its dilatancy are affected by cohesion, we will study the velocity profile at the outlet of a quasi-2D silo. The experimental results will be compared to continuous numerical simulation based on the 2D Navier-Stokes solver of the Basilisk open-source library (`www.basilisk.fr`).

4.3.1 Silo Experiments

Two configurations are used to study the discharge of the silo. An axisymmetric silo, shown in Fig. 4.6(a), and a 2D silo in Fig. 4.7(a). In both configuration, we investigate how the cohesion is influencing the flow. We first study the effect of the cohesion on the mass flow rate. For both silos, the removable bottom is used to change the size of the orifice from 1 mm to 30 mm (see Fig 4.6(b) and 4.7(b)). At the beginning of the experiment, the height of the column of grain, and the mass of grains poured in the silo gives us the initial volume fraction ϕ_b of the material. When the orifice is opened, the mass flow rate is recorded with a weighing scale with a 20 Hz frequency. In the axisymmetric silo, we performed several discharge experiments by changing the shape of the orifice (see Fig. 4.6(b)) to investigate the role of the geometry of the orifice.

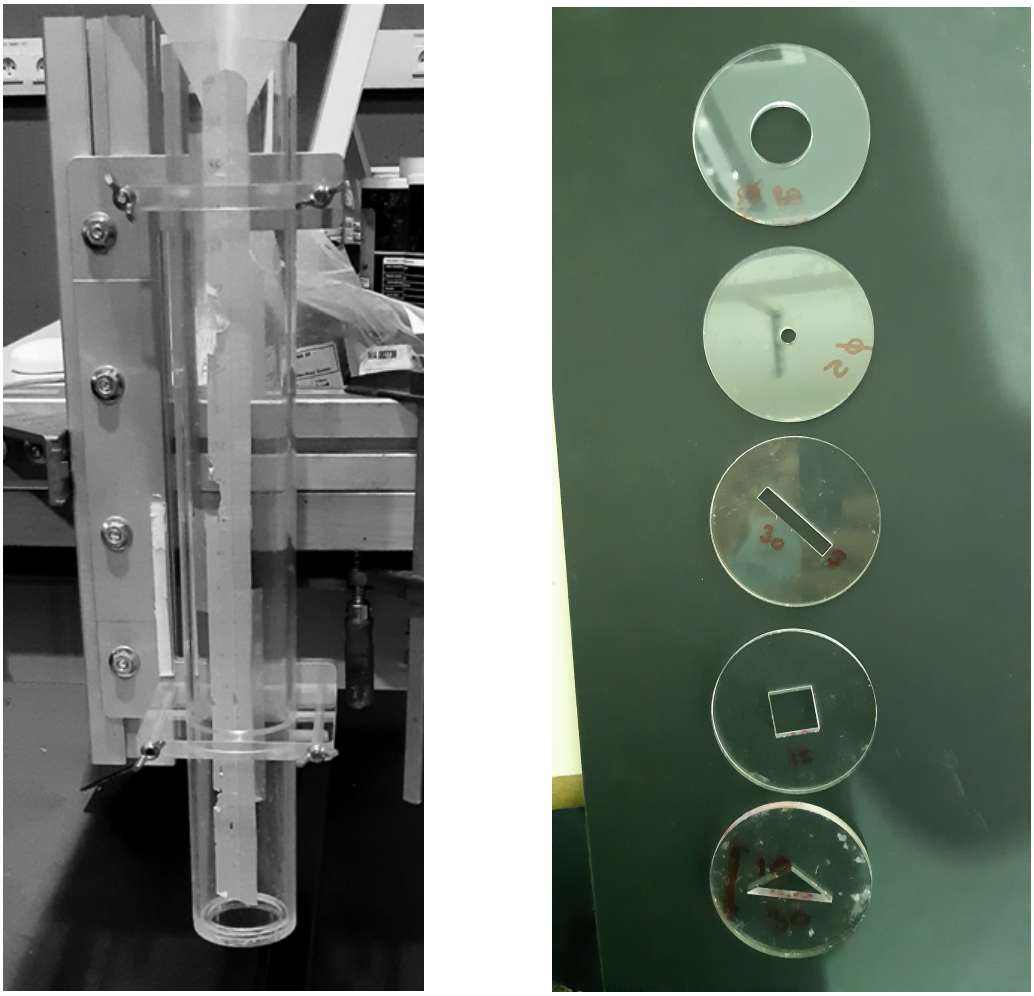

(a) (b)

Figure 4.6 – (a) Picture of the axisymmetric silo of width $L = 60$ mm and height $H = 50$ cm. (b) Several outlets shapes used to perform the experiments.

To study the velocity profile near the orifice, we carried out experiments in the quasi-2D silo (see Fig. 4.7). The velocity profiles were obtained by recording the flow at the orifice with a high-speed camera and processed by a python PIV algorithm (openpiv) to access to the velocity field close to the orifice. The experiments were performed using several batches of particles from cohesionless granular beads to cohesive grains with $\ell_c = \frac{\tau_c}{\phi\rho g} = 2.6$ mm and two grains sizes $d = 800$ µm and $d = 340$ µm.

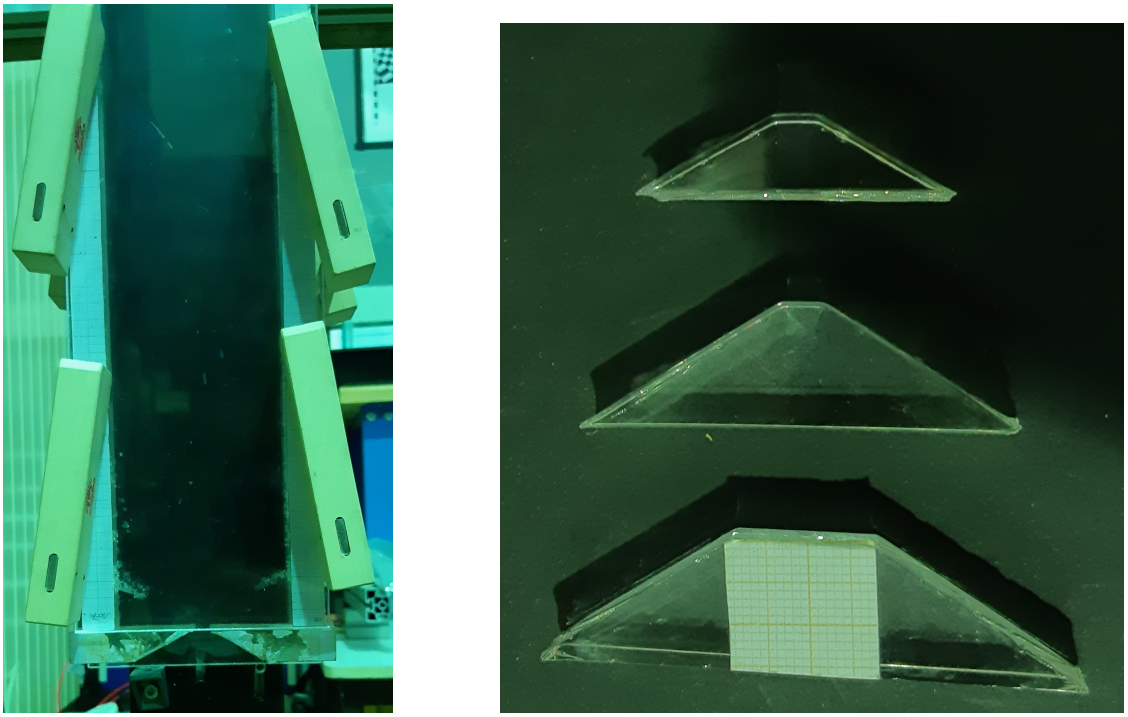

(a) (b)

Figure 4.7 – (a) Photo of the Rectangular quasi-2D silo of width $L = 11$ mm and height $H = 60$ cm with a thickness $W = 2$ cm. (b) Several outlets stopper used to perform the experiments.

4.3.2 Numerical simulations

The experimental results are compared to numerical simulations based on the 2D Navier-Stokes solver of the Basilisk open-source library (`www.basilisk.fr`), using an adaptive mesh and a volume-of-fluid method. The granular flow is simulated using a simple cohesive granular rheology. Without cohesion, the granular rheology can be modelled with the classical $\mu(I)$ constitutive law [26], where the friction coefficient is a function of the dimensionless inertial number I

$$\mu(I) = \mu_s + \frac{\Delta\mu}{I_0/I + 1}, \quad \text{where} \quad I = \frac{\dot{\gamma} d}{\sqrt{P/\rho}} \tag{4.12}$$

For the cohesive granular material, this rheological model is extended by adding the cohesion between particles, which is represented as a yield stress τ_c so that the tangential stress τ becomes

$$\tau = \tau_c + \mu(I)P. \tag{4.13}$$

In the numerical approach, the cohesive length $\ell_c = \tau_c/\rho g$ is chosen as the characteristic length. The plastic criterion and the existence of a yield stress is not strictly captured. A regularization method is then used in which a cut-off of the viscosity

to a finite but high value is introduced for low values of I. In the numerical model, we use the width of the silo L_{num} as the scaling parameter for normalisation to fit with the experiments. The experimental width L of the 2D silo is 11 cm, therefore the numerical width was arbitrary defined equal to 11. The numerical diameter of the outlet is defined $D_{num} = D/L_{num}$ with D in centimeters so the ratio D/L is kept identical for the experiments and the simulations. The cohesive length is defined $\ell_{num} = \tau_c/\rho g L_{num}$ so the ratios ℓ_c/D and ℓ_c/L are also kept identical between the experiments and the numerics. This dimensionless cohesive length is used as the parameter to control the cohesion in the simulations. Although the wall friction is not exactly known for experiments, we assume a no-slip condition at the side walls. Since the numerical model does not include the volume fraction of the material, the simulation may be used to dissociate the impact of cohesion on the rheology and the dilatancy of the material.

4.4 Results from the axisymmetric silo experiments

In this section, we investigate the discharge in a an axysimmetric silo. We first study when the flow occurs as a function of the cohesion in section 4.4.1. Then the study on the mass flow rate during the discharge is presented in section 4.4.2.

4.4.1 When do flow occurs ?

We first investigate the flow threshold for the axisymmetric silo. The cohesive material is poured in the silo using a funnel with continuous stirring to obtain a homogeneous volume fraction. The orifice is initially closed by a stopper, which prevents the fall of grains without penetrating into the granular material. Once the silo is filled, the stopper is removed and we observe whether the material is flowing or not. The results are presented in Fig. 4.8.

On Fig. 4.8, the cohesive length ℓ_c normalised by the size of the grains d is plotted as a function of the hydraulic diameter D_h for several cohesion and outlet's shapes. The hydraulic diameter is defined by the ratio of the surface and perimeter of the outlet $D_h = 4S/P$ where S and P are the surface and the perimeter of the outlet respectively. For a circular shape, the hydraulic diameter is equal to the diameter of the outlet. Empty symbols correspond to experiments where the flow occurs and full symbols corresponds to experiments where the grains stay in the silo after the removal of the stopper. Circles, triangles, squares and diamond symbols correspond to circular, triangular, squared and rectangle outlet's shapes respectively. For cohesionless grains, a threshold is seen around $D = 4d$ which is a known result from a previous study [176]. For a cohesive length $\ell_c/d < 1$, the threshold does not change and is controlled by the diameter of the grains. For $\ell_c/d > 1$, the threshold increase linearly with the cohesive length and the critical diameter of the orifice is $D_h \simeq 4\ell_c$. For cohesive granular material, the results suggest that the cohesive length is playing the role of the

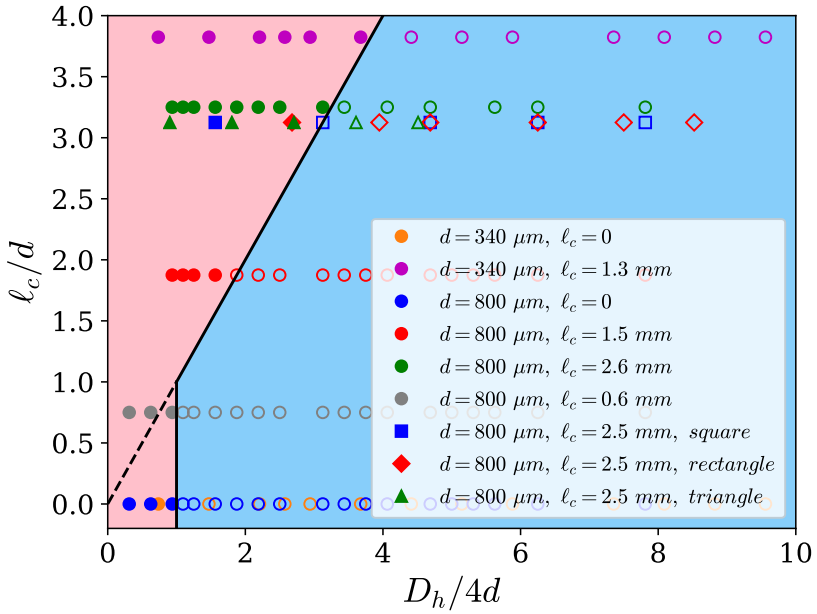

Figure 4.8 – Flow threshold depending on the cohesive length ℓ_c, the size of the grains d and the hydraulic diameter D_h. The pink region is the non-flowing area, and the blue region is the flowing area. Empty symbols correspond to flowing experiments, and full symbols correspond to non flowing experiments.

grains for cohesionless particles. To explain this result, one can consider the balance between gravity and cohesion for a column of material above the orifice :

$$\phi_b \rho g S h = \tau_c P h \tag{4.14}$$

where S is the surface, P is the perimeter and h is the height of the column. Therefore, the threshold is given by $\ell_c = S/P$ which may be rewritten as

$$4\ell_c = D_h \tag{4.15}$$

where $D_h = 4S/P$ is the hydraulic diameter. Equation 4.15 is used to plot the line separating the flowing area (blue) and the jammed area (pink) on Fig. 4.8. This is consistent with the experiment performed with various shapes of orifices presented in Fig. 4.8 and suggests that the characteristic length governing the behavior of cohesive granular materials is the maximum length between the cohesive length and the grain diameter. Considering that result, we introduce the effective size :

$$d^* = max[d, \ell_c]. \tag{4.16}$$

The threshold of flowability is now given, for all materials and outlets' shapes, by $D_h = 4d^*$.

4.4.2 Mass flow rate of the cohesive material

In this section we present the results for the measurements of the mass flow rate through a circular orifice. Since the flow occurs for orifices larger than four times the cohesive length, we now study the effect of the cohesive length on the mass flow rate. A weighting scale is interfaced with a computer by the Labview software and records the flowing mass over time. Fig. 4.9(a) shows a record of the mass measured over time; the slope gives the mass flow rate plotted in Fig. 4.9(b). The peaks observed come from the record of the weighting scale [31]. We average the signal without the peaks to extract the value of the mass flow rate Q.

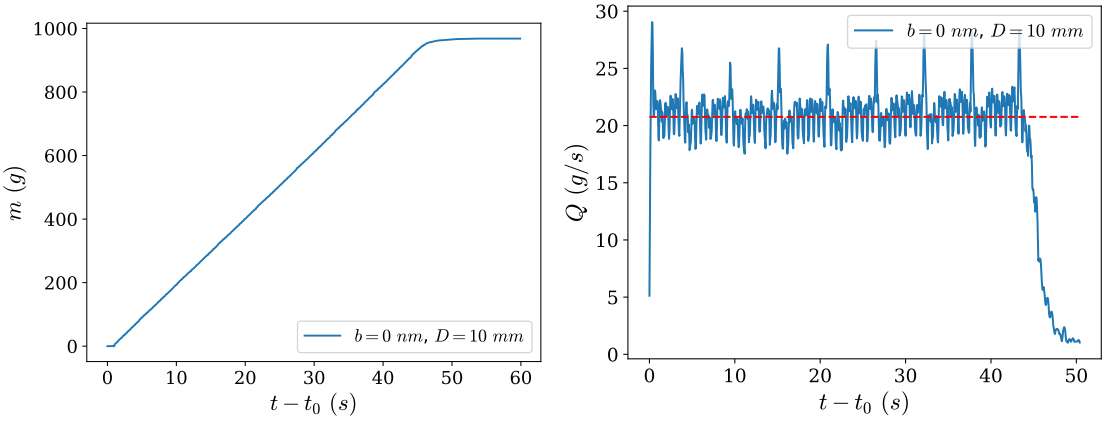

(a) (b)

Figure 4.9 – (a) Mass flowing on the weighting scale over time for a cohesionless granular material. (b) Extraction of the mass flow rate for $D = 10$ mm, $d = 800$ µm.

For the cohesionless experiments, the flow is stationary. Similarly for cohesive experiments, the flow rate is mainly stationary. However for some cohesive experiments, an increase of the mass flow rate has been recorded at the end of the discharge (see Fig. 4.10). This phenomenon has not been investigated in details and the flow rate used in this work is given by the steady state.

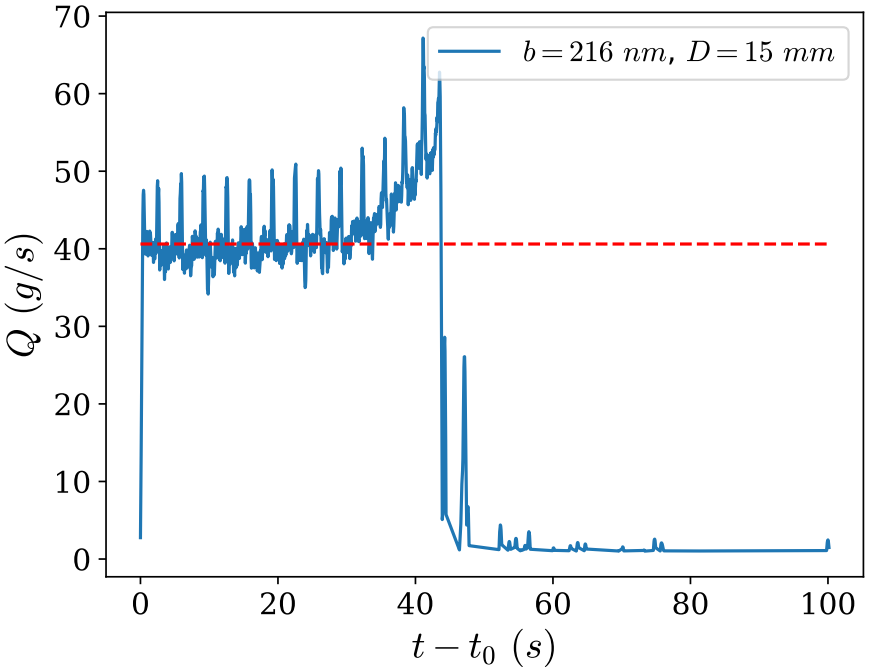

Figure 4.10 – Mass flow rate of cohesive granular materials through an outlet of size $D = 15$ mm for $\ell_c = 2.6$ mm.

Following Benyamine *et al.* [185], we are seeking for a relation between the mass flow rate Q, the size of the grains d and the diameter of the orifice D as supported by equation 4.11 in section 4.1.3. Fig. 4.11(a) presents the mass flow rate measurements as a function of the diameter of the orifice D. For cohesionless materials, the data follow the classical law $Q \propto \sqrt{gD^5}$. The same trend is observed for cohesive materials, even for strong cohesion. However increasing the cohesion decreases the mass flow rate. This shows that the diameter of the orifice is the main parameter controlling the mass flow rate. Cohesion has only a second order effect comparable to the effect of the grain size.

In the framework of Benyamine *et al.* [185], the flow rate can be written as :

$$Q = C\rho\phi_0\sqrt{gD^5} \tag{4.17}$$

with ϕ_0 being the volume fraction at the outlet supposed to be less than the bulk volume fraction ϕ_b, and C is a fitting parameters. Therefore the parameter $\frac{\phi_0}{\phi_b} = \frac{Q}{C\rho\phi_b\sqrt{gD^5}}$ represents the ability of a granular material to dilate at the outlet. This parameter is plotted Fig. 4.11(b) with $C = 0.62$ and shows that for a given size of the outlet D and a given grain diameter d, the dilation effect is stronger when the cohesion increases. However, this interpretation is based on the assumption that the velocity of cohesive granular materials is weakly affected by cohesion and approximately $\sqrt{gD}$. This assumption will be investigated in details in section 4.5.1. For cohesionless

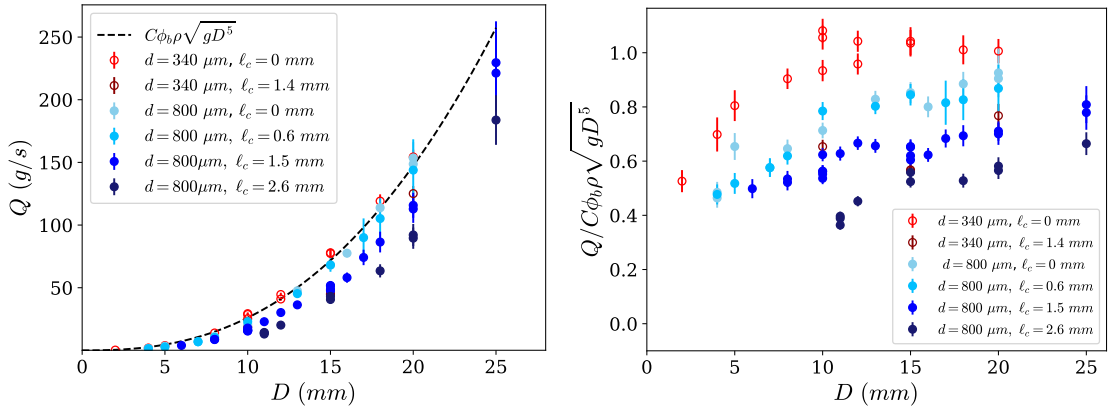

(a) (b)

Figure 4.11 – (a) Mass flow rate and (b) Normalized mass flow rate as a function of the orifice diameter for several cohesion.

materials, ϕ_0 is expected to be a function of D/d (See equation 4.10). The rescaled mass flow rate as a function of D/d is plotted Fig. 4.12(a). For cohesive materials, we see that the trend is similar to cohesionless materials, however, as seen in the previous section, the flow threshold is determined by the cohesive length for cohesive materials. Since the cohesive length acts as an effective grain size for the flow threshold, we suggest to modify the expression 4.11 using $d^* = max[d, \ell_c]$ instead of d. The results are compared to the theoretical prediction in Fig. 4.12(b). All the data collapse on a single master curve given by equation 4.11 and the cohesive length seems to act as an effective particle size for $\ell_c > d$. The vertical dashed line correspond to $D/d^* = 4$ which is flow threshold.

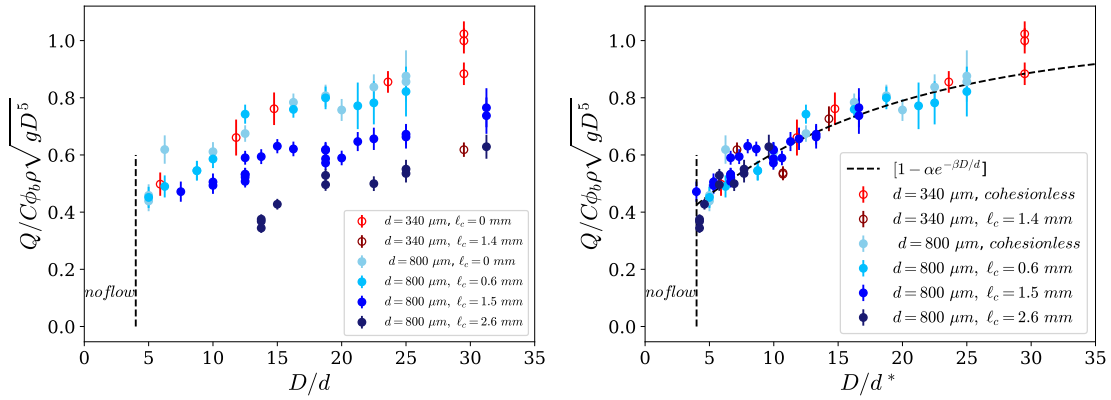

(a) (b)

Figure 4.12 – Rescaled mass flow rate as a function of (a) D/d and (b) D/d^*. Dashed line is given by equation 4.17 with $C = 0.62$, $\alpha = 0.74$, $\beta = 0.063$. and vertical dashed line is the flow threshold.

4.4.3 Effect of the outlet's shape

We have seen that the flow threshold is mainly controlled by the effective grain size $d^* = max[d, \ell_c]$, and that it also controls the dilation of the material. We now investigate the influence of the shape of the outlet on the mass flow rate. Considering that the flow threshold is given by the ratio d^*/D_h where D_h is the hydraulic diameter, we assume that, for non-circular shapes, we can replace the outlet diameter by the hydraulic diameter in equation 4.17. The results of the experiments are plotted in Fig. 4.13.

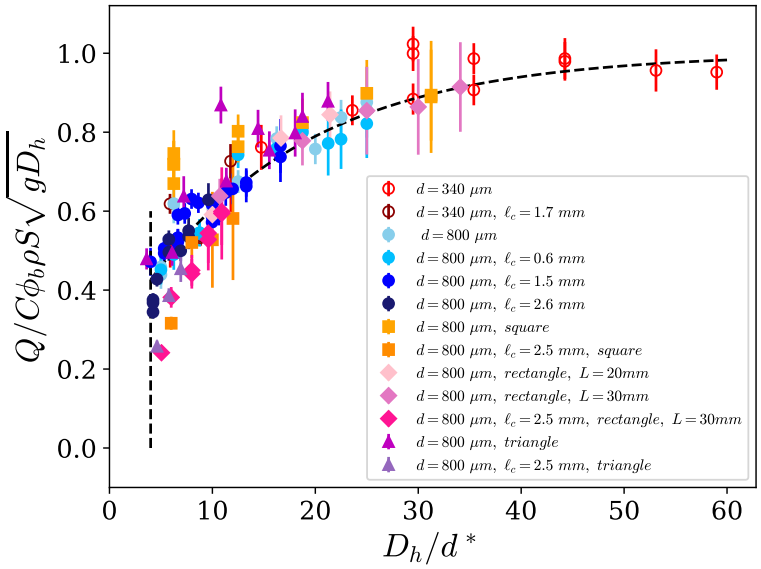

Figure 4.13 – Rescaled mass flow rate as a function of D_h/d^*. Dashed line is given by equation 4.11

The agreement between the experimental data and the model seems quite good. This suggest that the same parameters control both the flow threshold of cohesive granular materials and the flowing behavior. However some experiments seems to barely dilate, like squares close to the cohesive jamming and more experiments need to be performed to characterize the flow close to the flow threshold for "exotic" outlet shapes.

4.5 Results of the quasi-2D silo experiments

In this section, we investigate the discharge of a rectangular, quasi-2D silo. First in section 4.5.1 we will present the effect of cohesion on the mass flow rate, before discussing the velocity profile at the outlet in section 4.5.2.

4.5.1 Mass flow rate

Similarly to the axisymmetric silo experiment, it is possible to record the mass flow rate during the discharge in the quasi-2D silo. The experiments were performed using 800 µm beads of cohesion from $\ell_c = 0$ to $\ell_c = 2.3$ mm. Fig. 4.14(a) shows the mass flow rate Q as a function of the size of the outlet D. As the axisymmetric case, increasing the cohesion decreases the mass flow rate. As seen in section 4.1.3, the mass flow rate for a rectangular silo may be expressed with equation 4.11 which, in the quasi-2D case, writes:

$$Q = c_D \rho \phi_b \left[1 - \alpha e^{-\beta \frac{D}{d}}\right] W \sqrt{gD^3} \tag{4.18}$$

where W is the depth of the quasi-2D silo, and c_D, α and β are fitting parameters. The trend $Q \propto D^{3/2}$ is observed and as in the axisymmetric case, we can rescale all data on a single master curve by using the parameter d^* (see Fig. 4.14(b)).

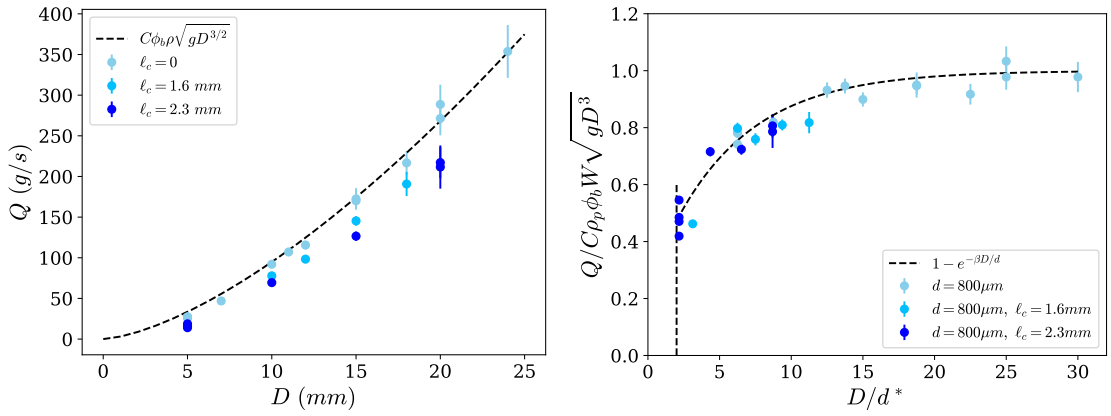

(a) (b)

Figure 4.14 – Quasi-2D silo mass flow rate (a) and normalised mass flow rate (b) as a function of D for cohesive and cohesionless grains. The dashed line is given by equation 4.18 with $C = 0.98$, $\alpha = 0.75$ and $\beta = 0.18$.

The vertical dashed line in Fig. 4.14(b) corresponds to the flow threshold and to a critical orifice $D = 2\ell_c$. This is compatible with the simple argument of equation 4.15 based on the stability of a column above the orifice. Surprisingly, the flow threshold is still $D > 4d$ for the cohesionless case as in 3D, therefore, the flow threshold in the 2D silo is not as straightforward as the axisymmetrical one, and the parameter d^* is only

relevant for $2\ell_c > 4d$ which is always the case for our experiments. The case $2\ell_c < 4d$ has not been investigated. The same remark about the dilation in section 4.4.2 can be made. Under the assumption that the cohesion has little to no effect on the velocity at the outlet, the scaling of all the data with the parameter d^* implies that cohesive granular materials tend to dilate more at the outlet. This assumption is investigated in section 4.5.2.

4.5.2 Velocity profile at the outlet

In this section, we investigate the velocity profile at the orifice of a quasi-2D silo. The PIV method gives access to the velocity field at the wall, close to the orifice. The outlet of the quasi-2D silo is recorded with a high-speed camera at a frequency 1000 fps to track the velocity of the grains over time (see Fig. 4.15).

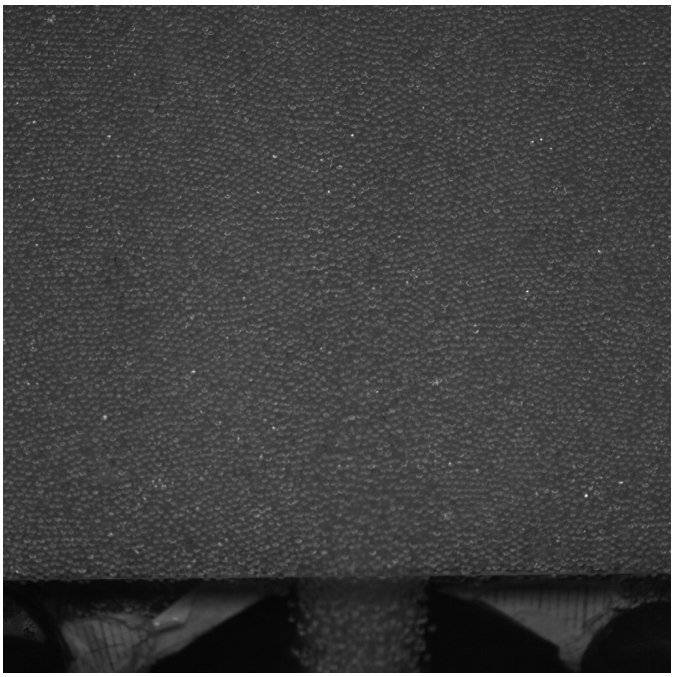

Figure 4.15 – Picture of cohesive granular material ($\ell_c = 2.3$ mm) flowing through an outlet of size $D = 15$ mm.

The difference between 2 consecutive images allows to extract the velocity field for the entire field of view of the camera. In parallel, a code tracking the velocity of some sample grains allows to check the values of velocities given by the PIV. Exemples of velocity profiles are presented in Fig. 4.16 and transformed in color maps of the vertical velocity field in Fig. 4.17. Qualitatively, one observes that the cohesion changes the morphology of the flow inside the silo. Far from the outlet, the flow of cohesive grains occurs in a narrower region above the outlet (Fig. 4.17(b)) than for cohesionless grains (Fig. 4.17(a)).

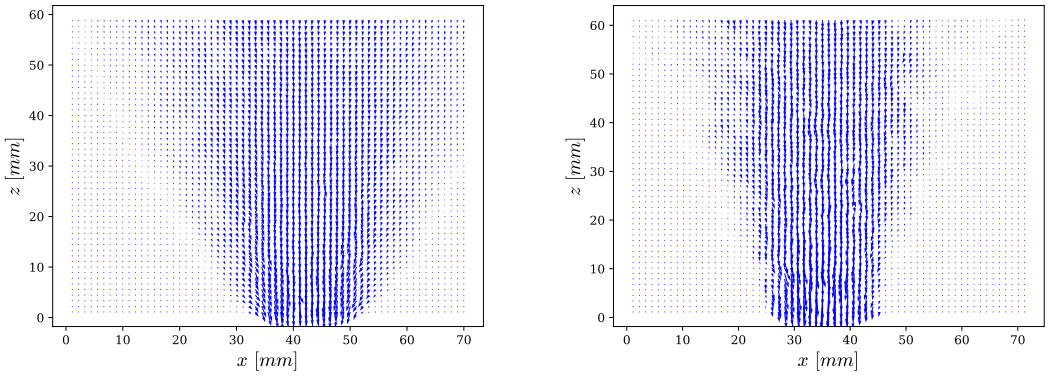

Figure 4.16 – Velocity field of the flowing grains above the outlet for (a) Cohesionless grains and (b) cohesive grains for $D = 20$ mm, $d = 800$ µm and $\ell_c = 2.3$ mm.

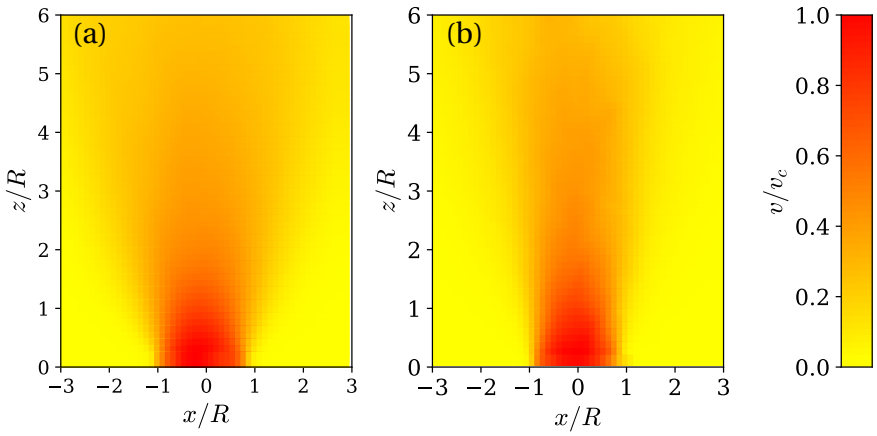

Figure 4.17 – Colormap of the normalised vertical velocity field for $D = 20mm$ for (a) cohesionless grains and (b) cohesive grains, $\ell_c = 2.3mm$, v_c is the maximum vertical velocity at the outlet.

Considering the change in the velocity field above the outlet, we first check whether the self-similarity of the profile is affected by the cohesion. Fig. 4.18 shows the velocity profile normalized by the velocity at the center of the outlet for cohesionless grains (Fig. 4.18(a)) and cohesive grains (Fig. 4.18(b)). Surprisingly, although the velocity field seems to depend on the cohesion, the self-similarity of the velocity profile close to the orifice does not seem to change. This result is consistent with the results of section 4.4: the mass flow rate seems to be governed mainly by the diameter of the orifice.

In the previous section we have explained the decrease of mass flow rate with cohesion by a lower volume fraction, assuming the velocity was unchanged. In order

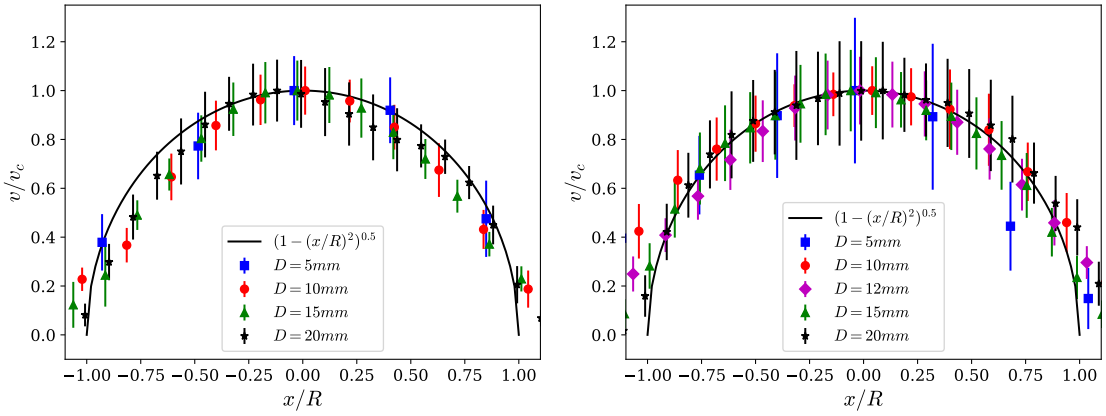

(a) (b)

Figure 4.18 – Normalized vertical velocity profile $v(x)/v_c$ at the outlet for several orifices' size D for (a) cohesionless grains and (b) cohesive grains, $\ell_c = 2.3mm$, v_c is the velocity at the center of the outlet.

to clarify this assumption, we measure the center velocity in the 2D silo and plot in Fig. 4.19(a) v_c as a function of the outlet's size D for several cohesions. First we observe that, even for the cohesionless experiments, a gap exists between the expected $\sqrt{gD}$ power law. That may be due to a wall effect in the velocity captured by the PIV which we assume to be the same for all experiments (the adhesive particles do not stick on PPMA walls). The interesting result in Fig. 4.19(a) is the decrease of the velocity when increasing the cohesion. This observation suggests that the decrease of mass flow rate observed for cohesive granular materials is at least partially due to a decrease of the velocity, and not only to a lower volume fraction at the outlet.

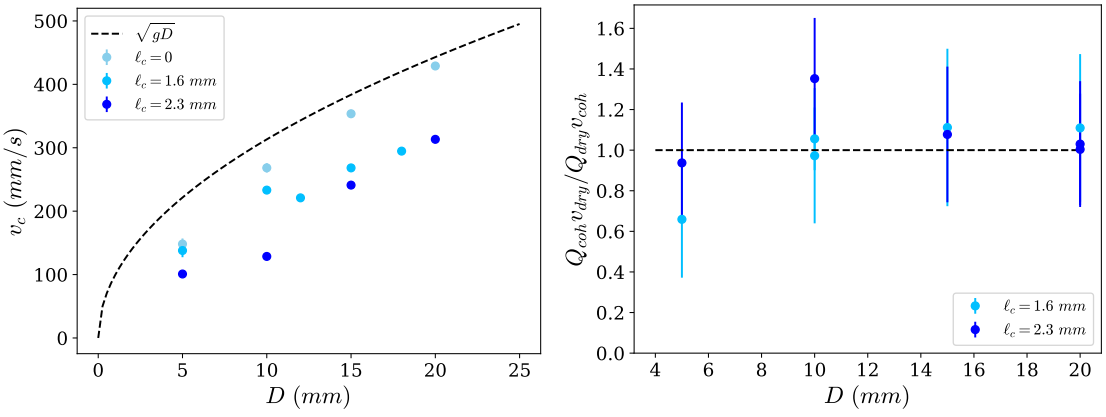

(a) (b)

Figure 4.19 – (a) Central velocity v_c as a function of the size of the outlet D for several cohesion. (b) Cohesive/cohesionless volume fraction ratio as a function of D. Black dashed line corresponds to a value of 1.

An attempt to quantify the relative influence of the change in v_c and ϕ can be made by implementing the ratio of the cohesive and the cohesionless flow rate Q_{coh}/Q_{dry}. The mass flow rate writes in 2D :

$$Q = c_D \phi_{outlet} \rho_p W D v_c \tag{4.19}$$

with $c_D = \int_{-R}^{R} \sqrt{1-(x/R)^2} = \pi/2$ given by equation 4.7. Considering that the profiles are self-similar, c_D is the same for all cases and the ratio Q_{coh}/Q_{dry} is given by the following expression:

$$\frac{Q_{coh}}{Q_{dry}} = \frac{c_D \phi_{coh} \rho_p W D v_{coh}}{c_D \phi_{dry} \rho_p W D v_{dry}} = \frac{\phi_{coh}}{\phi_{dry}} \frac{v_{coh}}{v_{dry}} \tag{4.20}$$

Where v_{coh} and v_{dry} are the velocities at the center of the outlet for the cohesive flow and cohesionless flow respectively, and Q_{coh} and Q_{dry} are the respective cohesive and cohesionless mass flow rates measured by the weighting scale. The effect of cohesion on the volume fraction can be measured through the relative variation of volume fraction :

$$\frac{\phi_{coh}}{\phi_{dry}} = \frac{Q_{coh}}{Q_{dry}} \frac{v_{dry}}{v_{coh}} \tag{4.21}$$

The volume fraction ratio ϕ_{coh}/ϕ_{dry} is plotted in Fig. 4.19(b) as a function of D for two cohesion level. We can see that for each outlet sizes considered, the ratio of the volume fraction is close to 1 which means that the cohesive granular material does not dilate more than the cohesionless granular material at the outlet. To summarize the results, experiments in 2D silos suggest that the decrease of mass flow rate for a cohesive flow is only due to a decrease of velocity at the outlet. The parameter ϕ_0 introduced in equation 4.11 might reflect both the dilation of the medium at the outlet and the velocity. This has already been observed in contact dynamics simulations by Zhou *et al.* [161] on cohesionless granular materials close to the jamming.

4.5.3 Numerical simulations

This section presents the results of a numerical simulation based on the continuous rheology described in section 4.3.2. The simulations provide a map of the pressure and velocity fields for different parameters (see Fig. 4.20).

The simulations are performed for different numerical cohesive length with the same D/L ratio than in the experiments. The velocity and pressure field and the mass flow rate are extracted at each time step. The mass flow rate is measured when the flow becomes steady. Fig. 4.21(a) shows the dimensionless flow rate as a function of the size of the outlet D. In the 2D configuration, we recover the main trend with $Q \propto D^{3/2}$ for every cohesion. However, the influence of cohesion is lower than in the experiments which may be due to the fact that simulations do not account for finite size effects nor dilation. Following what we have done in experiments, we plot in

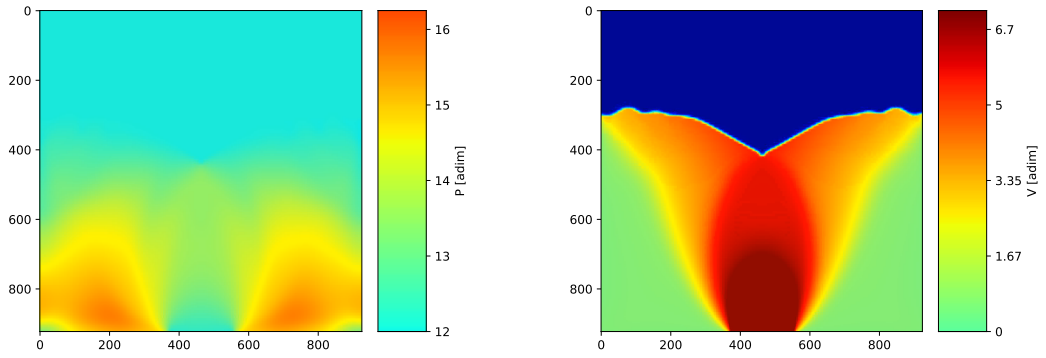

(a) (b)

Figure 4.20 – (a) Pressure field for a cohesion $\ell_{num} = 0.2$. The color gradient goes from blue (low pressure) to orange (high pressure). (b) Velocity field associated. The shape of the surface is also a signature of the cohesion. Quantities are dimensionless.

Fig. 4.21(b) the flow rate normalized by $D^{3/2}$ as a function of D/ℓ_{num}.

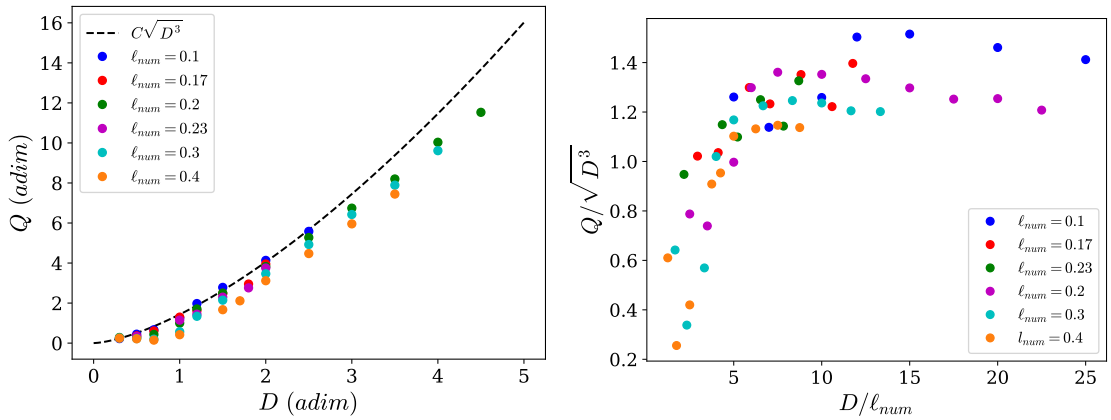

(a) (b)

Figure 4.21 – (a) Mass flow rate and (b) normalised mass flow rate as a function of D for several cohesive materials.

Although the collapse of the data is clearly not perfect, it is interesting to notice that $Q/\sqrt{D^3}$ is not constant for small ℓ_c/D. Since there is no dilation, this is due to a change in the outlet velocity especially for small outlets. This result supports the interpretation that the parameter ϕ_0 introduced in section 4.1.3 contains the decrease of velocity for small outlets sizes.

4.6 Conclusions and perspectives

Using a cohesion-controlled granular material, we have studied the discharge of a silo. First in an axisymmetric silo, we measured the minimum outlet size to get a flow for a cohesive granular material. This threshold depends on the comparison between the cohesive length ℓ_c and the diameter of the grains d, and suggests that the cohesive length screens the diameter of the grains as long as it is larger. The flow threshold may be described entirely by the introduction of an effective particle size $d^* = max[\ell_c, d]$ that describes both cohesive granular materials and cohesionless materials. We have also shown that the flow is mainly governed by the size of the outlet, whether the material is cohesive or not, and that the power law $Q \propto D^{5/2}$ universal.

Our experiments are in agreement with the model of Benyamine *et. al.* [185] as long as the particle diameter is replaced by the effective diameter d^* introduced to describe the flow threshold.

Experiments in a quasi-2D rectangular silo show that cohesion mainly affects the outlet velocity. Our experiments suggest that the parameter ϕ_0 in the Benyamine model [185] might be describing a more complex competition between the dilation of the granular media and the decrease of velocity for small outlets. Numerical simulations based on continuous modelling have been performed, and showed that for small outlets, cohesion induces a lower velocity, although dilation is not taken into account. While the flow of our cohesive granular material seems to be well described by a modified Benyamine model [185], several issues remain and a deeper investigation on the rheology of the CCGM is needed to completely understand the flow behavior.

5 The Granular Collapse experiment

In this chapter, the results of both experimental and numerical investigations of the collapse of a cohesive granular column are presented. We will investigate the effect of the cohesive length ℓ_c on the velocity and the final deposit of a collapsed granular column. Experimental results are compared to a numerical solution arising from a 2D Navier-Stokes solver coupled with a cohesive granular rheology. The numerical simulations and the processing of the numerical data were performed by Anais Abramian at Institut Jean le Rond d'Alembert in the framework of the COPRINT ANR project.

5.1 Introduction to the granular collapse experiment

Among the different experimental configurations (rotating drum, inclined plane, silo discharge), the collapse of a column made of granular material has for many years been investigated as a benchmark test both in experiments [99, 100, 193, 194] or in numerical codes [26, 195]. Also known as dam-break, this configuration is simple and the limited number of geometrical parameters eases the comparison between different studies.

Two main configurations are often used to release the mass of grains. The column can be a cylinder with an axisymmetric spread of grains [29, 196, 197] or a parallelepiped with a flow of grains along a rectangular channel with a single-sided collapse.

In this configuration (see Fig. 5.1), a static column of length L_i and of height H_i is prepared at the left side of a box with a removable gate. A first geometric dimensionless number is the aspect ratio $a = H_i/L_i$. At $t = 0$, the gate is removed, and the granular volume flows down as long as another static configuration is reached. The final width is L_f and the final maximum height is H_f. The morphology of the deposit is mainly controlled by the initial aspect ratio and is slightly dependent on the material properties [100, 198, 199]. The length difference between the final and initial state is the run-out length $\Delta L = L_f - L_i$, and is made dimensionless with the initial length scale: $\Delta L/L_i$. During the collapse, the front moves with a velocity v, and the characteristic time of the collapse if the free-fall time, $t_{ff} = \sqrt{H_i/g}$. A previous experimental study shows that $\Delta L/L_i$ is proportional to a power law of a for a dry granular material [100]:

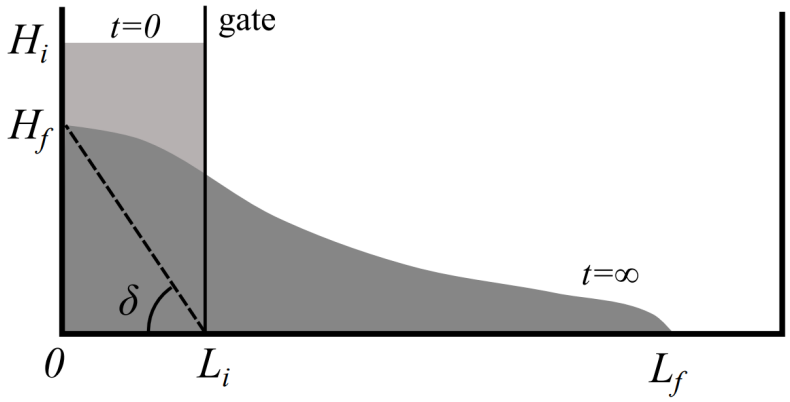

Figure 5.1 – Setup of a quasi-2D granular collapse experiment. The column is characterized by its initial height H_i, and initial length L_i. The final deposit is characterized by its final height H_f and final lenght L_f.

$$\frac{\Delta L}{L_i} \propto \begin{cases} a & \text{for } a \leq 3 \\ a^{2/3} & \text{for } a \geq 3 \end{cases}$$

and (5.1)

$$\frac{H_f}{L_i} \propto \begin{cases} a & \text{for } a \leq 0.7 \\ a^{1/3} & \text{for } a \geq 0.7 \end{cases}$$

The proportionality coefficient depends on the frictional properties of the granular material. These scalings are presented in Fig. 5.2(a) where dimensionless run-out length $\Delta L/L_i$ is plotted as a function of the aspect ratio a for two grain sizes. This shows that the granular collapse experiment is relevant to characterize the frictional properties of granular materials. Considering the dynamics of the collapse, several experiments find out that the velocity of the front is mostly governed by the height of the column. Indeed, the flow goes through three phases: the initiation, the constant velocity flow, and the decelerating phase, lasting $0.8t_{ff}$, $1.9t_{ff}$, and $0.6t_{ff}$ respectively [100, 200]. As an example, these phases are represented in Fig. 5.2(b). Each of these scalings are highly reproducible from an experiment to another, and independant of the experimental conditions. The way to remove the gate does not affect the results of the scaling laws, as long as the gate is removed quickly enough.

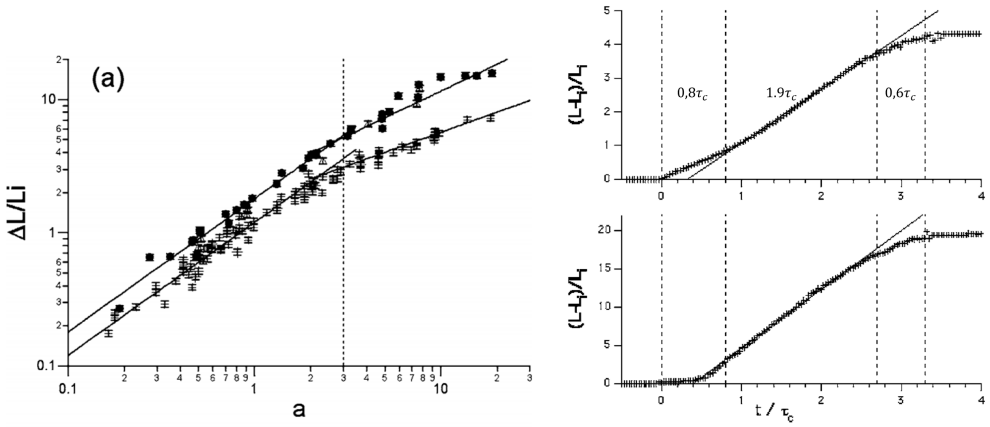

(a) (b)

Figure 5.2 – (a) Scaled runout $\Delta L/Li$ as functions of a. Circles and triangles correspond to experiments performed in a 2D channel working respectively with glass beads of diameter $d = 1.15mm$ or $d = 3mm$. (b) Scaled distance traveled by the pile front as a function of the non dimensional time, for $a = 2.4$ (up) and $a = 16.7$ (down), with $\tau_c = \sqrt{H_i/g}$, extracted from Lajeunesse *et al.* [100].

Cohesive granular media and powders have also been studied with the dam-break setup. For instance, Artoni *et al.* [98] and Wang *et al.* [97] managed to link the run-out length of the collapse to the Bond number of the grains $Bo = \rho g R^2/\gamma$ and the percentage of water of the material. Artoni *et. al* [98] introduced an empirical expression to describe the evolution of the position of the pile foot with time:

$$L(t) = L_0 + \tau V_0 \frac{\sqrt{\pi}}{2}\left[-\mathrm{erf}\left(-\frac{t_0}{\tau}\right) + \mathrm{erf}\left(\frac{t-t_0}{\tau}\right)\right] \tag{5.2}$$

where L_0 is the initial Length of the column, V_0 is the maximum velocity reached $t = t_0$ and τ is the characteristic time of the collapse (see Fig. 5.3 (a)). They characterized the dependencies of t_0 and V_0 with the Bond number Bo and the percentage of water w and showed that the dimensionless run-out length $L^* = (L_f - L_0)/L_0$ may be expressed as $L^* = 2.17\left[1 - \left(Bo^{-1} w^{2/3}\right)^{1/3}\right]$ as shown in Fig. 5.3(b).

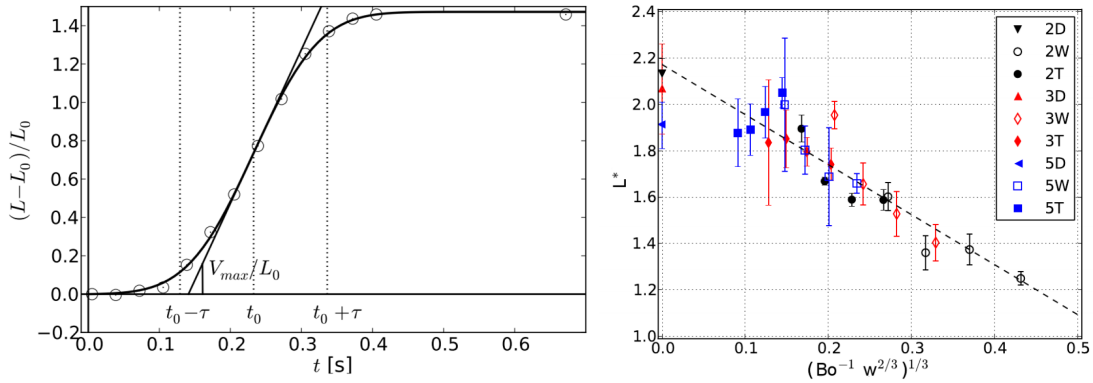

(a) (b)

Figure 5.3 – (a) Example of the runout dynamics for a test with $d = 2$ mm, $w = 1$ %, pure water as a wetting fluid. The symbols represent the experimental data, while the solid curve is a sigmoid fit. (b) Dependence of the dimensionless runout length L^* on the dimensionless number $Bo^{-1}w^{2/3}$. The number in the legend denotes particle diameter, while the letter denotes: D the dry case, W the case with distilled water, T the case with water and a surfactant. Extracted from Artoni *et al.* [98].

Vo *et al.* [201] used the collapse experiment to study the transport and erosion of aggregates of wet granular media. On powders, Meriaux *et al.* [194] studied the cracks and deposit of gypsum powders. An interesting result of this study, that can be seen Fig. 5.4(a) is that the power laws of the collapse does not seem changed by cohesion, but cohesion affects the surface of the deposit, where cracks and irregularities can bee seen in Fig. 5.4(b).

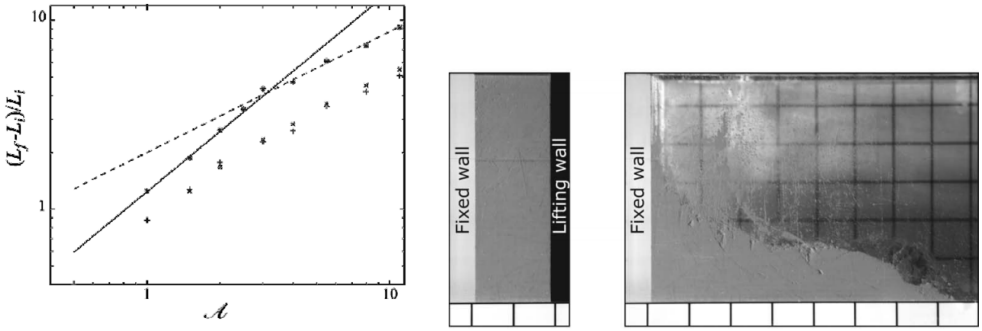

(a) (b)

Figure 5.4 – (a) Run-out length as a function of a for gypsum, for collapse (*) and quasi-static fall (+) and (b) final deposit after collapse, extracted from Meriaux *et al.* [194]

More recently, Torres *et al.* [202] used this apparatus to characterize the flowability of powders, like talc or fertiliser, through various parameters like packing, run-out,

or slope of the deposit. For its high reproducibility, its adaptability to a wide range of materials, and its simplicity, the granular collapse experiment is a relevant experiment to study the frictional properties of cohesive granular materials. In the following we use our controlled cohesion granular material presented in chapter 2 to investigate the role of cohesion on the column collapse.

5.2 Experimental and numerical methods

5.2.1 Experimental methods

In our experiments, the controlled-cohesion granular material (CCGM) consists of glass beads of diameter $d = 800 \pm 60$ μm. The experiments are performed using three batches of grains: cohesionless granular beads ($\ell_c = 0$), and cohesive grains with cohesive lengths from $\ell_c = 2.8$ mm to $\ell_c = 3.6$ mm, respectively.

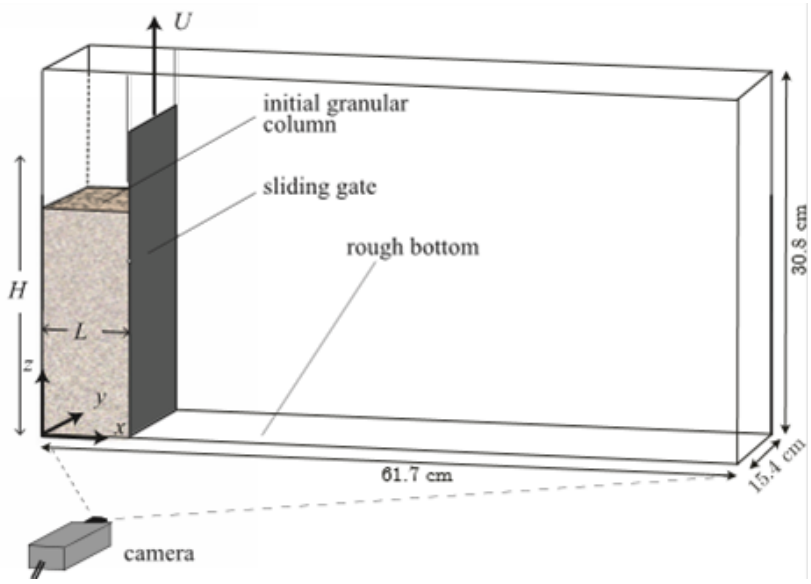

Figure 5.5 – Schematic of the collapse setup showing the initial granular column of width L_i and height H_i.

A sketch of the experimental setup is shown in Fig. 5.5. It consists of a rectangular channel of length 61.7 cm, width 15.4 cm and height 30.8 cm. A removable gate, which slides upwards, allows to build a column of mass M of cohesive grains. The rectangular channel is made of PMMA and the bottom is made rough by gluing particles of the same size as the flowing particles. Since the PBS-coated particles have a very low friction coefficient with the wall material (PMMA), there is no significant lift nor tangential stress observed neither when opening the gate, nor on the side walls. The static column of length L_i and height H_i is initially maintained by the removable

gate. The initial geometry is thus characterized by its aspect ratio $a = H_i/L_i$, which varies in the range $0.7 < a < 7$. At time $t = 0$ the gate is removed vertically, and the granular mass spreads until reaching another static configuration at long time. The final deposit is characterized by its length L_f and its maximum height H_f. The granular collapse is recorded with a high-speed camera (Phantom VEO 710) at 300 fps. For some experiments, a vertical laser sheet along the center of the channel allows a clear visualization of the avalanche profile. An image analysis is then processed to extract the profile of the granular column during the collapse, the front velocity v and the final deposit profile.

5.2.2 Numerical methods

The experimental measurements obtained are compared with numerical simulations using the continuum model described in section 4.3.2. For the cohesive granular material, the classical $\mu(I)$ rheological model is enhanced with the cohesion between particles, which is represented as a yield stress τ_c so that the tangential stress τ becomes $\tau = \tau_c + \mu(I)P$. In the numerical approach, the cohesive length $\ell_c = \tau_c/\rho g$ is chosen as the characteristic length. The plastic criterion and the existence of a yield stress is not strictly captured. A regularization method is then used in which a cut-off of the viscosity to a finite but high value is introduced for low values of I. In the model we assume that the cohesion does not impact the rheological parameters, therefore we choose the values of the parameters close to the usual values present in the literature : $\Delta\mu = 0.12$ and $I_0 = 0.3$. The comparison with the experiments is performed by taking $\mu_s = 0.4$ and the following ratios ℓ_c/H_i, ℓ_c/L_i and H_i/L_i are kept identical to the experiments to allow a direct conversion of the numerical quantities into physical quantities.

5.3 Qualitative observations

When the gate is lifted, four different behaviors are observed, depending on the height of the column and on the cohesion of the material. When the column is not high enough, it remains static, as shown in Fig. 5.6(a). This observation expresses the fact that a minimal height H_0 is required to trigger the flow. For a slightly higher column, the material fractures along a straight line from the pile foot to the top, leading to the collapse of the top right corner of the column (see Fig. 5.6(b)). For a sufficiently high column, and for a sufficiently weak cohesive force between particles, the collapse starts as soon as the gate is removed and the material starts flowing. The column starts to break at an initial angle α_i (see the red line Fig. 5.7(a)) and the mass spreads at a given velocity (Fig. 5.7(b)) until a new static position is reached (Fig. 5.7(c)). A second angle α_f is observed which corresponds to a wedge of material at the bottom-left of the channel that remains non-deformed (see the green line on Fig. 5.7(c)). For a column made with strongly cohesive particles, a noticeable delay between the removal

of the gate and the initiation of the collapse is observed. Beyond these observations, the free surface exhibits a large-scale roughness for cohesive particles whereas a dry granular collapse shows a smooth free surface. In particular, the upper right corner of the initial column seems to be carried by the flow without being sheared or deformed and is present even at the end of the collapse (see Fig. 5.7(c)).

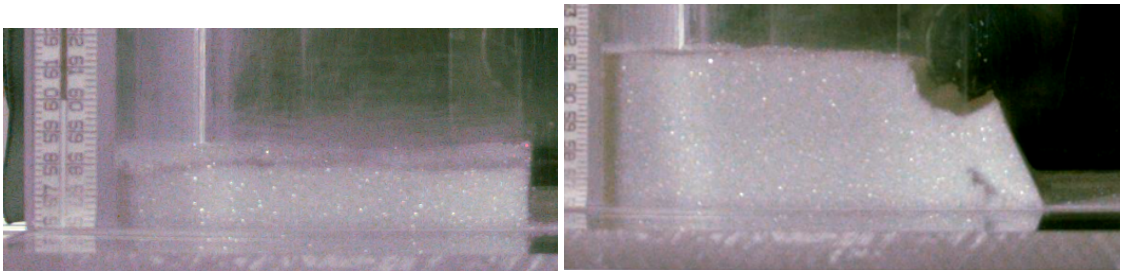

(a) (b)

Figure 5.6 – (a) Cohesive granular column of height $H_i = 2$ cm, and (b) $H_i = 5.4$ cm. In both cases, the coating thickness b is 400 nm.

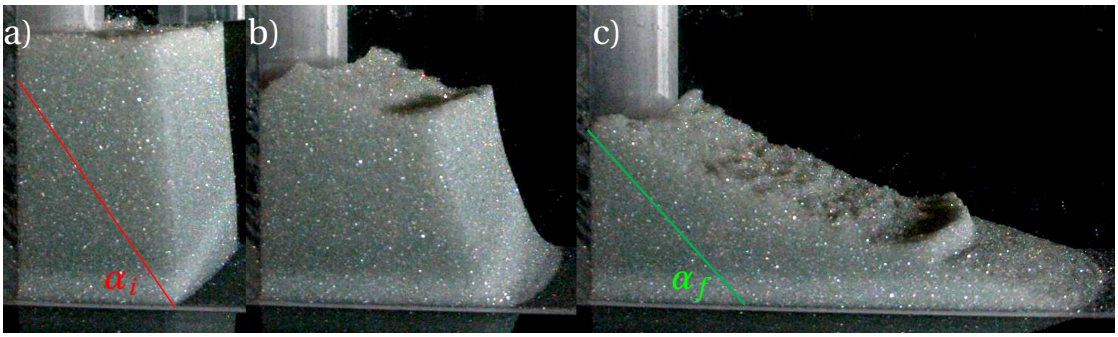

Figure 5.7 – Phenomenology of a cohesive granular collapse. (a) Frame captured just after the gate is lifted at $t = 0$. (b) Above the slip failure depicted by the red line, the volume of grains deforms and flows. (c) The final deposit is characterized by its final height H_f and length L_f. The 'surfing wedge' comes from the top corner that was transported during the flow. It is a signature of the cohesion.

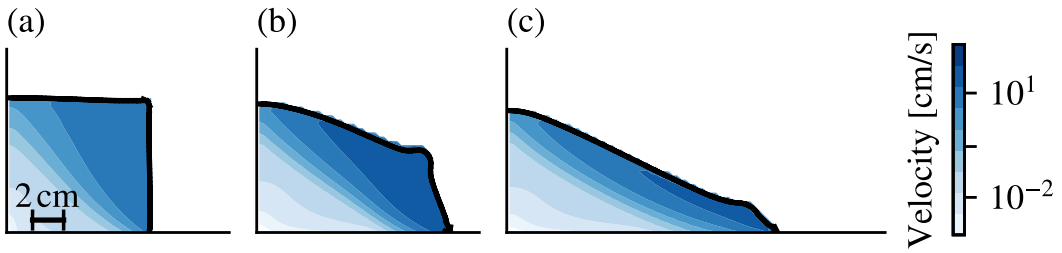

Figure 5.8 – Continuous simulation of the collapse of a column of aspect ratio $a = 1$. The numerical dimensions are converted to physical quantities.

Fig. 5.8 shows a numerical simulation for a cohesive column of aspect ratio $a = 1$. The velocity of the material is plotted as a color scale at three different time of the collapse. As in the experiment, the velocity field displayed in Fig. 5.8(a) shows a wedge of material at the bottom-left of the channel that remains undeformed and the upper part slides above it, however the slip plane do not seems as well defined in the simulations as in the experiments. The material then flows until it reaches a static configuration. As explained in section 5.2, the static state is reached when the value of I reaches a threshold value. The "surfing wedge" displacement is also observed in the numerical calculation: the top-right corner of the initial column seems transported by the collapse flow without being sheared or deformed. The end of the simulation also shows a memory of this surfing wedge (see Fig. 5.8)(c)) as in the experiments. In section 5.4 we will investigate the effect of cohesion on both the initiation angle α_i and the final angle α_f.

5.4 Minimum collapse height and slip failure angle

5.4.1 Measurements of collapse angles

We measure both angles α_i and α_f for cohesive materials of cohesion lengths ℓ_c between 2.8 mm and 4.1 mm for several initial heights. Two methods were used to measure each angle. The initial failure angle α_i is determined by the image difference between the early frame after the failure occurs (see Fig. 5.9(a)). The angle made by the bottom left part of the column that remained static α_f is determined by the sum of all frames of the collapse (see Fig. 5.9(b)).

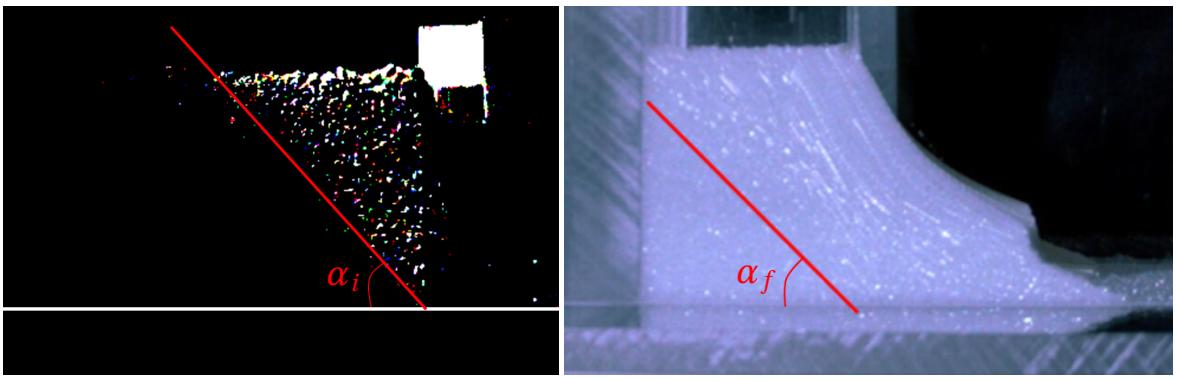

(a) (b)

Figure 5.9 – (a) Image difference between the 10 first frames of the collapse of a granular column, the white triangle part corresponds to the grains moving between two time steps. The limit between the black and white part (red line) is the initial line of failure. The white line is the ground. (b) Sum of every frames of the collapse, the limit between the blurry and sharp material (marked by the red line) gives the limit between the flowing and not flowing material.

Both angles α_i (cross) and α_f (squares) are plotted in Fig. 5.10(a) as a function of the initial height of the granular column. One can see that the initial angle α_i seems to converge to a value close to 55 degrees (see the dashed red line), while the final angle α_f decreases when the initial height increases. Also, below a given height $H_i = 5$ cm, both angles are equal. This is visually explained by the fact that below a given height, the top right corner detaches from the column along a straight line as we can see in the pictures of Fig. 5.10(a). Geometrically, we see that two situations are possible. Either α_i is larger than $\tan a$, which corresponds to a detached corner, or α_i is less than $\tan a$, which corresponds to a column that breaks in two parts from its base. Fig. 5.10(b) shows both the initial angle of failure α_i and the final angle of collapse α_f as a function of the aspect ratio a. The black dashed line represents $\arctan a$. One may observe that the dissociation between α_i and α_f happens for values where $\alpha_i < \arctan a$, therefore this dissociation may be an aspect ratio effect.

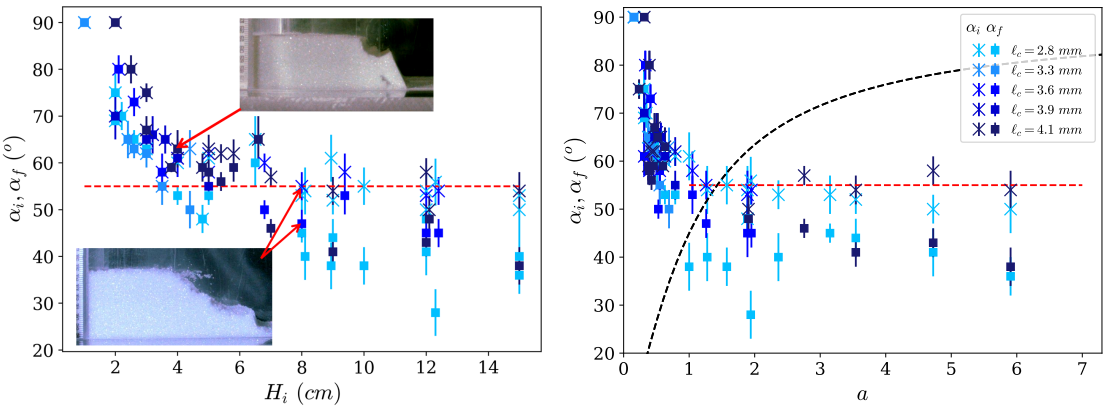

(a) (b)

Figure 5.10 – Measurements of both the initial failure angle α_i (cross) and final angle α_f (squares) as a function of the height of the column H_i (a) and the aspect ratio a (b).

5.4.2 Failure angle measurements in numerical simulations

In order to compare the experiments with the simulations, we used a method similar to the one used in the experiments based on a comparison of the velocity field at different time steps. Fig.5.11 shows how the angles of failure is measured. The initial angle of failure α_i is determined from the difference of the velocity field on 5 time steps (Fig. 5.11(a)). The region of the column which never flows and α_f is determined from the sum of all the velocity fields of the collapse (Fig. 5.11 (b)). An arbitrary threshold of velocity is chosen below which the material is considered static. It is important to note that the numerical angle measurement is not well defined. For instance, two thresholds are represented in the figures, one at a numerical velocity of 0.01 (white markers), and the other one at 0.03 (pink markers). The measured angles seem to be highly dependent on the chosen threshold and no global tendency could be extracted from the simulations.

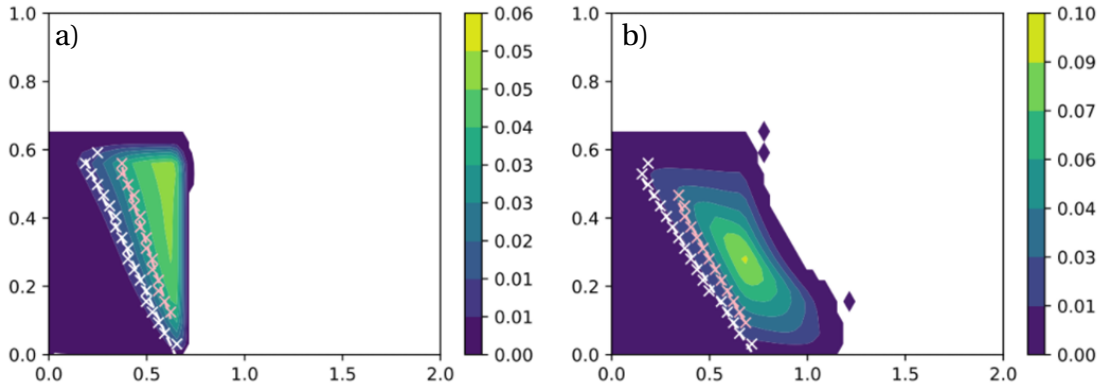

Figure 5.11 – Two methods to measure the angle of failure. Image on the left is a difference of velocity fields of the 5 first time steps to capture the initial fracture angle. Image on the right is the sum of every velocity fields over the time of the collapse. White markers correspond to a plane at a velocity of 0.01 and pink markers correspond to a plane at velocity of 0.03.

However, the limit of stability has already been trialed by Abramian *et al.* [203] using the Basilisk software. Fig. 5.12 shows the result of several simulations performed for ℓ_c/H_i between 0.2 and 1.25, and aspect ratios a between 0.1 and 0.75. Blue markers correspond to stable columns and red markers correspond to collapses. Although a measure of the angle of collapse is tedious, it is easy to measure if a column collapse or not. A clear limit of stability can be seen in Fig. 5.12. For low cohesion levels and high aspect ratios, columns collapse, whereas at high cohesion level and low aspect ratios, columns are stable.

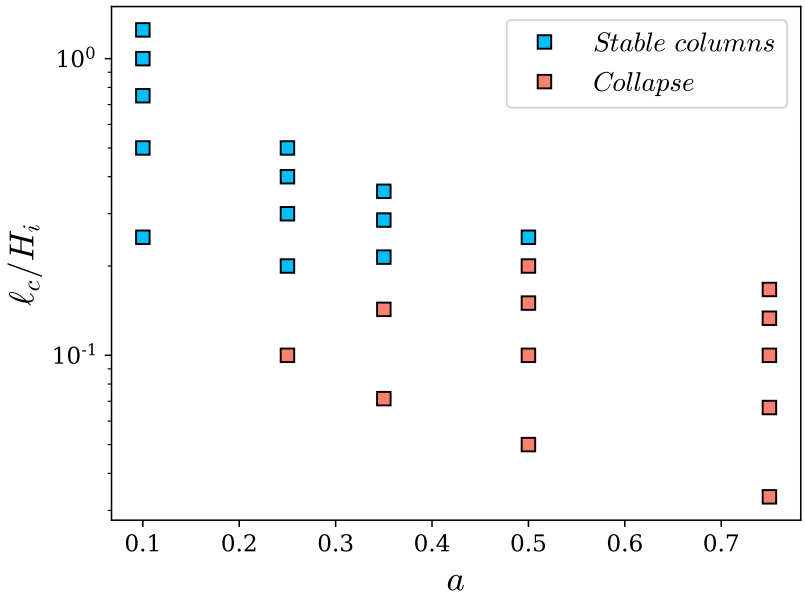

Figure 5.12 – Result of several simulations performed for ℓ_c/H_i between 0.2 and 1.25, and aspect ratios a between 0.1 and 0.75. Blue markers correspond to stable columns and red markers correspond to collapses.

In the following section, we will discuss the failure condition in the framework of a cohesive Mohr-Coulomb plastic criterion.

5.4.3 Condition of stability

The approach of the condition of stability described in this section follows the work of Restagno *et al.* [204]. We first investigate the conditions required to trigger the collapse of a column, and the transition from a single fracture to a flowing material. Several failure geometries have been investigated in the soil mechanics literature, mostly for piles and hills [205, 206, 207, 208]. In this section we will consider the simple case of a cohesive column sliding along a straight plane having its origin at the bottom right base.

5.4.3.1 Small aspect ratio a

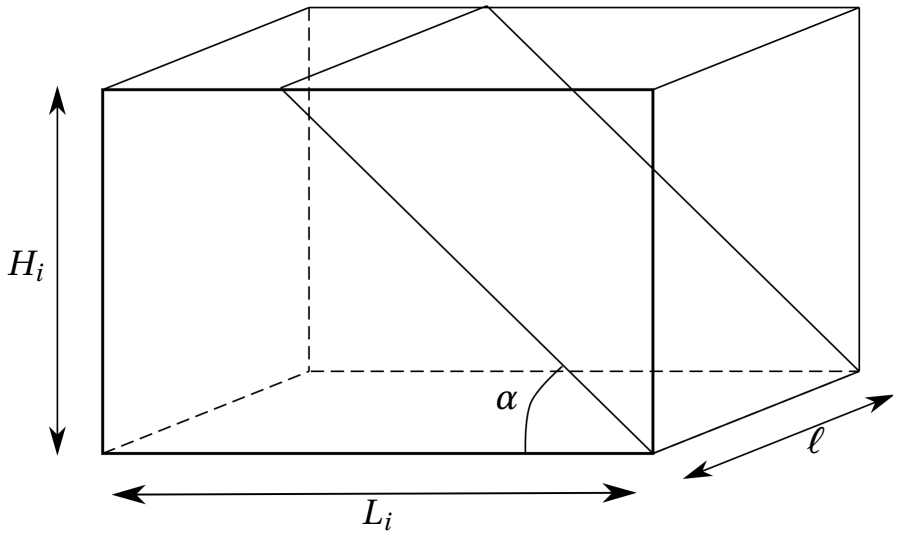

Figure 5.13 – Schematic of the stability of a cohesive granular column. The top right corner rests on a slip plane S inclined at an angle α.

For a cohesive granular material, the stability of a column of height H_i, density ρ, and cohesion τ_c can be described by the Mohr-Coulomb criterion of stability, where we consider the balance between the weight M, the friction and the cohesion τ_c applied by the top right corner on a plane surface at an angle α (see Fig. 5.13) [209, 210, 204]. In this case, the Mohr-Coulomb criterion of failure is

$$\frac{Mg}{S}\sin\alpha \leq \tau_c + \mu\frac{Mg}{S}\cos\alpha \tag{5.3}$$

Using $M = \rho\ell {H_i}^2/2\tan\alpha$ and $S = H_i\ell/\sin\alpha$, the equation 5.3 rewrites :

$$\frac{\rho g H_i}{2\tan\alpha}\sin\alpha\left(\sin\alpha - \mu\cos\alpha\right) \leq \tau_c \tag{5.4}$$

Then we introduce the definition of ℓ_c to obtain the general equation :

$$\frac{\ell_c}{H_i} \geq \frac{1}{2}\left(\cos\alpha\sin\alpha - \mu\cos^2\alpha\right) = f(\alpha) \tag{5.5}$$

One may rewrite equation 5.5 as follows (see Appendix) :

$$f(\alpha) = \frac{\cos\alpha\sin(\alpha-\theta_c)}{2\cos\theta_c} \leq \frac{\ell_c}{H_i} \tag{5.6}$$

The function $f(\alpha)$ is represented as a function of α in Fig. 5.14(a). One may notice that this function describes a parabola centered in an angle α_m where it reaches its maximum value, and becomes zero in θ_c and $\pi/2$. Each colored horizontal line

represents a characteristic cohesion level ℓ_c/H_i : a high cohesion level (blue line) corresponds to a stable column, the red line represents the exact limit of stability given by equation 5.7, and the green line represents an unstable column that may fail at any angle where $f(\alpha) > \ell_c/H_i$.

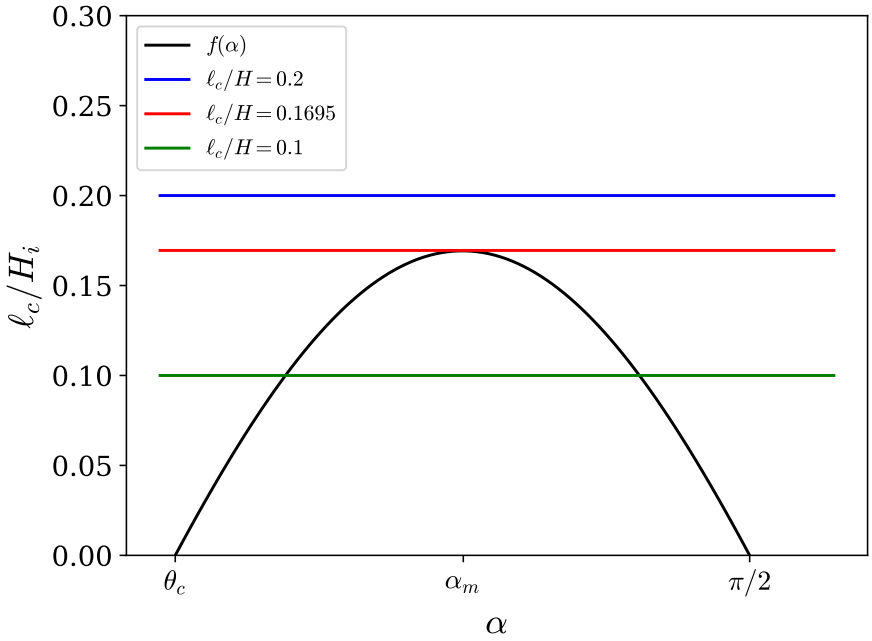

Figure 5.14 – Representation of the function $f(\alpha)$ (equation 5.6). The three cohesion levels displayed represent a stable column (blue), the limit of stability (red) and an unstable column (green).

With this criterion, the column may be considered stable only if the criterion of stability 5.5 is verified for every value of α, *i.e* the maximum value of $f(\alpha)$ is always below ℓ_c/H_i given by the solution of $\frac{\partial f}{\partial \alpha} = 0$ (Red line on Fig. 5.14). Introducing the angle $\theta_c = \arctan\mu$, one may find that the maximum value of $f(\alpha)$ is obtained for $\alpha_m = \theta_c/2 + \pi/4$ (see Appendix). From our experiments we have $\alpha_m = 56°$. After some algebra (see Appendix) one may rewrite the criterion of stability as follows :

$$\frac{4\ell_c}{\sqrt{\mu^2+1}-\mu} \geq H_i \tag{5.7}$$

5.4.3.2 Large aspect ratio a

The previous sections assumed that the stability of a column is governed by the stability of the top right corner of the column. However when the cohesive column are build with a large aspect ratio $a = H_i/L_i$ the weight of material on the slip plane is not the weight of a corner. Fig. 5.15 shows a schematic of a cohesive granular column for

a large aspect ratio. In this case, the assumption is to study the stability of a column where $\alpha < \arctan a$.

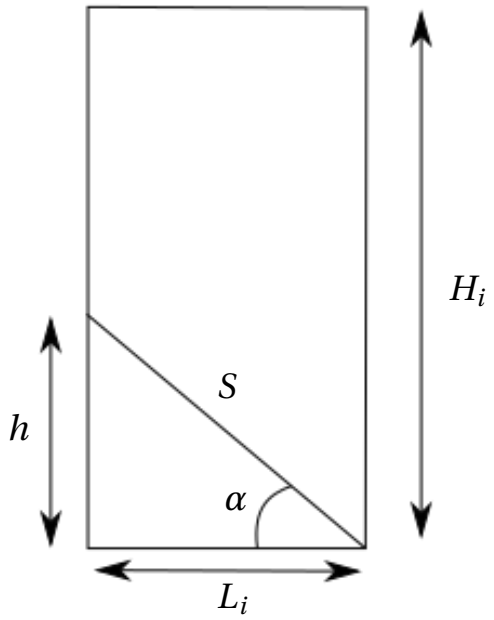

Figure 5.15 – Schematic of the stability of a cohesive granular column. The upper part of the column rests on a slip plane S inclined at an angle α from the horizontal.

In this case, the criterion of stability of the column is :

$$\rho g \left(H_i - \frac{L_i \tan\alpha}{2} \right) \cos\alpha \left(\sin\alpha - \mu \cos\alpha \right) \leq \tau_c \tag{5.8}$$

which may be easily rewritten :

$$f_a(\alpha) = \left(1 - \frac{1}{a} \frac{\tan\alpha}{2} \right) \cos^2\alpha \left(\tan\alpha - \tan\theta_c \right) \leq \frac{\ell_c}{H_i} \tag{5.9}$$

In this case, we see that the aspect ratio plays a significant role, especially for large a. Fig. 5.16 shows several stability curves f_a for several aspects ratio as a function of the angle of failure. We see that an increase of the aspect ratio leads to a decrease of stability. For example, a granular column with a cohesion level $\ell_c / H_i = 0.25$ would be considered unstable for an aspect ratio $a = 4$ but stable for an aspect ratio below $a = 2$. Also, one can see that for a given cohesion level, the aspect ratio opens new possible values of failure angles.

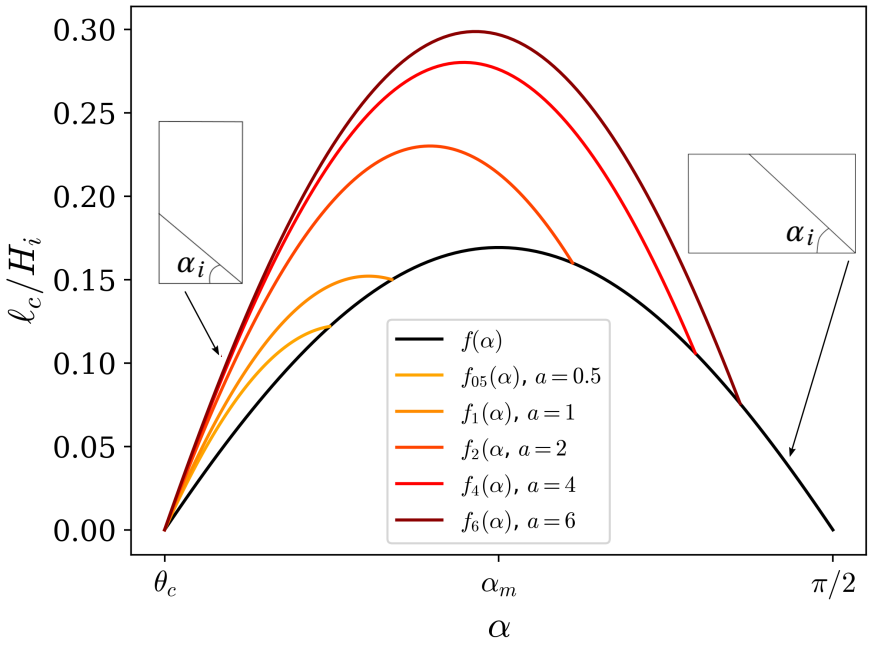

Figure 5.16 – Limit of stability for several aspect ratio. The joining point between $f(\alpha)$ and $f_a(\alpha)$ corresponds to $\alpha = \arctan a$.

Fig. 5.17 shows the results of both experiments and numerical simulation. The cohesion level ℓ_c/H_i is plotted as a function of the aspect ratio a. The limit of stability is given by the black line that separates the stable area (blue) from the collapse area (pink). The plateau at low values of a is given by equation 5.7. The discontinuity of the limit of stability is due to the effect of the aspect ratio and is evaluated at $a = 1.2$. Blue symbols corresponds to stable columns and red symbols correspond to collapsing columns. We observe that the theoretical stability limit captures the behavior of the columns at low aspect ratios. Unfortunately, we performed no experiment to investigate large aspect ratios and large ℓ_c/H_i simultaneously. Nonetheless this opens new perspectives to study the limit of stability of cohesive granular columns.

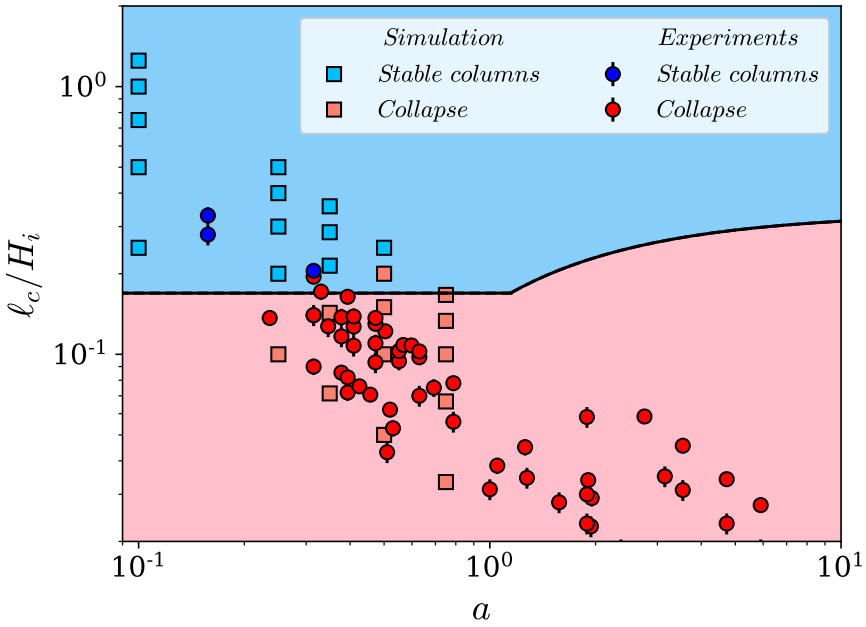

Figure 5.17 – Stability map for a cohesive granular column. Black line is the limit of stability. the plateau at low values of a is given by equation 5.7 and the discontinuity of the limit of stability is due to the effect of the aspect ratio and is evaluated at $a = 1.2$. Blue symbols correspond to stable columns and red symbols correspond to collapse.

5.4.3.3 Selected angle of failure

In this section we focus on the low aspect ratios $a < \tan(\alpha)$ where $\alpha_f = \alpha_i$. In this configuration the right corner of the column breaks along a slip plane. While the threshold of stability calculated previously predicts the maximum height of stability, this approach does not allow to predict the observed angle of failure.

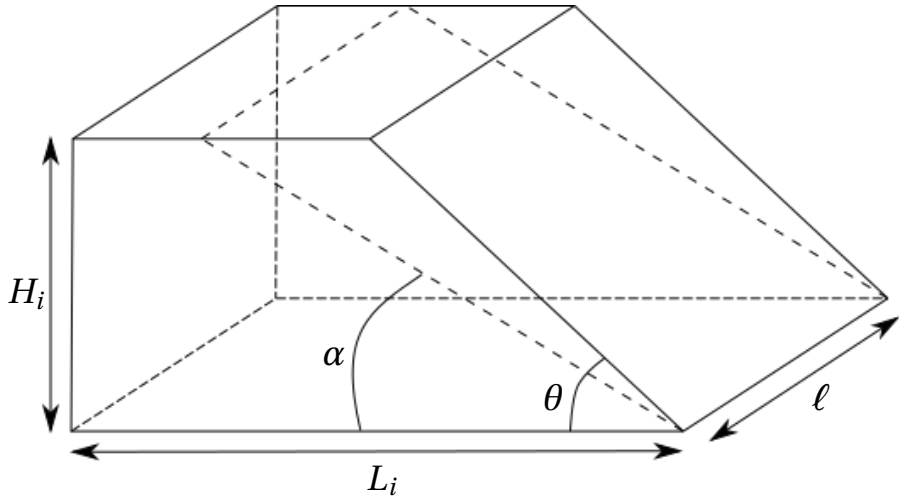

Figure 5.18 – Schematic of the stability of a cohesive granular heap. The top right slice repose on a slip plane S inclined at an angle α.

In order to provide an upper limit of the angle of failure for small columns, we may consider the stability of the column after the failure. Indeed, after the detachment of the top right corner of the column, the remaining heap does not break and is therefore considered as stable (see Fig. 5.18). In this configuration, the remaining heap draws an angle θ with the ground, and we look for the maximum value of θ for the heap to remain stable. Following the same process that led to equation 5.4, we write the balance between the weight, the friction and the cohesion applied by a slice of material on a planar surface at an angle α. To account for the inclined pile foot, the equation 5.4 is modified as follows:

$$\frac{1}{2}\rho g H_i \left(\frac{1}{\tan\alpha} - \frac{1}{\tan\theta}\right)\left(\sin\alpha - \mu\cos\alpha\right) \leq \tau_c. \tag{5.10}$$

This equation may be rewritten as follows (see Appendix) :

$$f(\alpha,\theta) = \frac{\sin(\alpha-\theta_c)\sin(\theta-\alpha)}{2\cos\theta_c \sin\theta} \leq \frac{\ell_c}{H_i} \tag{5.11}$$

where $f(\alpha,\theta)$ is the general function of stability of a cohesive granular heap. For a given value of θ, a granular heap is stable only if the stability criterion of equation 5.11 is checked for all values of α. Fig. 5.19(a) shows 4 examples of the functions $f(\alpha,\theta)$. The y-axis is the cohesion level ℓ_c/H_i and the x-axis is the chosen angle of the heap θ. One may observe that for each value of the heap base angle θ, the function f describes a parabola centered in $(\theta_c+\theta)/2$. For a cohesion level $\ell_c/H_i = 0.1$ (green dashed line), the parabola given by the stability criterion for a heap angle θ_3 (orange curve) intercepts the cohesion level line, thus gives several possible values of failure angle, the heap angle θ_2 (green curve) corresponds to the exact limit of stability, and the heap angle θ_1 (cyan curve) corresponds to a stable heap. For a cohesion level

$\ell_c/H_i = 0.042$ (cyan dashed line), only the heap angle θ_1 may be consider stable as it is at the limit of stability. For instance, if a cohesive column with a cohesion level $\ell_c/H_i = 0.1$ (green dashed line) breaks at an angle θ_3, the granular heap remaining will not be stable either and will have to break again until the remaining heap base angle reaches the value θ_2 or lower.

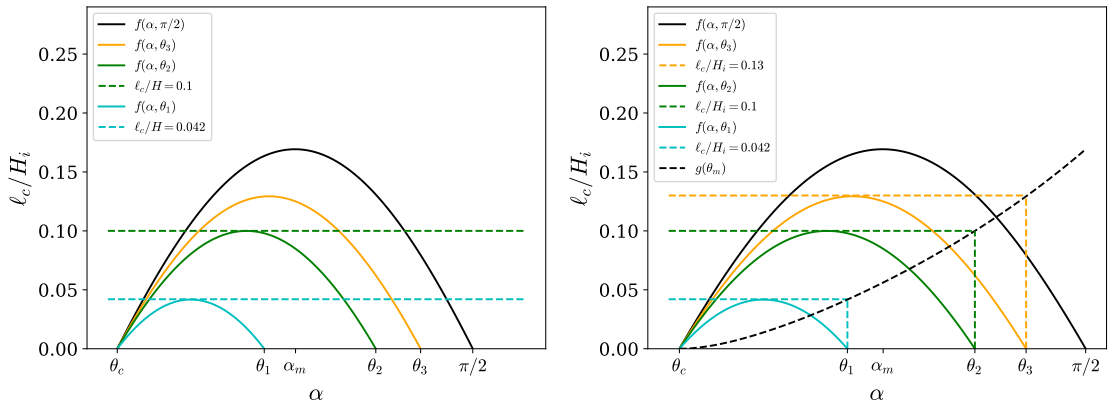

(a) (b)

Figure 5.19 – (a) Representation of the function $f(\alpha,\theta)$ for several values of θ. Each representation reaches a cohesion level at its maximum value. (b) Visual representation of the function $g(\theta_m)$ that describes the maximum angle of stability of a granular heap for a given cohesion level ℓ_c/H_i.

For any value of θ, the curve $f(\alpha,\theta)$ corresponds to the limit of stability of a unique cohesion level ℓ_c/H_i. For a given cohesion, we may rewrite equation 5.11 at the exact limit of stability :

$$f(\alpha,\theta_m) = \frac{\sin(\alpha-\theta_c)\sin(\theta_m-\alpha)}{2\cos\theta_c\sin\theta_m} \leq \frac{\ell_c}{H_i} \tag{5.12}$$

where $f(\alpha,\theta_m)$ is the function reaching the value ℓ_c/H_i for the value $\alpha_{max} = (\theta_c + \theta_m)/2$ (see appendix). Therefore, we may introduce α_{max} in equation 5.12 to obtain the following equation describing the maximum angle of stability of a granular heap for a given cohesion level.:

$$g(\theta_m) = \frac{1-\cos(\theta_m-\theta_c)}{4\cos\theta_c\sin\theta_m} = \frac{\ell_c}{H_i} \tag{5.13}$$

The function $g(\theta_m)$ is plotted in Fig. 5.19(b). We observe that for a given cohesion level ℓ_c/H_i the function g always returns the value θ_m corresponding to the function $f(\alpha,\theta_m)$ describing the limit of stability of a granular heap. Note that for a rectangular column at a cohesion level $\ell_c/H_i = 0.13$ (orange dashed line), the corresponding value of the maximum angle of stability θ_3 is not a failure angle allowed by the function $f(\alpha,\pi/2)$ (black curve). This means that for large values of ℓ_c/H_i, *i.e.* when $g(\theta_m) >$

$f(\alpha, \pi/2)$, we expect to measure a failure angle way lower than θ_m and closer to $\alpha_m = \theta_c/2 + \pi/4$.

Fig. 5.20 shows the final angle of failure α_f measured for every cohesion ℓ_c and initial height H_i. Experiments where columns never collapse are artificially placed at $\pi/2$. We see that most of the values of failure angle measured are displayed below the limit of stability which is consistent with the model. However, some columns seem to break at angles not allowed by the model. While this is unexpected, this happen for very small values of H_i. At these scales, a long delay between the removal of the gate and the failure is observed, which implies that we may have to account for other effects at long times scales (creeping, PDMS lubrication, etc...). It seems that the definition of θ_m as the limit angle of stability of a granular heap suits the definition of α_f as it is the lowest angle measured below which grains have not moved during the collapse. The function $g(\theta_m)$ seems to capture the fact that every collapsed column forms a granular heap with an angle of stability below θ_m for a given cohesion level. Also, one can see that the trend of the experiments are deviating from $g(\theta_m)$ as g get closer to f. This result is consistent with the explanation given above. Also, we only considered the case of a failure happening along a slip plane, while the actual failures may follow more complex shapes.

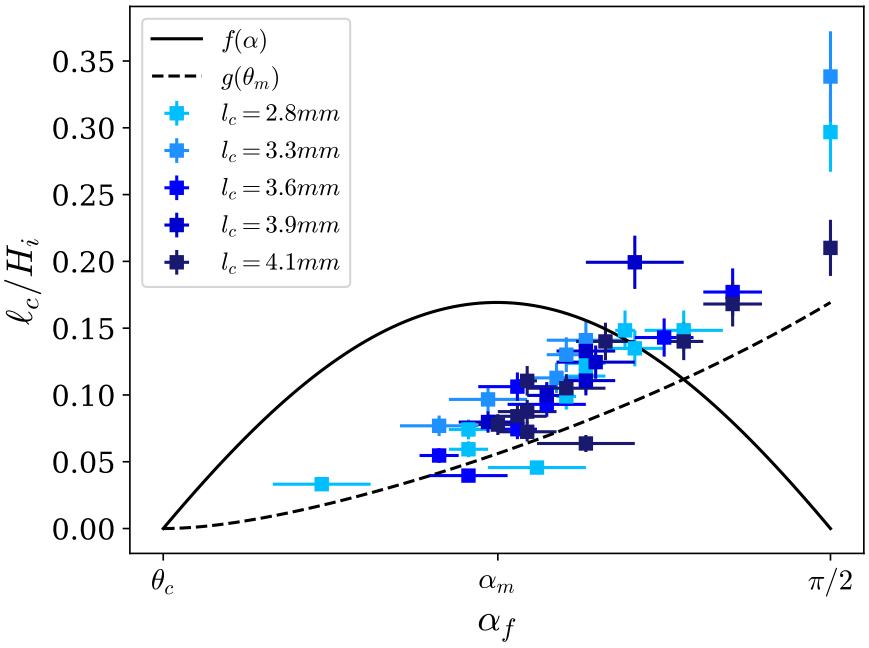

Figure 5.20 – Measurements of (a) the initial angle of failure α_i and (b) the final angle of stability α_f for each cohesion level ℓ_c/H_i considered. The dashed line corresponds to equation 5.13.

5.5 Velocity of the front

Once the gate is removed, the front position $L(t)$ is recorded. After a short acceleration phase, the front position travels at a constant velocity, as already mentioned by Langlois *et al.* [211]. The surface of the collapsing column is detected thanks to a laser sheet recorded by a high speed camera. The line corresponding to the ground bottom is used to detect the position of the pile foot over time (see Fig. 5.21): a spatio-temporal diagram is plotted by recording this line at different times, from which the position of the pile foot over time and the run-out length $L(t) - L_i$ are measured, as shown in Fig. 5.22.

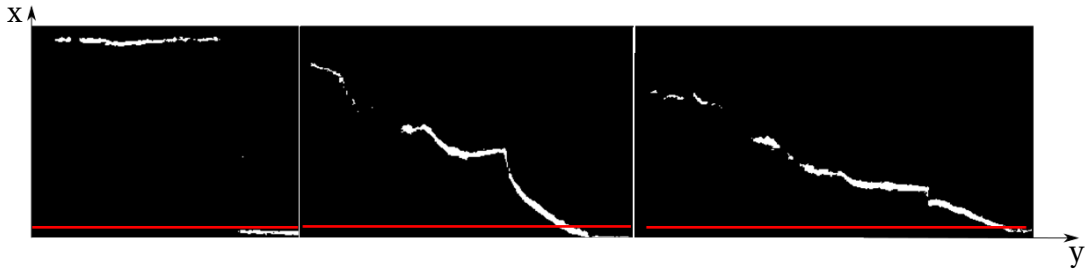

Figure 5.21 – Surface of the collapse obtained from the laser sheet visualisation at 3 time steps : t = 0, t = 0.18 s and t = 0.52 s.

We see a clear inflexion point for each curves. The velocity is measured from these curves using a linear fit on the curves around the inflexion point. At the end of the flow, the front decelerates and eventually reaches a static position. Fig. 5.23(a) shows the front position $L(t) - L_i$ as a function of time t for $\ell_c = 0$ (cohesionless material), $\ell_c = 2.8$ mm and $\ell_c = 3.6$ mm, both for experimental and numerical results. The main plots were recorded for an aspect ratio $a = 1$, and the inset shows the effect of a low aspect ratio $a = 0.5$. The start time t_0 is arbitrary and was chosen to help the comparison between the curves. The comparison between experimental and numerical results shows a good agreement from the beginning to the end of the steady state. In particular, the cohesionless granular experiment (light blue curves) shows that the main features of the granular collapse are well captured by the continuous numerical code and the $\mu(I)$ rheology. But there is a noticeable difference when the flow slows down before stopping for the cohesive tests. The final run-out length is observed to be shorter in the numerical simulations for cohesive materials compared to the experiments.

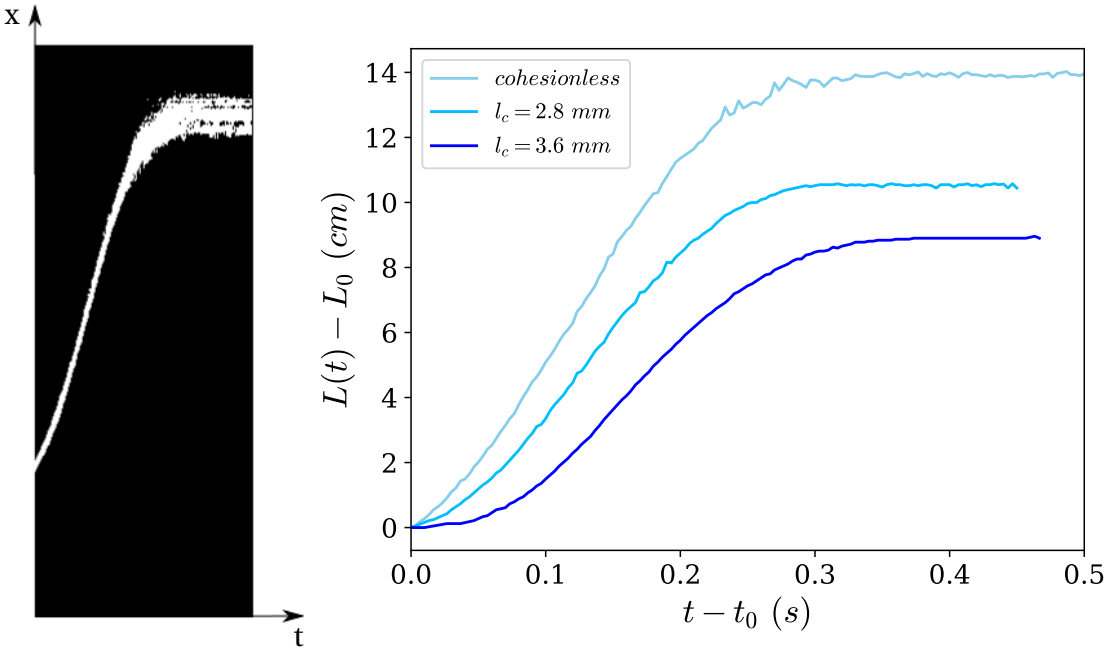

(a) (b)

Figure 5.22 – (a) Spatio-temporal diagram of the pile foot position over time. Vertical axis is the position and the horizontal axis is the time. (b) Plot of the run-out distance versus time corresponding to the spatio-temporal diagram for $a = 1$.

For low aspect ratio experiments (inset) and for a large cohesion level, the start of the flow is strongly delayed. A bulk creeping reorganization may be invoked to explain this phenomenon which is not present in the simulations. The effect of cohesion seems to be stronger for low aspect ratios [212].

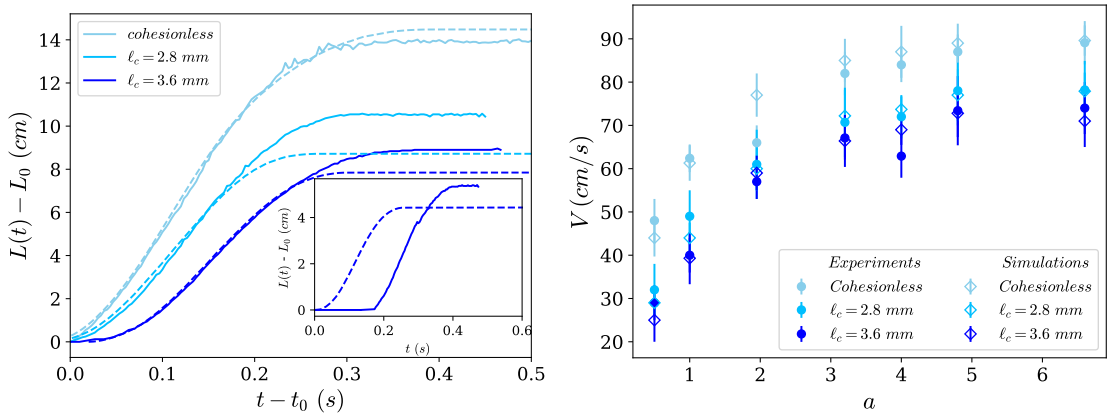

(a) (b)

Figure 5.23 – (a) Position of the front for different cohesions in experiments (continuous curves) and simulations (dashed curves) for an aspect ratio $a = 1$. Inset: results for $a = 0.5$. For the most cohesive material (dark blue, $\ell_c = 3.6$ mm), a significant delay is observed before the collapse starts. (b) Velocity of the front as a function of the aspect ratio for different cohesions. The color code is the same as in (a).

Fig. 5.23(b) shows the effect of the aspect ratio on the velocity measured during the steady flow phase. The flow velocity increases with the aspect ratio before saturating for $a \geqslant 3$. The comparison between experimental and numerical results gives a good agreement, an increase of the cohesion level decreases the front velocity. However, the simulations under estimate the run-out distance.

5.6 Run-out length and final deposit morphology

Once the kinetic energy of the collapse is fully dissipated, we measure the final deposit and focus on the final run-out length $L_f = L_i + \Delta L$. As presented in section 5.1, the run-out length and the final height of a cohesionless granular material scales as a power law of the aspect ratio a:

$$\frac{\Delta L}{L_i} \propto \begin{cases} a & \text{for } a \leq 3 \\ a^{2/3} & \text{for } a \geq 3 \end{cases} \quad \text{and} \quad \frac{H_f}{L_i} \propto \begin{cases} a & \text{for } a \leq 0.7 \\ a^{1/3} & \text{for } a \geq 0.7 \end{cases} \tag{5.14}$$

From our experiment, the results for L_f and H_f obtained with cohesionless and cohesive materials are plotted on Fig. 5.24(a)-(b). This plot shows a decrease of the run-out length when increasing the cohesion. However, the power laws (5.14) seems to remain unchanged, as seen by the a^1 and $a^{2/3}$ slopes on the graph. The cohesion only changes the pre-factor on the run-out length, without changing the exponent of the aspect ratio.

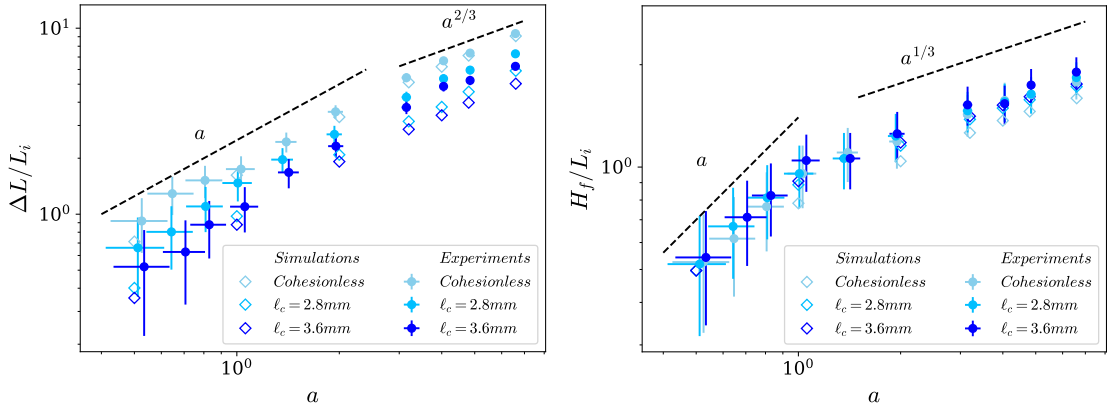

(a) (b)

Figure 5.24 – (a) Normalized run-out length as a function of the aspect ratio for cohesionless and cohesive beads for both experiments and simulations. (b) Normalised height of final deposit as a function of the aspect ratio a.

As presented in section 5.5, the final run-out predicted by the simulations are not in good agreement with the experiments for the cohesive materials. In order to investigate the reasons of this discrepancy, we look at the morphology of the free surface at the end of the flow. Fig. 5.25 shows the superposition of the numerical and experimental profile for a column of aspect ratio $a = 1$ and cohesion $\ell_c = 2.8$ mm. The global morphology of the free surface seems to be well captured by the numerical model excepted at the contact point between the bottom surface and the material. Also at the end of the collapse (t = 0.45 s), the shape of the front of the granular material is different between the experiments and the simulations. This discrepancy may be linked to the no-slip boundary condition applied at the contact point in the simulations. In the following, we will investigate the effect of several rheological parameters of the numerical model on the velocity and the run-out distance.

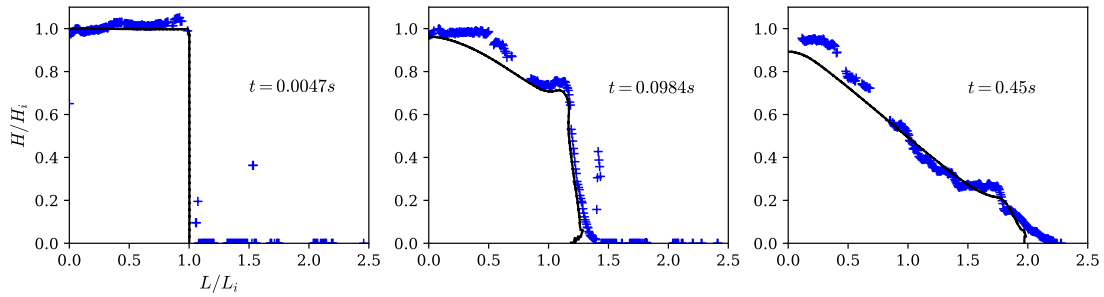

Figure 5.25 – Snapshots of the numerical and experimental profiles at different times for $H_i = 8.9$ cm, $a = 1$, and $\ell_c = 2.8$ mm.

5.7 Effect of the rheological parameters

The rheological model is set by three arbitrary parameter that are tricky to determine experimentally : μ_s, $\Delta\mu$ and I_0 (see equation 4.12). In the model we assume that the cohesion does not impact these parameters, however, since the run-out length and the final morphology is not well captured by the model, a deeper investigation is needed. An investigation on the effect of the rheological parameter $\Delta\mu$ is presented Fig. 5.26(a). The distance of the front $L(t)$ is plotted as a function of time for a column of cohesion $\ell_c = 2.8$ mm and an aspect ratio $a = 1$. The green area is obtained by changing the value of $\Delta\mu$ from 0 to 0.2. Fig. 5.26(b) shows the associated final profile for a variation of $\Delta\mu$. We see that an increase of the parameter $\Delta\mu$ leads to a decrease of the run-out length. As it seems, changing the value of $\Delta\mu$ allows to adjust the final run-out of the cohesive collapse with a small change on the velocity of the collapse.

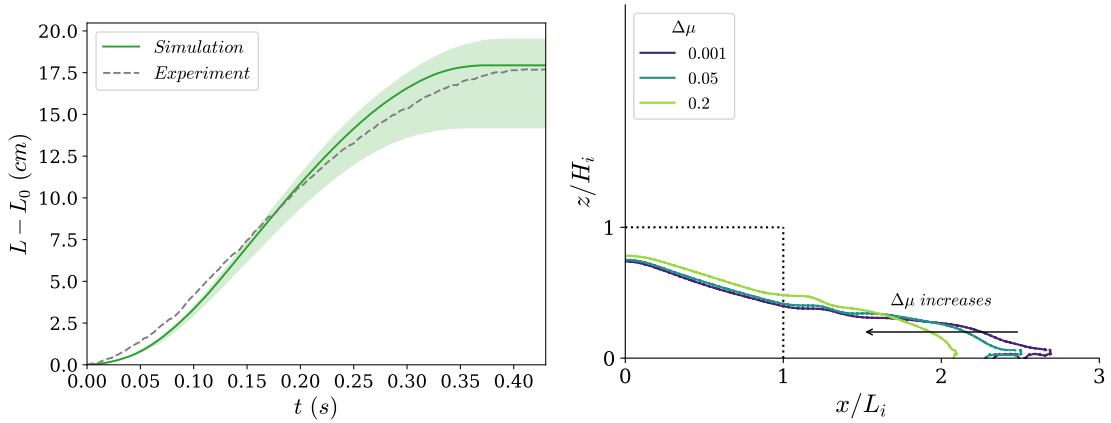

(a) (b)

Figure 5.26 – (a) Experimental and numerical front position $L(t)$ of the collapse for $\ell_c = 2.8$ mm, $I_0 = 0.1$ and $a = 1$. The green area is obtained by varying the parameter $\Delta\mu$ from 0 to 0.2, and the green line is the best agreement for the velocity and the run-out. (b) Associated final profile for 3 values of $\Delta\mu$.

The effect of a variation of I_0 is plotted in Fig. 5.27(a) and the associated run-out profile is plotted in Fig. 5.27(b) for the same experiment than before, and a chosen $\Delta\mu = 0.1$. We see that changing the value of I_0 barely changes the dynamics and the final profile of the run-out, therefore if the cohesion has an impact on this parameter, we do not expect to see a major effect.

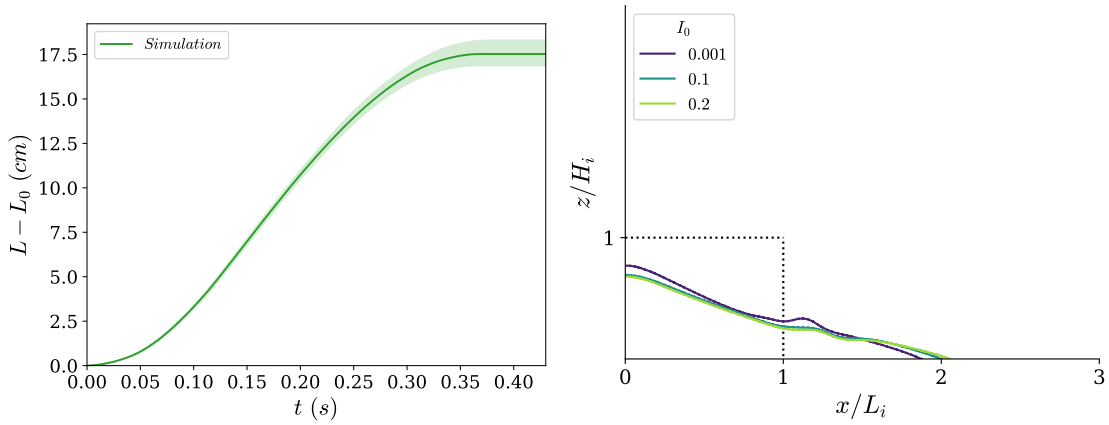

(a) (b)

Figure 5.27 – (a) Numerical front position $L(t)$ of the collapse for $\ell_c = 2.8$ mm, $\Delta\mu = 0.1$ and $a = 1$. The green area is obtain by varying the parameter I_0 from 0.001 to 0.2, and the green line is the best agreement for the velocity and the run-out. (b) Associated final profile for 3 values of I_0.

The last parameter we investigate is μ_s. While this parameter has been measured experimentally using inclined plane experiments in chapter 2, the measure was obtained by the triggering of the flow on the plane. However after the initiation of the flow, one may suggest that the PDMS coating could act like a lubricant which could decrease the effective μ_s during the flow. An investigation on the effect of the rheological parameter μ_s is presented in Fig. 5.28. The distance of the front is plotted as a function of the time for an experiment of aspect ratio $a = 1$ and 2 simulations with μ_s equal to 0.4 and 0.25. We see that a decrease of μ_s is linked to an increase of the velocity and of the run-out.

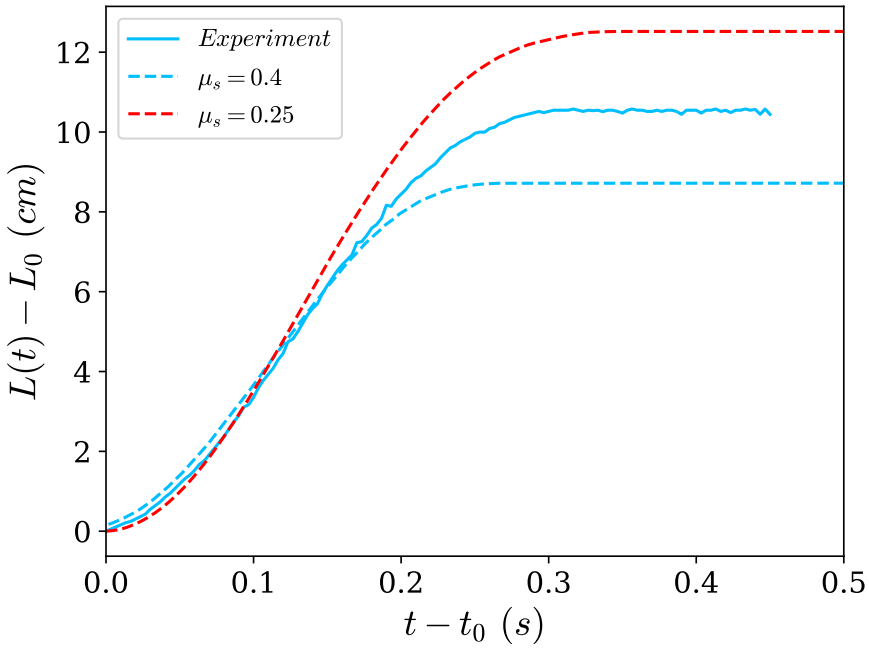

Figure 5.28 – Experimental and numerical front position $L(t)$ of the collapse for ℓ_c = 2.8 mm, $\Delta\mu = 0.12$, $I_0 = 0.3$ and $a = 1$.

With this investigation on these 3 parameters, we see that a variation of $\Delta\mu$ and μ_s may have a significant impact on the dynamics of the collapse and there might be possible to define an optimal doublet $(\mu_s, \Delta\mu)$ to fit the experiments. Since in the experiments the PDMS coating might change the frictional properties during the flow, we do not know if the apparent effect on μ_s and $\Delta\mu$ is due to cohesion or not. These results suggest that a deeper investigation on the rheology of the CCGM is needed to fully understand its dynamical behavior

5.8 Conclusion and discussion

The collapse of a granular column is a widely used benchmark configuration for experiments and numerical simulations. In this chapter we performed both experiments using the model CCGM, and numerical simulations using a continuous approach based on a cohesive $\mu(I)$ rheology. For a cohesionless granular material, we observe a good agreement between experimental and numerical results despite the assumptions needed to carry out the calculation. Indeed, the simulations are two-dimensional and based on continuous equations whereas in the experiments, a microscopic scale (the size of the grains) exists.

In the experiments, the first effect of the cohesion is to stabilize a granular column below a given height and to modify its maximum angle of stability. The domain of existence of the collapse and the angle of failure have been measured and compared

with a simple theoretical approach proposed by Restagno *et al.* [204]. The condition of stability calculated by Restagno *et al.* [204] predicts the maximum angle of stability of the column for low aspect ratios.

During the flow, the cohesion enhances the dissipation of energy. This leads to lower collapse velocities and to shorter run-out lengths. A striking effect of cohesion on the collapse of the granular column is the 'surfing wedge' on the top corner of the column. It acts as a dead volume simply transported by the granular flow below it.

The comparison of results (run-out length, collapse velocity) between the experiments and the numerical simulation for cohesive material are in good agreement, despite some discrepancies at the end of the flow. The delay between the gate removal and the initiation of the collapse observed in the experiments has not been investigated in detail. Since this delay is not observed in the simulations, some microscopic evolution at the scale of the contacts between particles may be invoked. An investigation on the effect of the different rheological parameters has also been performed and suggests that the usual rheology used for cohesionless granular materials may be altered by the presence of cohesion and a PDMS coating.

The granular collapse experiment provides valuable informations on the frictional properties of the CCGM. As expected, a yield stress τ_c added to the $\mu(I)$ rheology seems relevant to describe the behavior of cohesive granular media. However, there are still some progress to make. On the numerical side, the transition from a static column to a flow is tricky. On the experimental side, supplementary experiments are needed to deepen the knowledge about the rheological properties of the cohesive granular materials.

6 Perspectives

This PhD thesis brings some elements in the comprehension of the flowability of cohesive granular materials, however several questions remains open. In this section we present a summary of the different results and the perspectives for each subject, before presenting preliminary results on the rheology of the CCMG carried out thanks to an imposed pressure rheometer.

6.1 Perspectives on the studied configurations

6.1.1 Characterization of the cohesion-controlled granular material

The cohesion-controlled granular material is made of spherical glass beads coated with a polyborosiloxane polymer. The characterization of the inter-particle cohesion and the bulk cohesion as a function of the coating thickness has been performed. The characterization of the inter-particle tangential force has not been investigated yet as we initially focus on the characterization of cohesion. It certainly plays a role in the rheology of the CCGM, as suggested by the preliminary results in section 6.2. Another interesting question concerns the role of the stiffness and inelasticity of the particles. In the numerical simulations performed by Sandip Mandal [128], the restitution coefficient and the stiffness of the granular material is an important parameter influencing the bulk cohesion. However our attempt to test this and change the properties of the CCGM through several methods failed. Among the attempts, we tried to change the boric acid mass ratio in the preparation with the idea that it would change the stiffness of the polymer coating. Fig. 6.1 shows the variation of the inter-particle cohesive force as a function of the percentage of boric acid poured in the preparation. The inter-particle cohesive force do not seem to change significantly between 5% and 30 %. In the same spirit we tried to change the temperature (from -4°C until 180 °C). A change of the repose angle of a pile is observed but with a weak reproducibility of the experiments.

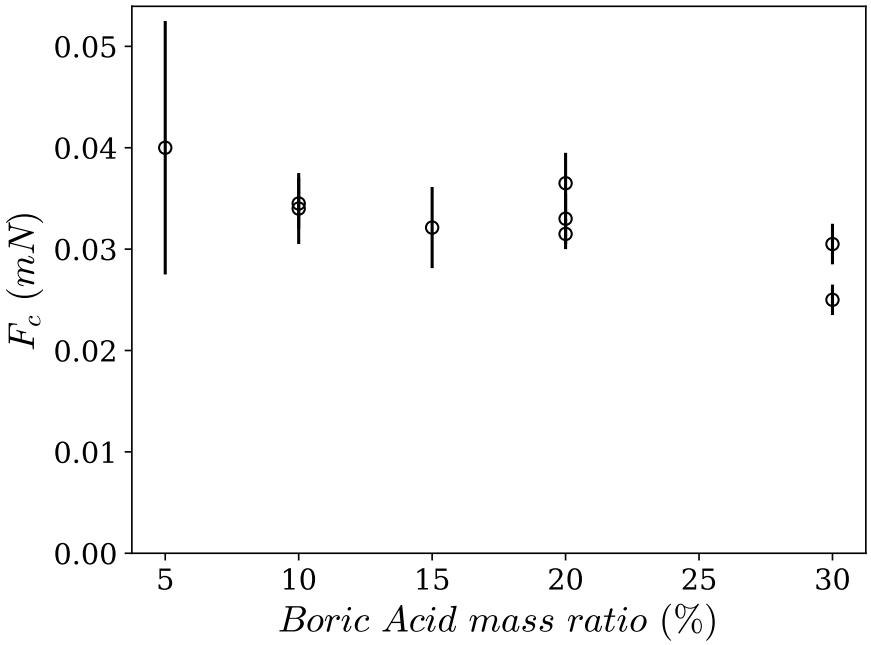

Figure 6.1 – Inter-particle cohesion force for 800 µm particles as a function of the amout of boric acid poured in the preparation. (mass ratio of boric acid to mass ratio of PDMS)

Despite these issues, the PBS coating of particles opens several experimental perspectives. This method of cohesion control may be extended to other shapes of particles (polydisperse beads or sand grains) to model more realistic powders provided that silicium is present at the surface of the grains to ensure the sticking of the PBS.

6.1.2 Erosion of cohesive granular material

The Jet Erosion Test performed on the CCGM has shown that this method allows to probe the inter-particle cohesion force with a simple setup. The introduction of the cohesion force in the definition of the Shields number seems to predict the erosion threshold of the CCGM. On the erosion threshold, the modification added in the Shield number to account for the cohesion comes with a fit parameter of order 1. This parameter accounts for the local distribution of the contacts of the grains, and a more accurate description of the local geometry would provide a better understanding of the transport threshold and describe whether a single particle or a cluster is eroded. Also, investigating the crater shape and the dynamics of the erosion in the crater at the impact point of the jet would be interesting. In the first observation, for cohesionless grains, avalanches are triggered periodically at the border of the crater depending on the velocity of the jet. For cohesive granular materials, the avalanches do not seem to be present and an investigation on the effect of cohesion on the stability of the crater

borders would be interesting.

6.1.3 Discharge of a silo

The study of both the cylindrical and quasi-2D silos discharge of cohesive granular material has provided several results. The flow threshold as a function of the cohesion and of the size of the outlet has been studied and is controlled by the cohesive length ℓ_c. For both silos the introduction of ℓ_c as an effective grain size in the expression of the parameter ϕ_0 allows to capture the main effect of cohesion on the discharge for standard outlet shapes. In the future the ϕ_0 parameter which represents the volume fraction of the material at the outlet may be studied in more detail to understand its dependency on the dilation and on the velocity. For now, the description of the flow rate is not directly linked to the rheology, and a better description of the velocity field and the dilatancy field above the outlet may help to understand the effect of both friction and cohesion on the discharge.

Another perspective concerns the study of the flow threshold in the simulations. The simulations are based on the 2D Navier-Stokes solver of the Basilisk open-source library (www.basilisk.fr). The plastic criterion is not strictly captured and a regularization method is used in which a cut-off of the viscosity to a finite but high value is introduced for low values of I. Therefore, it is not possible to observe a static behavior since even a highly viscous fluid would flow, but we expect to observe a strict change of behavior for low values of ℓ_c/D, as in the experiments. We performed several simu-

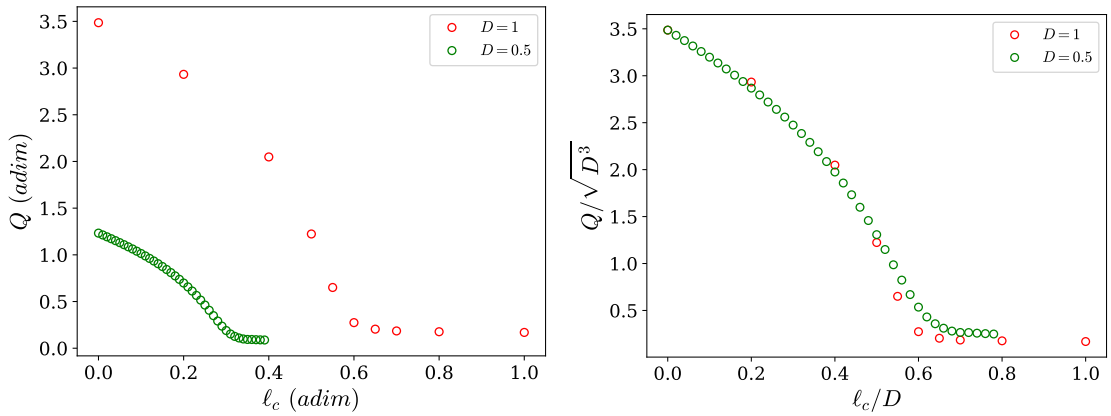

(a) (b)

Figure 6.2 – (a) Flow rate Q as a function of the cohesive length ℓ_c for two outlet sizes D. (b) Rescaled Flow rate Q as a function of ℓ_c/D for two outlet sizes.

lation for different cohesive length ℓ_c and outlet sizes D to measure the flow rate as a function of ℓ_c/D. Fig. 6.2(a) shows the flow rate Q as a function of the cohesive length ℓ_c for two outlet sizes D. For both outlets, we observe a change of trend in the flow rate at a given value of ℓ_c. Fig. 6.2(b) shows the rescaled flow rate as a function of ℓ_c/D.

Interestingly, both thresholds rescale together as in the experiments. However the critical value of ℓ_c/D in the experiments is 0.5 while it is closer to 0.6 in the simulations. Since this result was obtained from only one sample of grain for the 2D silo, more experiments are needed to check the reliability of the numerical threshold.

A last pespective concerns the effect of the cohesion on the Janssen effect for a static silo. We performed preliminary experiments to measure the Janssen effect for the CCGM. The experimental setup is presented in Fig. 6.3. A PMMA vertical cylindrical silo of 2 cm radius R is closed by a cylinder. The cylinder is designed to penetrate the silo with a 200 micron gap with the walls (see Fig. 6.3(b)). 800 µm grains are poured in the silo via a funnel above (see Fig. 6.3(a)) and are blocked by the bottom cylinder. A laboratory jack (see Fig. 6.3(a)) allows to move down the cylinder after the filling of the silo in order to mobilize the friction on the walls. The effective mass at rest on the cylinder is measured by a weighting scale. The experiments are performed on cohesionless grains and grains of coating thickness b between 100 nm and 155 nm.

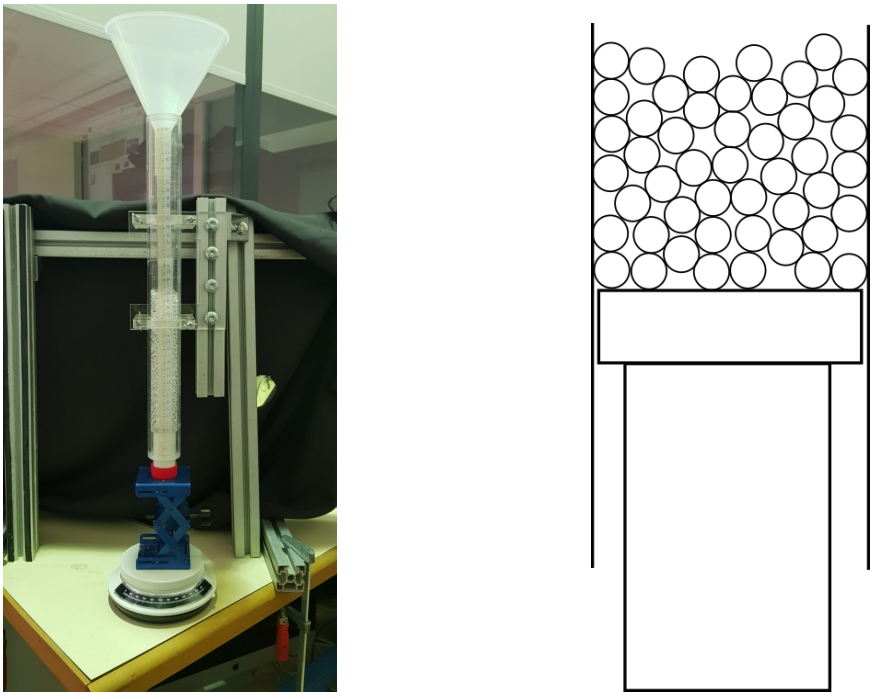

(a) (b)

Figure 6.3 – (a) Photo and (b)schematic of the experimental setup used to study the Janssen effect. The cylinder prevents the grains to fall without touching the walls of the silo.

The theoretical apparent mass m_{app} measured on the bottom cylinder is related to the height of grains as follows:

$$m_{app} = \lambda\phi\rho S(1 - e^{-\frac{H}{\lambda}}) \tag{6.1}$$

where S is the section of the silo, ϕ is the volume fraction, ρ is the density of the grains, H is the height of grains and λ is a characteristic screening length that represents the typical position of the archs supporting the weight of grains. As presented in section 4.1.1, λ, for cohesionless grains, equals to $R/2K\mu_w$ where R is the radius of the silo, μ_w is the grain-wall friction coefficient and K is the ratio between the radial stress σ_{rr} and the vertical stress σ_{zz}. The first observation is that it is harder to mobilize the friction on the walls for cohesive grains than for cohesionless grains. Whereas moving down the cylinder of 1 grain diameter is sufficient to mobilize the friction for cohesionless grains, approximately 10 grain diameter is needed to mobilize the friction of cohesive grains. This result strengthens the results of section 4.5 where we assume that the friction of the cohesive grains on the walls do not decelerate the grains. Fig. 6.4 shows the measurements of the apparent mass on the cylinder for 3 sample of grains. The value of λ is fitted according to equation 6.1 and the dashed lines correspond to the prediction. Assuming that the friction has been equally mobilized for the 3 experiments, we observe that the value of λ decreases when the cohesion increases. It is not clear if this effect is due to the bulk cohesion or to a lubrication at the walls. Further experiments are needed to study the effect of cohesion or lubrication on the Janssen effect.

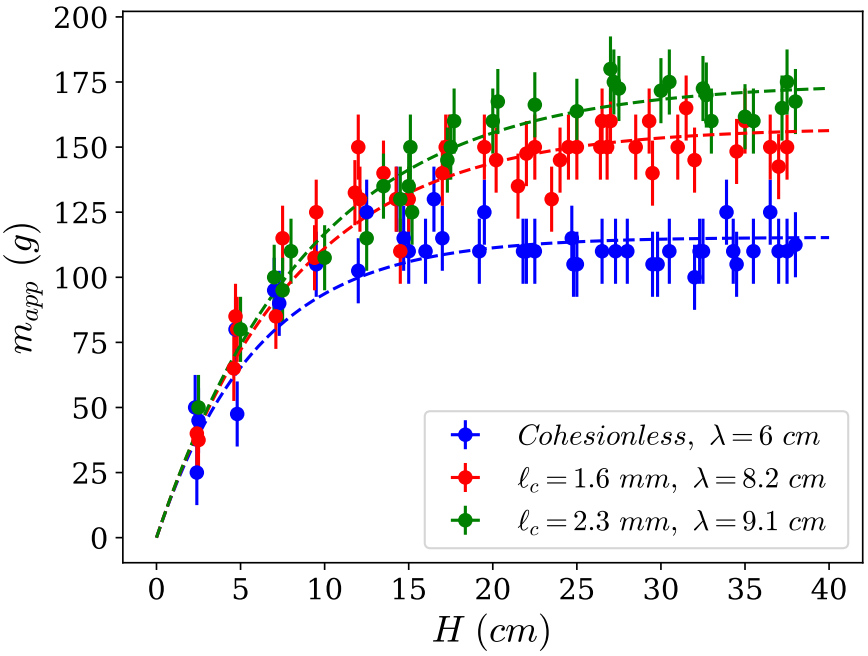

Figure 6.4 – Measurements of the apparent mass at the bottom of the cylinder for cohesionless and cohesive grains of thickness b equal to 100 nm and 155 nm. λ is fitted according to equation 6.1.

6.1.4 The granular collapse experiment

We have studied the flow threshold and the shape of the initial flow in terms of slip angle for a cohesive granular column. The velocity and the shape of the final deposit have also been studied both experimentally and numerically as a function of the cohesion. We observe that the cohesion tends to stabilize the granular columns and to select an initial slip plane at the initiation of the collapse. During the spread, the cohesion slows down the flow and reduces the distance of the spread. The dynamics of the spread is well captured by the simulations with a continuous description although some discrepancies are seen concerning the final run-out distance. These discrepancies could be due to a modification of the rheological parameters due to the PDMS or to the no-slip boundary condition in the simulations. To go further, a deeper investigation on the rheology of the CCGM is needed.

6.2 Rheology of the CCGM

This section presents the preliminary results from an investigation, in collaboration with Franco Tapia, on the rheology of the CCGM performed with a home designed pressure imposed rheometer. The apparatus has already been used to study the effect of the roughness on the rheology of immersed and dry spheres, and the rheology of suspensions of fibers [213, 214].

6.2.1 Experimental methods

The experimental apparatus, depicted in Fig. 6.5, is a custom-made rheometer enabling pressure-imposed rheological measurements of granular materials and suspensions. The granular sample is sheared in a plane-plane geometry consisting of a cylindrical annulus (of internal and external radii R1 = 43.95 mm and R2 = 90.28 mm, respectively) covered by a fixed top plate. The bottom annulus reservoir rotates at a constant angular velocity controlled by an asynchronous motor (Parvalux SD18) regulated by a frequency controller (OMRON MX2 0.4 kW) while the top plate does not rotate.

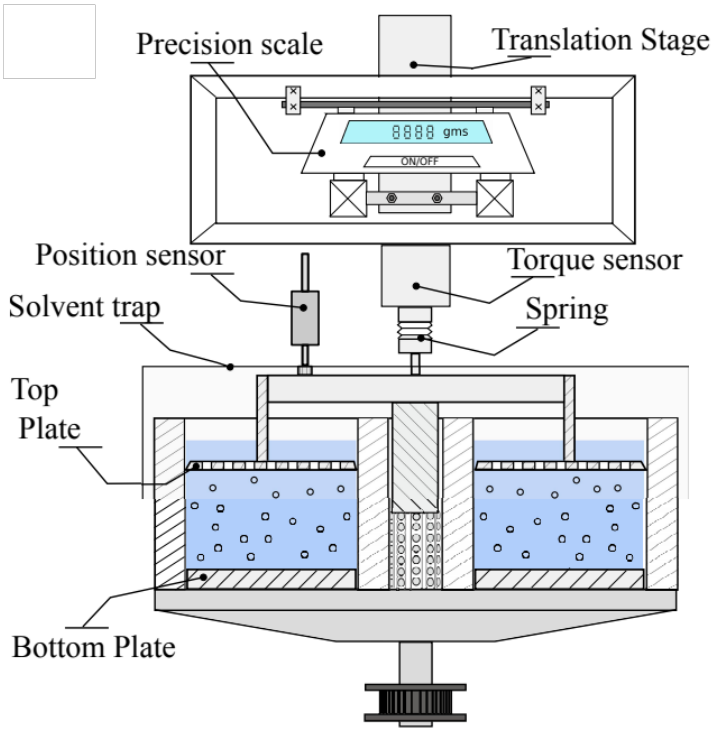

Figure 6.5 – Sketch of the experimental apparatus, extracted from Tapia *et al.* [213]

A wide range of shear rate $\dot{\gamma}$ can be achieved, spanning between 0.02 and 130 s^{-1}. To ensure an efficient no-slip boundary condition, the top and bottom plates are made rough by covering them with a sieve mesh 1.5 times the size of the grains. The top plate can be moved vertically by using a linear positioning stage (Physics Instrumente M-521) and fits into the bottom annulus with a precision of 280 µm. This apparatus was initially built to study suspension rheology and has been adapted for the investigation of dry granular material. The shear stress τ is computed from the torque exerted on the top plate measured by a torque transducer (TEI - CFF401). The normal stress perpendicular to the top plate, simply referred as the particle pressure P, is given by a precision scale (Mettler-Toledo XS6002S) attached to the translation stage. The bulk packing fraction of the sample, ϕ, can be adjusted by displacing the top plate. The plate position h is continuously measured by a position sensor (Novotechnik T-50). A feedback control system connects the positioning stage and the precision scale in order to perform pressure-imposed experiments on the sample. In this pressure-imposed mode, the resulting shear stress τ and packing fraction ϕ are measured as functions of the shear rate $\dot{\gamma}$ for a given particle pressure P once the steady state is established. Note that a soft spring is placed between the top plate and the torque sensor to avoid blockage during experiments with dense packings. Since the velocity profile is assumed to be linear, the shear rate $\dot{\gamma}$ is just the ratio between the bottom plate velocity V and the top plate position h, and the friction coefficient μ is given by the ratio between the measured tangential stress τ and the imposed pressure P.

The cohesive samples is made of 400 g of 800 µm spherical glass particles coated with a PBS layer of thickness b varied from 10 to 100 nm which corresponds to cohesive stresses τ_c of 3 to 75 Pa. The imposed pressure varies from 1100 to 1500 Pa. This high pressure level has been chosen to neglect the hydrostatic pressure due to gravity but is also high compared to the cohesive stress, which may hide the influence of cohesion.

6.2.2 Preliminary results on the rheology

We first investigate the effect of a very thin coating thickness. Fig. 6.6(a) and (b) show the evolution of the friction μ and the volume fraction ϕ as a function of the inertial number I for three values of the imposed pressure. One may notice a slight increase of $\mu(I)$ when decreasing I for low values of I for both experiments. This result has already been experimentally highlighted by Kuwano *et al.* [127]. The most interesting effect is seen on the values of ϕ. Whereas there is no difference on the friction when a 10 nm coating is added, there is a significant increase of volume fraction. This effect has been predicted by Trulsson *et al.* [215] in numerical simulations based on contact dynamics. They observed that a small change of inter-particle friction does not affect significantly the $\mu(I)$ rheology but changes significantly the volume fraction. The authors explain this effect by a transition from a rolling to a sliding mechanism between the grains. This is the first sign that the coating may strongly affect the frictional interactions between the particles.

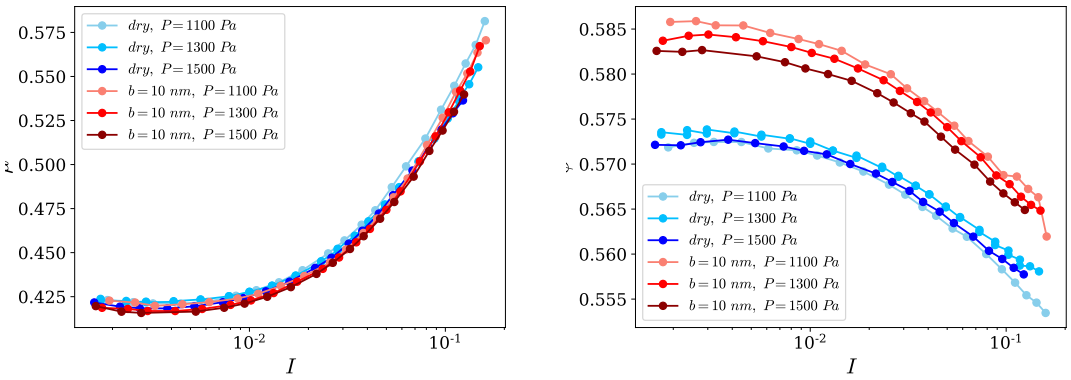

Figure 6.6 – (a) friction coefficient μ and (b) volume fraction ϕ as a function of the dimensionless number I for three pressure levels.

Fig. 6.7 shows the evolution of the friction coefficient μ for coating thickness b from 20 nm to 100 nm and $P = 1500$ Pa. For $b = 20$ nm, we observe that the evolution of μ is similar to the cohesionless material and starts to deviate at $I > 0.1$. For $b = 35$ nm, the level of friction decreases and an increase of V tends to make the global trend of the curves deviate for lower values of I. Also for $b = 100$ nm a sudden increase of μ at very

low values of I is observed. Experimentally this increase is observed for "stick-slip" like behavior where the top plate starts to oscillate fewly at low velocity.

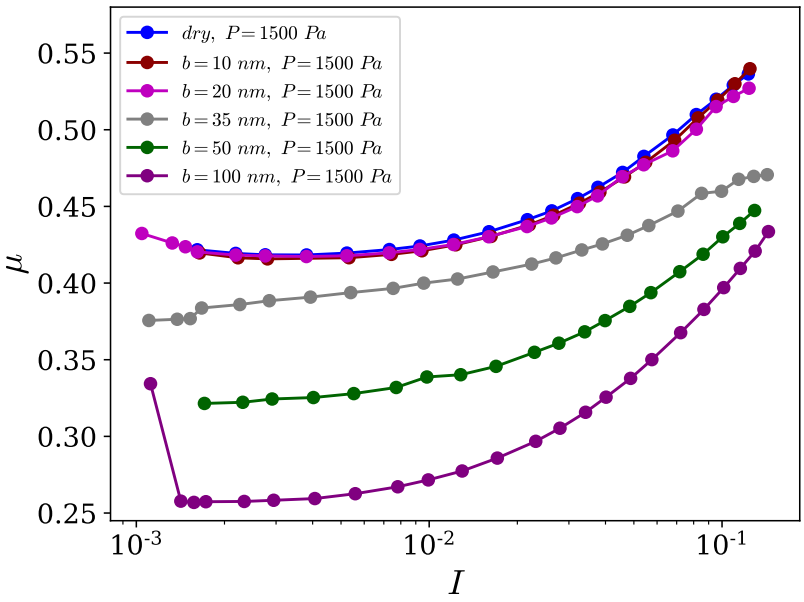

Figure 6.7 – Friction coefficient μ as a function of the dimensionless number I for three coating thickness and three pressure levels.

We next investigate the role of the pressure. Fig. 6.8 shows the results for coating values b of 50 and 100 nm for P varying from 1100 Pa to 1500 Pa. Increasing the pressure leads to an increase of friction which is more pronounced at low shear rate than at high shear rate where the curves for different coatings seem to collapse. However more experiments are needed to better characterize this regime.

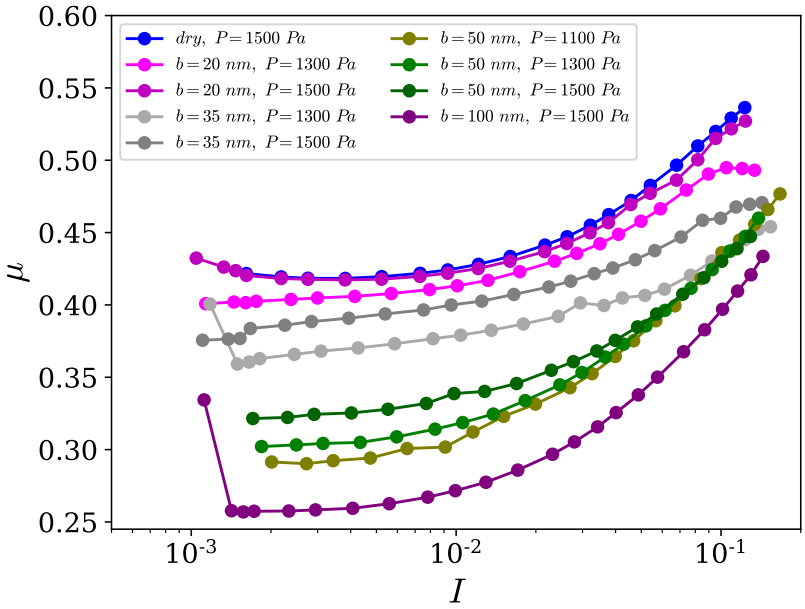

Figure 6.8 – Friction coefficient μ as a function of the dimensionless number I for several coating thickness and pressure levels.

The apparent paradox of these results is the relatively low friction measured, compared to the friction measured in the experiments performed on inclined planes or granular column close to 0.4 as for the non coated material. This paradox may be solved by the existence of lubrication at the contacts between particles in the dynamical regime. Indeed, the rheometer measurements are performed on flowing grains. It seems that for low velocities and high pressures, the behaviour of the grains tends toward a frictional rheology while for high velocities and low pressures, the behaviour of the grains tends toward a lubricated rheology and low friction. It seems reasonable to assume that experiments measuring flow initiation (collapse, inclined plane) measure static thresholds driven by $\mu_s = 0.4$, corresponding to zero velocity and non-zero pressure.

This behavior is reminiscent of the lubrication effect observed in tribology [216, 217, 218]. Several configurations are used to study the effective friction with a fluid lubricant. Generally, an object is placed on a liquid film of viscosity η on a rigid substrate. A load P is applied on the object while it is moved at constant velocity V. The Hersey number $He = \eta V / P$ describes the transition from a frictional interaction to lubrication. Fig. 6.9 shows the general evolution of the friction coefficient as a function of the Hersey number. For low values of He the friction is completely due to solid frictional interactions between the object and the substrate. Then for a given value of He, the value of μ decreases rapidly before it reaches a hydrodynamic trend where every contact point is perfectly lubricated.

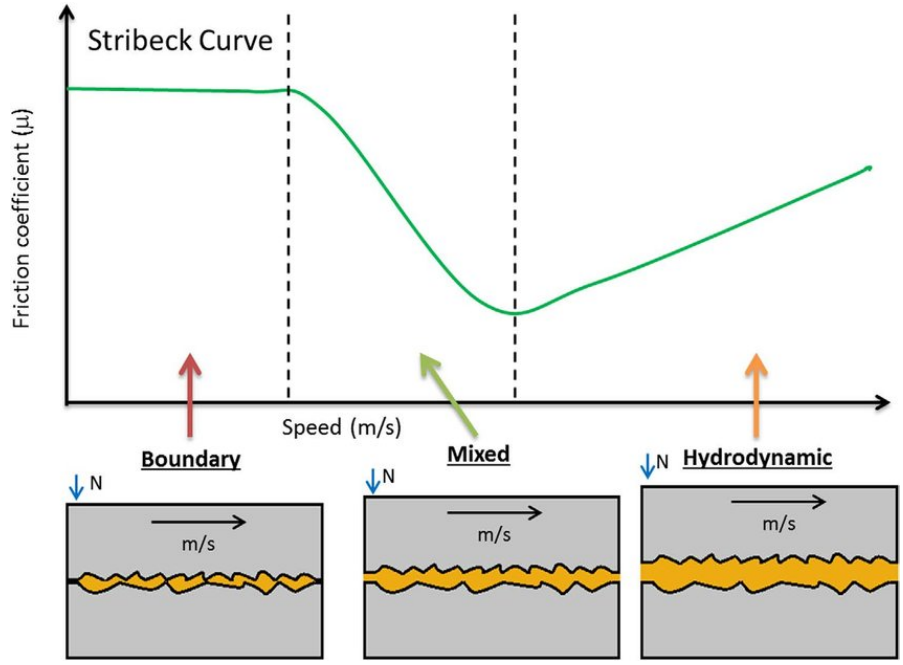

Figure 6.9 – Evolution of the effective coefficient of friction as a function of the Hersey number $\eta V/P$. Extracted from Robinson *et al.* [219]

This description is coherent with the data obtained with the rheometer where the ratio V/P seems to lead the transition to lubrication. One could suggest that the addition of lubrication transition at the particle-particle scale may decrease the macroscopic friction. This is also consistent with other studies on polymer slip effect [220, 221]. For instance, Henot *et al.* [222] showed that the tangential stress needed to deform a PDMS elastomer adsorbed to a surface may be of 1 kPa order of magnitude and is linear with the velocity of deformation.

A deeper investigation on the rheology of the CCGM will be necessary to understand it behavior and a detailed study of the behavior of the coating under tangential deformation is also needed. Ultimately it would be interesting to implement this lubrication effect in continuous modelling. This effect could be one of the reasons of the run-out difference observed between experiments and simulations for the granular collapse. Also this new method might open new possibilities to investigate lubricated granular materials and their applications.

Conclusion

As a part of the ANR Coprint project, the work of this thesis focuses on the characterisation and the description of the properties of a new cohesion-controlled granular material that could be used to model actual powders. Inspired by the kinetic sand, our team developed a cohesive granular material made of silica particles coated with a cross-linked PDMS polymer strongly attached to the particles due to a Si-OH chemical bond. The control parameter of the cohesion is the mass of PDMS mixed with the granular media, which gives an average coating size b around the particles. The first observations on this cohesive granular media suggested that the cohesion of this material could be tuned by changing the average coating size. An inclined plane was used to characterize the bulk cohesion and lead to the assumption that the cohesive media could be modelled by a $\mu(I)$ rheology enhanced with a cohesive yield stress τ_c. Starting from theses preliminary results, the purpose of this work was to rely on previous studies on granular materials and powders in order to develop several tools that could be used to characterize the CCGM and powders in general. Another important part of the thesis was to collaborate with the different participant of the Coprint ANR to work on a cohesive granular rheology that could be implemented in numerical codes, and to develop tools to handle industrial powders. All of this work is a step toward the understanding of the "flowability" of powders and several experiments were carried with the purpose of highlighting some parameters that could describe under which conditions cohesive granular materials could flow.

As presented in chapter 2, the first part of this work is the characterization the cohesive properties of the model granular material. At the bulk scale, we used the angle of repose to characterize the variability of the material to the environmental conditions like moisture, and temperature. The experiments showed a very stable behavior of the material for a wide range of environmental conditions, and a durability of 6 month of use. We also measured the volume fraction of the bulk as a function of the cohesion and we used an inclined plane to characterize the bulk cohesion. This experiment led to the introduction of the cohesive length ℓ_c which is the characteristic length below which the bulk cohesion is stronger than the gravity. At the particle scale, we used the high precision torque measurement of an industrial rheometer to measure the inter-particle cohesion, the reproducibility of the contact and the effect of the precompression load. Our experiment also showed a stable cohesion with the different conditions for one pair of particles at each measurements. we developed a set up that used the gravity to perform measurements on several pairs of particles at the same time to get a statistic view of the cohesion distribution in a batch of particles. These tools allowed us to characterize the inter-particles cohesion force as a function

of the size of the particles and the average coating b, and to link this inter-particle force to the bulk cohesion through the cohesive length ℓ_c. The ability to tune the inter-particle and the bulk cohesion allowed us to consider some standard configuration experiments to test the flow properties of cohesive materials and compare theses configurations with numerical simulations.

In collaboration with Alban Sauret at the University of Santa-Barbara, we considered the Jet Erosion Test configuration to test the threshold of transport. This experiment, presented in chapter 3, consisted in blowing a turbulent air flow on the granular material and observe for which air velocity the cohesive particles are eroded. The experiments showed that the condition to erode a grain are modified due to the inter-particles cohesion, and we were able to account for the cohesion in the description of the erosion threshold. This experiment provided a first approach on the transition to transport of cohesive granular materials.

Another approach developed in this work, presented in chapter 4 is the study of the silo discharge of cohesive granular media. While the Jet Erosion test provided an understanding of the transport transition at the particle scale, the silo discharge allowed to study the flowing properties of the CCGM. Two configurations were considered for this work. First, the axisymmetric silo allowed to characterise the flow threshold of the granular media depending on its cohesion. The introduction of the cohesive length ℓ_c as an effective size in the ϕ_0 parameter of the granular discharge indicates that a cohesive granular material may be considered as a cohesionless granular material composed of grains with an effective diameter ℓ_c. This description captures most of the mass flow rate behavior of the discharge. However, it is based on the assumption that the cohesive media dilates more but falls at the same speed as cohesionless media at the outlet. The second configuration considered in the chapter was a quasi-2D silo experiment. The study of the velocity field at the outlet of the silo allowed to determine that the velocity at the outlet of the silo was decreasing with cohesion. However, a detailed analysis of the velocity field suggested that, although the velocity of the CCGM tends to decrease with the increase of cohesion, the cohesive materials also tends to dilate more than the cohesionless material at the outlet. These results indicate that the parameter ϕ_0 was not only tied to the dilatation of the granular media at the outlet, but also tied to the velocity. Theses results also seem to be supported by the numerical continuum modelling of the cohesive granular silo discharge.

The last approach developed at Santa-Barbara University, presented in chapter 5 focused on the collapse of a cohesive granular column. This experiment had several purposes. First it allowed us to test our knowledge about the bulk cohesion and the stability of a granular column as a function of the cohesion. Second this experiment is quite easy to simulate numerically and, following several precaution, may be compared to the experimental results. Indeed, when the column collapses, the characteristics of the spread of the granular media (velocity and run-out) are directly related to the rheology. This makes the granular collapse a good experiment to test the cohesive rheology. The experiments performed on the stability of a column showed that the threshold of stability is mostly governed by the ratio between the cohesion and

the static pressure and can be understood by simple arguments based on the stability of a corner. The detail of the velocity of the pile foot during the fall indicates that the cohesion decreases the velocity. More importantly, the dynamics of the collapse seems well captured by a continuous simulation based on the cohesive $\mu(I)$ rheology. However, the last time steps of the cohesive collapse do not seem well captured by the model, and therefore the run-out of the cohesive collapse is not consistent with the experiments. This problem may be solved by a modification of the $\Delta\mu$ factor in the rheology, however it clearly indicates that a deeper investigation on the rheology of the CCGM is needed.

Although the parameter ℓ_c is a relevant parameter to represent the flowability under gravity, this work did not highlight an obvious parameter characterizing the flowability of cohesive granular materials. A deeper investigation on the rheology might be needed to bond the particle scale limit of transport and the bulk scale limit of flowability, and also the ability of a cohesive flow to be maintained. This work will be carried out in the futur using the pressure imposed rheometer available at IUSTI lab; some preliminary result have been obtained and more experiments will be performed to find out a better understanding of the behavior of cohesive granular media.

Bibliography

[1] Robert Leslie Brown and John Colin Richards. *Principles of powder mechanics: essays on the packing and flow of powders and bulk solids*. Vol. 10. Elsevier, 1970 (cit. on pp. 23, 28, 35, 86).

[2] R.M. Nedderman. "Statics and kinematics of granular materials". In: *Cambridge University Press* (1992) (cit. on pp. 23, 83, 86).

[3] Étienne Guyon and Jean-Paul Troadec. *Du sac de billes au tas de sable*. Odile Jacob, 1994 (cit. on p. 23).

[4] Jacques Duran. *Sables, poudres et grains*. BOOK. Eyrolles, 1997 (cit. on p. 23).

[5] K Kesava Rao, Prabhu R Nott, and S Sundaresan. *An introduction to granular flow*. Vol. 10. Cambridge university press New York, 2008 (cit. on p. 23).

[6] Bruno Andreotti, Yoël Forterre, and Olivier Pouliquen. *Les milieux granulaires-entre fluide et solide: Entre fluide et solide*. EDP sciences, 2012 (cit. on pp. 23, 25, 29, 33, 41, 42, 45, 79, 84).

[7] William Bailey Russel et al. *Colloidal dispersions*. Cambridge university press, 1991 (cit. on pp. 23, 28).

[8] Lyn Bates. "Bulk Solids Characterisation-The Need for industrial Education in Bulk Technology". In: *Bulk Solids Handling* 26.7 (2006), pp. 464–475 (cit. on p. 23).

[9] Heinrich M Jaeger, Sidney R Nagel, and Robert P Behringer. "Granular solids, liquids, and gases". In: *Reviews of modern physics* 68.4 (1996), p. 1259 (cit. on p. 24).

[10] Yoël Forterre and Olivier Pouliquen. "Flows of dense granular media". In: *Annu. Rev. Fluid Mech.* 40 (2008), pp. 1–24 (cit. on pp. 24, 26, 45).

[11] Aleksandar Donev et al. "Improving the density of jammed disordered packings using ellipsoids". In: *Science* 303.5660 (2004), pp. 990–993 (cit. on p. 25).

[12] MJ Powell. "Computer-simulated random packing of spheres". In: *Powder technology* 25.1 (1980), pp. 45–52 (cit. on pp. 25, 27).

[13] G David Scott and D Marc Kilgour. "The density of random close packing of spheres". In: *Journal of Physics D: Applied Physics* 2.6 (1969), p. 863 (cit. on p. 25).

[14] William M Visscher and M Bolsterli. “Random packing of equal and unequal spheres in two and three dimensions”. In: *Nature* 239.5374 (1972), pp. 504–507 (cit. on p. 25).

[15] W Steven Jodrey and Elmer M Tory. “Simulation of random packing of spheres”. In: *Simulation* 32.1 (1979), pp. 1–12 (cit. on p. 25).

[16] DJ Cumberland and Roy James Crawford. “The packing of particles”. In: (1987) (cit. on p. 25).

[17] Frédéric Da Cruz et al. “Rheophysics of dense granular materials: Discrete simulation of plane shear flows”. In: *Physical Review E* 72.2 (2005), p. 021309 (cit. on p. 26).

[18] Ivan Iordanoff and MM Khonsari. “Granular lubrication: toward an understanding of the transition between kinetic and quasi-fluid regime”. In: *J. Trib.* 126.1 (2004), pp. 137–145 (cit. on p. 26).

[19] Olivier Pouliquen and Yoël Forterre. “Friction law for dense granular flows: application to the motion of a mass down a rough inclined plane”. In: *Journal of Fluid Mechanics* 453 (2002), pp. 133–151 (cit. on p. 27).

[20] Yoël Forterre and Olivier Pouliquen. “Long surface wave instability in dense granular flows”. In: *arXiv preprint cond-mat/0303017* (2003) (cit. on p. 27).

[21] GDR MiDi. “On dense granular flows”. In: *The European Physical Journal E* 14.4 (2004), pp. 341–365 (cit. on p. 27).

[22] Pierre Jop, Yoël Forterre, and Olivier Pouliquen. “Crucial role of side walls for granular surface flows: consequences for the rheology”. In: *arXiv preprint cond-mat/0503425* (2005) (cit. on p. 27).

[23] Olivier Pouliquen et al. “Flow of dense granular material: towards simple constitutive laws”. In: *Journal of Statistical Mechanics: Theory and Experiment* 2006.07 (2006), P07020 (cit. on p. 27).

[24] Lydie Staron, P-Y Lagrée, and Stéphane Popinet. “The granular silo as a continuum plastic flow: The hour-glass vs the clepsydra”. In: *Physics of Fluids* 24.10 (2012), p. 103301 (cit. on pp. 27, 83, 86).

[25] L Staron, P-Y Lagrée, and S Popinet. “Continuum simulation of the discharge of the granular silo”. In: *The European Physical Journal E* 37.1 (2014), p. 5 (cit. on pp. 27, 86, 87).

[26] Lagrée, Lydie Staron, and Stéphane Popinet. “The granular column collapse as a continuum: validity of a two-dimensional Navier-Stokes model with a [mu](I)-rheology”. In: *Journal of Fluid Mechanics* 686 (2011), p. 378 (cit. on pp. 27, 92, 106).

[27] Pierre Jop, Yoël Forterre, and Olivier Pouliquen. “A constitutive law for dense granular flows”. In: *Nature* 441.7094 (2006), pp. 727–730 (cit. on p. 27).

[28] Forterre. "Kapiza waves as a test for three-dimensional granular flow rheology". In: *Journal of Fluid Mechanics* 563 (2006), p. 123 (cit. on p. 27).

[29] Laurent Lacaze and Rich R Kerswell. "Axisymmetric granular collapse: a transient 3D flow test of viscoplasticity". In: *Physical Review Letters* 102.10 (2009), p. 108305 (cit. on pp. 27, 106).

[30] Y Zhou et al. "Experiments, discrete and continuum simulations of, the discharge of granular media from silos with a lateral orifice". In: *Journal of Fluid Mechanics* 829 (2017), pp. 459–485 (cit. on pp. 27, 83, 86, 89).

[31] Z Zou et al. "Discharge of a silo through a lateral orifice: Role of the bottom inclination versus friction". In: *Physical Review E* 102.5 (2020), p. 052902 (cit. on pp. 27, 83, 89, 95).

[32] Olivier Pouliquen and Yoel Forterre. "A non-local rheology for dense granular flows". In: *Philosophical Transactions of the Royal Society A: Mathematical, Physical and Engineering Sciences* 367.1909 (2009), pp. 5091–5107 (cit. on p. 27).

[33] Ken Kamrin. "Nonlinear elasto-plastic model for dense granular flow". In: *International Journal of Plasticity* 26.2 (2010), pp. 167–188 (cit. on p. 27).

[34] Tamás Börzsönyi and Robert E Ecke. "Rapid granular flows on a rough incline: Phase diagram, gas transition, and effects of air drag". In: *Physical Review E* 74.6 (2006), p. 061301 (cit. on p. 27).

[35] Sam F Edwards and RBS Oakeshott. "Theory of powders". In: *Physica A: Statistical Mechanics and its Applications* 157.3 (1989), pp. 1080–1090 (cit. on p. 28).

[36] PS Whitfield, A Huq, and JA Kaduk. "Powders and particle statistics (granularity)". In: (2019) (cit. on p. 28).

[37] Robert Leslie Brown and JC Richards. "Kinematics of the flow of dry powders and bulk solids". In: *Rheologica Acta* 4.3 (1965), pp. 153–165 (cit. on pp. 28, 35, 89).

[38] David Train. "Some aspects of the property of angle of repose of powders". In: *Journal of Pharmacy and Pharmacology* 10.S1 (1958), 127T–135T (cit. on p. 28).

[39] Rupert Stevenson Bradley. "LXXIX. The cohesive force between solid surfaces and the surface energy of solids". In: *The London, Edinburgh, and Dublin Philosophical Magazine and Journal of Science* 13.86 (1932), pp. 853–862 (cit. on p. 29).

[40] Hugo C Hamaker. "The London—van der Waals attraction between spherical particles". In: *physica* 4.10 (1937), pp. 1058–1072 (cit. on pp. 29, 31).

[41] E.M. Lifshitz. "Soviet Phys. JETP 2, 73 (1956)". In: *J. exp. theor. Phys. USSR* 29 (1955), p. 94 (cit. on p. 29).

[42] Boris V Derjaguin, Vladimir M Muller, and Yu P Toporov. "Effect of contact deformations on the adhesion of particles". In: *Journal of Colloid and interface science* 53.2 (1975), pp. 314–326 (cit. on pp. 29, 30).

[43] E. M. Lifshitz, M Hamermesh, et al. "The theory of molecular attractive forces between solids". In: *Perspectives in Theoretical Physics*. Elsevier, 1992, pp. 329–349 (cit. on p. 29).

[44] Jacob N Israelachvili. *Intermolecular and surface forces*. Academic press, 2011 (cit. on p. 29).

[45] Heinrich Hertz. *Miscellaneous papers*. Macmillan, 1896 (cit. on p. 29).

[46] KL Johnson and JA Greenwood. "An adhesion map for the contact of elastic spheres". In: *Journal of colloid and interface science* 192.2 (1997), pp. 326–333 (cit. on p. 29).

[47] JA Greenwood. "Adhesion of elastic spheres". In: *Proceedings of the Royal Society of London. Series A: Mathematical, Physical and Engineering Sciences* 453.1961 (1997), pp. 1277–1297 (cit. on p. 29).

[48] Haimin Yao, Michele Ciavarella, and Huajian Gao. "Adhesion maps of spheres corrected for strength limit". In: *Journal of colloid and interface science* 315.2 (2007), pp. 786–790 (cit. on p. 29).

[49] K.L. Johnson, K. Kendall, and A. D. Roberts. "Surface energy and the contact of elastic solids". In: *Proceedings of the royal society of London. A. mathematical and physical sciences* 324.1558 (1971), pp. 301–313 (cit. on pp. 30, 67).

[50] D Tabor. "Surface forces and surface interactions". In: *Plenary and invited lectures*. Elsevier, 1977, pp. 3–14 (cit. on p. 30).

[51] Daniel Maugis. "Adhesion of spheres: the JKR-DMT transition using a Dugdale model". In: *Journal of colloid and interface science* 150.1 (1992), pp. 243–269 (cit. on p. 30).

[52] Donald Allan McQuarrie and John Douglas Simon. *Physical chemistry: a molecular approach*. Vol. 1. University science books Sausalito, CA, 1997 (cit. on p. 30).

[53] L. Bocquet et al. "Moisture-induced ageing in granular media and the kinetics of capillary condensation". In: *Nature* 396 (1998), pp. 735–737 (cit. on pp. 31, 43).

[54] D.W. Howell, I.S. Aranson, and G.W. Crabtree. "Dynamics of electrostatically-driven granular media. Effects of Humidity". In: *Physical Review E* 63 (2001), p. 050301 (cit. on p. 31).

[55] R. Jones et al. "Inter-particle forces in cohesive powders studied by AFM: effects of relative humidity, particle size and wall adhesion". In: *Powder Technology* 132 (2003), pp. 196–210 (cit. on pp. 31, 34, 35).

[56] S. R. Miles. “The relation between the moisture content and the test weight of corn”. In: *J. Am. Soc. Agronomy* 29 (1937), pp. 412–418 (cit. on pp. 31, 54).

[57] N. Vandewalle et al. “How relative humidity affects random packing experiments”. In: *Physical Review E* 85 (2012), p. 031309 (cit. on p. 31).

[58] Christoph Gögelein et al. “Controlling the formation of capillary bridges in binary liquid mixtures”. In: *Langmuir* 26.22 (2010), pp. 17184–17189 (cit. on p. 32).

[59] Pierre-Gilles De Gennes, Françoise Brochard-Wyart, and David Quéré. *Capillarity and wetting phenomena: drops, bubbles, pearls, waves*. Springer Science & Business Media, 2013 (cit. on p. 32).

[60] Thomas C. Halsey and Alex J. Levine. “How Sandcastles Fall”. In: *Physical Review Letters* 80.14 (1998), pp. 3141–3144 (cit. on pp. 33, 41, 68).

[61] AS Pereyra Gonzales et al. “Maillard reaction kinetics in milk powder: Effect of water activity at mild temperatures”. In: *International Dairy Journal* 20.1 (2010), pp. 40–45 (cit. on p. 34).

[62] Kyu Seob Chang et al. “Bulk flow properties of model food powder at different water activity”. In: *International Journal of Food Properties* 1.1 (1998), pp. 45–55 (cit. on p. 34).

[63] L. Konopka and J. Kosek. “Discrete element modeling of electrostatic charging of polyethylene powder particles”. In: *Journal of electrostatics* 87 (2017), pp. 150–157 (cit. on p. 34).

[64] Zhiguo Wang et al. “Aging behavior of nano-SiC/2014Al composite fabricated by powder metallurgy and hot extrusion techniques”. In: *Journal of Materials Science & Technology* 32.10 (2016), pp. 1008–1012 (cit. on p. 34).

[65] Henry Darcy. *Recherches expérimentales relatives au mouvement de l’eau dans les tuyaux*. Vol. 1. Mallet-Bachelier, 1857 (cit. on p. 35).

[66] Philip Crosbie Carman. “Fluid flow through granular beds”. In: *Trans. Inst. Chem. Eng.* 15 (1937), pp. 150–166 (cit. on p. 35).

[67] Josef Kozeny. “Uber kapillare leitung der wasser in boden”. In: *Royal Academy of Science, Vienna, Proc. Class I* 136 (1927), pp. 271–306 (cit. on p. 35).

[68] JLR Orband and D Geldart. “Direct measurement of powder cohesion using a torsional device”. In: *Powder Technology* 92.1 (1997), pp. 25–33 (cit. on p. 35).

[69] A. Castellanos. “The relationship between attractive interparticle forces and bulk behaviour in dry and uncharged fine powders”. In: *Advances in Physics* 54.4 (2005), pp. 263–376 (cit. on p. 35).

[70] A. W. Alexander et al. “Avalanching flow of cohesive powders”. In: *Powder Technology* 164 (2006), pp. 13–21 (cit. on p. 35).

[71] A. de Ryck, R. Condotta, and J. A. Dodds. "Shape of a cohesive granular heap". In: *Powder Technology* 157 (2005), pp. 72–78 (cit. on pp. 35, 54).

[72] Tian Hao. "Understanding empirical powder flowability criteria scaled by Hausner ratio or Carr index with the analogous viscosity concept". In: *RSC advances* 5.70 (2015), pp. 57212–57215 (cit. on p. 35).

[73] M.V. V. Antequera et al. "Evaluation of an adequate method of estimating flowability according to powder characteristics". In: *International Journal of Pharmaceutics* 103 (1994), pp. 155–161 (cit. on p. 35).

[74] A. Hassanpour, C. Hare, and M. Pasha, eds. *Powder Flow: Theory, Characterisation and Application*. Royal Society of Chemistry, 2019 (cit. on pp. 35, 57).

[75] James F Klausner, Dongming Chen, and Renwei Mei. "Experimental investigation of cohesive powder rheology". In: *Powder Technology* 112.1-2 (2000), pp. 94–101 (cit. on pp. 35, 164).

[76] Ezzat Chan Abdullah and Derek Geldart. "The use of bulk density measurements as flowability indicators". In: *Powder technology* 102.2 (1999), pp. 151–165 (cit. on pp. 35, 165).

[77] P Rognon et al. "Rheology of cohesive granular materials: discrete simulation of plane shear flows". In: *J. Fluid Mech* (2006) (cit. on p. 36).

[78] Alain De Ryck, Renaud Ansart, and John A Dodds. "Granular flows down inclined channels with a strain-rate dependent friction coefficient. Part I: Non-cohesive materials". In: *Granular Matter* 10.5 (2008), p. 353 (cit. on p. 36).

[79] D. Geldart et al. "CHARACTERIZATION OF POWDER FLOWABILITY USING MEASUREMENT OF ANGLE OF REPOSE". In: *China Particuology* 4.3-4 (2006), pp. 104–107 (cit. on p. 36).

[80] Stefan Luding. "Cohesive, frictional powders: contact models for tension". In: *Granular matter* 10.4 (2008), p. 235 (cit. on p. 36).

[81] Qin Li et al. "Interparticle van der Waals force in powder flowability and compactibility". In: *International journal of pharmaceutics* 280.1-2 (2004), pp. 77–93 (cit. on p. 36).

[82] James K Prescott and Roger A Barnum. "On powder flowability". In: *Pharmaceutical technology* 24.10 (2000), pp. 60–85 (cit. on p. 36).

[83] François Peters and Elisabeth Lemaire. "Cohesion induced by a rotating magnetic field in a granular material". In: *Physical Review E* 69.6 (2004), p. 061302 (cit. on pp. 37, 38).

[84] Arnaud Hemmerle et al. *Cohesive granular material*. US Patent App. 16/249,092. May 2019 (cit. on p. 38).

[85] Saurabh Singh et al. "System size effects on the mechanical response of cohesive-frictional granular ensembles". In: *EPJ Web of Conferences*. Vol. 140. EDP Sciences. 2017, p. 08007 (cit. on pp. 38, 39).

[86] Jean-Yves Delenne et al. “Mechanical behaviour and failure of cohesive granular materials”. In: *International Journal for Numerical and Analytical Methods in Geomechanics* 28.15 (2004), pp. 1577–1594 (cit. on pp. 38, 39).

[87] Mika M Kohonen et al. “On capillary bridges in wet granular materials”. In: *Physica A: Statistical Mechanics and its Applications* 339.1-2 (2004), pp. 7–15 (cit. on p. 39).

[88] N Huang et al. “Flow of wet granular materials”. In: *Physical review letters* 94.2 (2005), p. 028301 (cit. on p. 39).

[89] Z Fournier et al. “Mechanical properties of wet granular materials”. In: *Journal of Physics: Condensed Matter* 17.9 (2005), S477 (cit. on p. 39).

[90] V. Richefeu, M.-S. El Youssoufi, and F. Radjai. “Shear strength properties of wet granular materials”. In: *Physical Review E* 73.5 (2006), p. 051304 (cit. on pp. 39, 42, 43, 69, 70).

[91] N. Mitarai and F. Nori. “Wet granular materials”. In: *Advances in physics* 55.1-2 (2006), pp. 1–45 (cit. on p. 39).

[92] P Tegzes, T Vicsek, and P Schiffer. “Avalanche dynamics in wet granular materials”. In: *Physical review letters* 89.9 (2002), p. 094301 (cit. on pp. 39, 40).

[93] Qing Xu, Ashish V Orpe, and Arshad Kudrolli. “Lubrication effects on the flow of wet granular materials”. In: *Physical Review E* 76.3 (2007), p. 031302 (cit. on pp. 39, 40).

[94] QJ Zheng and AB Yu. “Modelling the granular flow in a rotating drum by the Eulerian finite element method”. In: *Powder Technology* 286 (2015), pp. 361–370 (cit. on p. 40).

[95] Sudeshna Roy et al. “Micro–macro transition and simplified contact models for wet granular materials”. In: *Computational particle mechanics* 3.4 (2016), pp. 449–462 (cit. on p. 40).

[96] Ahmed Jarray et al. “Scaling of wet granular flows in a rotating drum”. In: *EPJ Web of Conferences*. Vol. 140. EDP Sciences. 2017, p. 03078 (cit. on p. 40).

[97] Guanjin Wang, Amir Riaz, and Balakumar Balachandran. “Smooth particle hydrodynamics studies of wet granular column collapses”. In: *Acta Geotechnica* (2019), pp. 1–13 (cit. on pp. 40, 108).

[98] Riccardo Artoni et al. “Collapse of quasi-two-dimensional wet granular columns”. In: *Physical Review E* 87.3 (2013), p. 032205 (cit. on pp. 40, 41, 108, 109).

[99] N.J. Balmforth and R. Kerswell. “Granular collapse in two dimensions.” In: *J. Fluid Mech.* 538 (2005), pp. 339–428 (cit. on pp. 40, 106).

[100] E Lajeunesse, JB Monnier, and GM Homsy. “Granular slumping on a horizontal surface”. In: *Physics of fluids* 17.10 (2005), p. 103302 (cit. on pp. 40, 106–108).

[101] Réka Albert et al. “Maximum angle of stability in wet and dry spherical granular media”. In: *Physical Review E* 56.6 (1997), R6271 (cit. on p. 40).

[102] Albert-László Barabási, Réka Albert, and Peter Schiffer. “The physics of sand castles: maximum angle of stability in wet and dry granular media”. In: *Physica A: Statistical Mechanics and its Applications* 266.1-4 (1999), pp. 366–371 (cit. on p. 40).

[103] Mario Scheel et al. “Morphological clues to wet granular pile stability”. In: *Nature materials* 7.3 (2008), pp. 189–193 (cit. on p. 40).

[104] P. Møller M. Pakpour M. Habibi and D. Bonn. “How to construct the perfect sandcastle”. In: *Scientific Reports* 2.1 (2012), p. 549 (cit. on p. 40).

[105] AM Taylor-Noonan et al. “Stability of saturated granular columns: Role of stress-dilatancy and capillarity”. In: *Physics of Fluids* 33.3 (2021), p. 033309 (cit. on p. 40).

[106] A Mangeney et al. “Erosion and mobility in granular collapse over sloping beds”. In: *Journal of Geophysical Research: Earth Surface* 115.F3 (2010) (cit. on p. 40).

[107] Andrea Claudio Santomaso, Silvia Volpato, and Fabio Gabrieli. “Collapse and runout of granular columns in pendular state”. In: *Physics of Fluids* 30.6 (2018), p. 063301 (cit. on p. 40).

[108] Fabio Gabrieli et al. “Discrete particle simulations and experiments on the collapse of wet granular columns”. In: *Physics of fluids* 25.10 (2013), p. 103303 (cit. on p. 40).

[109] Francesca Ceccato et al. “Numerical and experimental investigation of saturated granular column collapse in air”. In: *Soils and Foundations* 60.3 (2020), pp. 683–696 (cit. on p. 40).

[110] Lydéric Bocquet, Elisabeth Charlaix, and Frédéric Restagno. “Physics of humid granular media”. In: *Comptes Rendus Physique* 3.2 (2002), pp. 207–215 (cit. on p. 41).

[111] Frédéric Restagno et al. “Aging in humid granular media”. In: *Physical review E* 66.2 (2002), p. 021304 (cit. on p. 41).

[112] Roman Mani, Dirk Kadau, and Hans J Herrmann. “Liquid migration in sheared unsaturated granular media”. In: *Granular Matter* 15.4 (2013), pp. 447–454 (cit. on p. 41).

[113] Guillaume Saingier, Alban Sauret, and Pierre Jop. “Accretion dynamics on wet granular materials”. In: *Physical review letters* 118.20 (2017), p. 208001 (cit. on p. 41).

[114] PY Liu, RY Yang, and AB Yu. “Self-diffusion of wet particles in rotating drums”. In: *Physics of Fluids* 25.6 (2013), p. 063301 (cit. on p. 41).

[115] Thanh Trung Vo et al. “Agglomeration of wet particles in dense granular flows”. In: *The European Physical Journal E* 42.9 (2019), pp. 1–12 (cit. on p. 41).

[116] Wolfgang Pietsch, Egon Hoffman, and Hans Rumpf. “Tensile strength of moist agglomerates”. In: *Industrial & Engineering Chemistry Product Research and Development* 8.1 (1969), pp. 58–62 (cit. on p. 42).

[117] P. C. F. Møller and D. Bonn. “The shear modulus of wet granular matter”. In: *Europhysics Letters* 80.3 (2007), p. 38002 (cit. on p. 42).

[118] R. Albert et al. “Maximum angle of stability in wet and dry spherical granular media”. In: *Physical Review E* 56.6 (1997), pp. 6271–6274 (cit. on pp. 43, 54, 55).

[119] TG Mason et al. “Critical angle of wet sandpiles”. In: *Physical Review E* 60.5 (1999), R5044 (cit. on p. 43).

[120] P. Tegzes et al. “Liquid-induced transitions in granular media”. In: *Physical Review E* 60.5 (1999), pp. 5823–5826 (cit. on pp. 43, 54, 55).

[121] S. Nowak, A. Samadani, and A. Kudrolli. “Maximum angle of stability of a wet granular pile”. In: *Nature* 1 (2005), pp. 50–52 (cit. on p. 43).

[122] Pierre G Rognon et al. “Dense flows of cohesive granular materials”. In: *Journal of Fluid Mechanics* 596 (2008), pp. 21–47 (cit. on p. 44).

[123] Nicolas Berger et al. “Scaling behaviour of cohesive granular flows”. In: *EPL (Europhysics Letters)* 112.6 (2016), p. 64004 (cit. on p. 44).

[124] Saeed Khamseh, Jean-Noël Roux, and François Chevoir. “Flow of wet granular materials: A numerical study”. In: *Physical Review E* 92.2 (2015), p. 022201 (cit. on p. 44).

[125] M Badetti et al. “Shear strength of wet granular materials: macroscopic cohesion and effective stress”. In: *The European Physical Journal E* 41.5 (2018), pp. 1–16 (cit. on p. 44).

[126] M. Badetti et al. “Rheology and microstructure of unsaturated granular materials: Experiments and simulations”. In: *Journal of rheology* 62 (2018), p. 1175 (cit. on p. 45).

[127] Osamu Kuwano, Ryosuke Ando, and Takahiro Hatano. “Crossover from negative to positive shear rate dependence in granular friction”. In: *Geophysical research letters* 40.7 (2013), pp. 1295–1299 (cit. on pp. 45, 46, 141).

[128] Sandip Mandal, Maxime Nicolas, and Olivier Pouliquen. “Insights into the rheology of cohesive granular media”. In: *Proceedings of the National Academy of Sciences* 117.15 (2020), pp. 8366–8373 (cit. on pp. 46, 134).

[129] Sandip Mandal, Maxime Nicolas, and Olivier Pouliquen. “Rheology of Cohesive Granular Media: Shear Banding, Hysteresis, and Nonlocal Effects”. In: *Physical Review X* 11.2 (2021), p. 021017 (cit. on pp. 46, 47).

[130] Adrien Gans, Olivier Pouliquen, and Maxime Nicolas. "Cohesion-controlled granular material". In: *Physical Review E* 101.3 (2020), p. 032904 (cit. on p. 50).

[131] J. Modell and S. Thuresson. "Material composition and method for its manufacturing". In: *Patent* WO2008/020800A1 (2008) (cit. on p. 50).

[132] X. Li et al. "Synthesis of polyborosiloxane and its reversible physical crosslinks". In: *RSC Advances* 4 (2014), 32894Ð–32901 (cit. on p. 50).

[133] E. F. Wolf and H. L. Hohenleiten. "Experimental study of the flow of coal in chutes". In: *Trans. Am. Soc. Mech. Eng* 67 (1945), pp. 585–599 (cit. on p. 54).

[134] A. Samadani and A. Kudrolli. "Angle of repose and segregation in cohesive granular matter". In: *Physical Review E* 64.5 (2001), pp. 051301-1–051301-9 (cit. on p. 54).

[135] N. Standish, A.B. Yu, and Q.L. He. "An experimental study of the packing of a coal heap". In: *Powder Tech.* 68 (1991), pp. 187–193 (cit. on p. 57).

[136] T. Kobayashi et al. "DEM-CFD analysis of fluidization behavior of Geldart Group A particles using a dynamic adhesion force model". In: *Powder Technology* 248 (2013), pp. 143–152 (cit. on p. 64).

[137] Emmanuel Partheniades. "Erosion and deposition of cohesive soils". In: *Journal of the Hydraulics Division* 91.1 (1965), pp. 105–139 (cit. on p. 72).

[138] Etienne Bousser, L Martinu, and JE Klemberg-Sapieha. "Solid particle erosion mechanisms of protective coatings for aerospace applications". In: *Surface and Coatings Technology* 257 (2014), pp. 165–181 (cit. on p. 72).

[139] Chi Fai Wan and Robin Fell. "Investigation of rate of erosion of soils in embankment dams". In: *Journal of geotechnical and geoenvironmental engineering* 130.4 (2004), pp. 373–380 (cit. on p. 72).

[140] Philip T Metzger, Jacob Smith, and John E Lane. "Phenomenology of soil erosion due to rocket exhaust on the Moon and the Mauna Kea lunar test site". In: *Journal of Geophysical Research: Planets* 116.E6 (2011) (cit. on p. 72).

[141] S De Baets et al. "Modelling increased soil cohesion due to roots with EUROSEM". In: *Earth Surface Processes and Landforms: The Journal of the British Geomorphological Research Group* 33.13 (2008), pp. 1948–1963 (cit. on p. 72).

[142] Rajiv Kohli and KL Mittal. *Developments in Surface Contamination and Cleaning: Applications of Cleaning Techniques: Volume 11*. Vol. 11. Elsevier, 2018 (cit. on p. 72).

[143] Albert Shields. "Anwendung der Aehnlichkeitsmechanik und der Turbulenzforschung auf die Geschiebebewegung". In: *PhD Thesis Technical University Berlin* (1936) (cit. on p. 72).

[144] Hunter Rouse. "Modern conceptions of the mechanics of fluid turbulence". In: *Transactions of the American Society of Civil Engineers* 102.1 (1937), pp. 463–505 (cit. on p. 73).

[145] Raymond M Brach. "Impact dynamics with applications to solid particle erosion". In: *International journal of impact engineering* 7.1 (1988), pp. 37–53 (cit. on p. 73).

[146] R Sam Williams et al. "Erosion rates of wood during natural weathering. Part III. Effect of exposure angle on erosion rate". In: *Wood and fiber science* 33.1 (2001), pp. 50–57 (cit. on p. 73).

[147] Guidoux Cyril et al. "Contact erosion at the interface between granular coarse soil and various base soils under tangential flow condition". In: *Journal of geotechnical and geoenvironmental engineering* 136.5 (2010), pp. 741–750 (cit. on p. 73).

[148] Arman Haddadchi et al. "An alternative method for interpreting JET erosion test (JET) data: Part 2. Application". In: *Earth Surface Processes and Landforms* 43.3 (2018), pp. 743–754 (cit. on p. 73).

[149] Sarah Badr, Georges Gauthier, and Philippe Gondret. "Erosion threshold of a liquid immersed granular bed by an impinging plane liquid jet". In: *Physics of Fluids* 26.2 (2014), p. 023302 (cit. on pp. 73, 76, 77, 79–82).

[150] Florian Brunier-Coulin, Pablo Cuéllar, and Pierre Philippe. "Erosion onset of a cohesionless granular medium by an immersed impinging round jet". In: *Physical Review Fluids* 2.3 (2017), p. 034302 (cit. on p. 73).

[151] Jacobus J Derksen. "Simulations of granular bed erosion due to laminar shear flow near the critical Shields number". In: *Physics of Fluids* 23.11 (2011), p. 113303 (cit. on p. 73).

[152] Florian Brunier-Coulin, Pablo Cuéllar, and Pierre Philippe. "Generalized Shields criterion for weakly cohesive granular materials". In: *Physical Review Fluids* 5.3 (2020), p. 034308 (cit. on p. 73).

[153] JR Agudo and Andreas Wierschem. "Incipient motion of a single particle on regular substrates in laminar shear flow". In: *Physics of Fluids* 24.9 (2012), p. 093302 (cit. on p. 79).

[154] Brian P Tighe and Matthias Sperl. "Pressure and motion of dry sand: translation of Hagen's paper from 1852". In: *Granular Matter* 9.3-4 (2007), pp. 141–144 (cit. on pp. 83, 86).

[155] Wim A Beverloo, Hendrik Antonie Leniger, and J Van de Velde. "The flow of granular solids through orifices". In: *Chemical engineering science* 15.3-4 (1961), pp. 260–269 (cit. on pp. 83, 87).

[156] U Tüzün and RM Nedderman. "An investigation of the flow boundary during steady-state discharge from a funnel-flow bunker". In: *Powder Technology* 31.1 (1982), pp. 27–43 (cit. on p. 83).

[157] C Mankoc et al. "The flow rate of granular materials through an orifice". In: *Granular Matter* 9.6 (2007), pp. 407–414 (cit. on pp. 83, 88).

[158] Alvaro Janda, Iker Zuriguel, and Diego Maza. "Flow rate of particles through apertures obtained from self-similar density and velocity profiles". In: *Physical review letters* 108.24 (2012), p. 248001 (cit. on pp. 83, 86–88).

[159] Iker Zuriguel et al. "Clogging transition of many-particle systems flowing through bottlenecks". In: *Scientific reports* 4.1 (2014), pp. 1–8 (cit. on p. 83).

[160] Sara Maria Rubio-Largo et al. "Disentangling the free-fall arch paradox in silo discharge". In: *Physical review letters* 114.23 (2015), p. 238002 (cit. on p. 83).

[161] Y Zhou, P Ruyer, and P Aussillous. "Discharge flow of a bidisperse granular media from a silo: discrete particle simulations". In: *Physical Review E* 92.6 (2015), p. 062204 (cit. on pp. 83, 89, 103).

[162] D Hirshfeld and DC Rapaport. "Granular flow from a silo: discrete-particle simulations in three dimensions". In: *The European Physical Journal E* 4.2 (2001), pp. 193–199 (cit. on p. 83).

[163] Chris H Rycroft et al. "Analysis of granular flow in a pebble-bed nuclear reactor". In: *Physical review E* 74.2 (2006), p. 021306 (cit. on p. 83).

[164] JE Hilton and PW Cleary. "Granular flow during hopper discharge". In: *Physical Review E* 84.1 (2011), p. 011307 (cit. on p. 83).

[165] L Vanel and E Clément. "Pressure screening and fluctuations at the bottom of a granular column". In: *The European Physical Journal B-Condensed Matter and Complex Systems* 11.3 (1999), pp. 525–533 (cit. on p. 84).

[166] L Vanel et al. "Stresses in silos: comparison between theoretical models and new experiments". In: *Physical review letters* 84.7 (2000), p. 1439 (cit. on p. 84).

[167] G Ovarlez, C Fond, and E Clément. "Overshoot effect in the Janssen granular column: a crucial test for granular mechanics". In: *Physical Review E* 67.6 (2003), p. 060302 (cit. on p. 84).

[168] Thomas Cambau, Jérémy Hure, and Joël Marthelot. "Local stresses in the janssen granular column". In: *Physical Review E* 88.2 (2013), p. 022204 (cit. on p. 84).

[169] Iker Zuriguel et al. "Jamming during the discharge of granular matter from a silo". In: *Physical Review E* 71.5 (2005), p. 051303 (cit. on p. 85).

[170] Cristian Mankoc et al. "Role of vibrations in the jamming and unjamming of grains discharging from a silo". In: *Physical Review E* 80.1 (2009), p. 011309 (cit. on p. 85).

[171] A Janda et al. "Unjamming a granular hopper by vibration". In: *EPL (Europhysics Letters)* 87.2 (2009), p. 24002 (cit. on p. 85).

[172] Angel Garcimartin et al. "Flow and jamming of granular matter through an orifice". In: *Traffic and Granular Flow'07*. Springer, 2009, pp. 471–486 (cit. on p. 85).

[173] I Zuriguel and A Garcimartın. “Statistical Mechanics of Clogging”. In: (2020) (cit. on p. 85).

[174] Thierry Le Pennec et al. “Ticking hour glasses: experimental analysis of intermittent flow”. In: *Physical Review E* 53.3 (1996), p. 2257 (cit. on p. 85).

[175] Kiwing To and Hsiang-Ting Tai. “Flow and clog in a silo with oscillating exit”. In: *Physical Review E* 96.3 (2017), p. 032906 (cit. on p. 85).

[176] A Janda et al. “Jamming and critical outlet size in the discharge of a two-dimensional silo”. In: *EPL (Europhysics Letters)* 84.4 (2008), p. 44002 (cit. on pp. 85, 93).

[177] Yixian Zhou. “Ejection de gaz et de grains suite à la rupture d’un crayon de combustible nucléaire: modélisation de la dynamique”. PhD thesis. Aix-Marseille, 2016 (cit. on p. 85).

[178] Yann Bertho, Frédérique Giorgiutti-Dauphiné, and Jean-Pierre Hulin. “Dynamical Janssen effect on granular packing with moving walls”. In: *Physical review letters* 90.14 (2003), p. 144301 (cit. on p. 86).

[179] Christophe Perge et al. “Evolution of pressure profiles during the discharge of a silo”. In: *Physical Review E* 85.2 (2012), p. 021303 (cit. on p. 86).

[180] Marıa Alejandra Aguirre et al. “Granular flow through an aperture: Pressure and flow rate are independent”. In: *Physical Review E* 83.6 (2011), p. 061305 (cit. on p. 86).

[181] M Benyamine et al. “Discharge flow of a bidisperse granular media from a silo”. In: *Physical Review E* 90.3 (2014), p. 032201 (cit. on pp. 86, 88, 89).

[182] G Hagen. “Druck und Bewegung des trockenen Sandes”. In: *Berliner Monatsberichte Akad. D. Wiss.* (1852), s35–s42 (cit. on p. 86).

[183] Sachith Dunatunga and Ken Kamrin. “Continuum modelling and simulation of granular flows through their many phases”. In: *Journal of Fluid Mechanics* 779 (2015), pp. 483–513 (cit. on p. 86).

[184] Gilles Daviet and Florence Bertails-Descoubes. “Nonsmooth simulation of dense granular flows with pressure-dependent yield stress”. In: *Journal of Non-Newtonian Fluid Mechanics* 234 (2016), pp. 15–35 (cit. on p. 86).

[185] Mebirika Benyamine, Pascale Aussillous, and Blanche Dalloz-Dubrujeaud. “Discharge flow of a granular media from a silo: effect of the packing fraction and of the hopper angle”. In: *EPJ Web of Conferences*. Vol. 140. EDP Sciences. 2017, p. 03043 (cit. on pp. 89, 96, 105).

[186] Baptiste Percier. “Dynamique d’un empilement granulaire: instabilité de tôle ondulée et fluage d’une colonne de grains”. PhD thesis. Ecole normale supérieure de lyon-ENS LYON, 2013 (cit. on p. 89).

[187] Robert J Berry, Anthony H Birks, and Michael SA Bradley. "Arching behaviour of cohesive powders in a pilot-scale plane-flow silo". In: *Task Quarterly* 7.4 (2003), pp. 479–498 (cit. on p. 89).

[188] Antonio Cannavacciuolo et al. "Arch-Free flow in aerated silo discharge of cohesive powders". In: *powder Technology* 191.3 (2009), pp. 272–279 (cit. on p. 89).

[189] Eric Freyssingeas, M-J Dalbe, and J-C Géminard. "Flowers in flour: avalanches in cohesive granular matter". In: *Physical Review E* 83.5 (2011), p. 051307 (cit. on p. 89).

[190] Diego Barletta et al. "Solid flow rate prediction in silo discharge of aerated cohesive powders". In: *AIChE journal* 53.9 (2007), pp. 2240–2253 (cit. on p. 89).

[191] Lizhuo Zhu et al. "Hopper discharge of cohesive powders using pulsated airflow". In: *AIChE Journal* 66.7 (2020), p. 16240 (cit. on p. 89).

[192] GWJ Wes, S Stemerding, and DJ van Zuilichem. "Control of flow of cohesive powders by means of simultaneous aeration, and vibration". In: *Powder technology* 61.1 (1990), pp. 39–49 (cit. on p. 89).

[193] Gert Lube et al. "Collapses of two-dimensional granular columns". In: *Physical Review E* 72.4 (2005), p. 041301 (cit. on p. 106).

[194] C. Mériaux and T. Triantafillou. "Scaling the final deposits of dry cohesive granular columns after collapse and quasi-static fall". In: *Phys. Fluids* 20 (2008), p. 033301 (cit. on pp. 106, 109).

[195] L. Staron and E.J. Hinch. "Study of the collapse of granular columns using two-dimensional discrete-grain simulation." In: *J. Fluid Mech.* 545 (2005), pp. 1–27 (cit. on p. 106).

[196] Gert Lube et al. "Axisymmetric collapses of granular columns". In: *Journal of Fluid Mechanics* 508 (2004), p. 175 (cit. on p. 106).

[197] JM Warnett et al. "Scalings of axisymmetric granular column collapse". In: *Granular Matter* 16.1 (2014), pp. 115–124 (cit. on p. 106).

[198] Zhiqiang Lai et al. "Collapse of granular columns with fractal particle size distribution: Implications for understanding the role of small particles in granular flows". In: *Geophysical Research Letters* 44.24 (2017), pp. 12–181 (cit. on p. 106).

[199] Teng Man et al. "Finite Size Analysis of the Collapse of Axisymmetric Dry Granular Columns". In: *arXiv preprint arXiv:2012.03287* (2020) (cit. on p. 106).

[200] Xiaorong Xu et al. "Measurements of velocity and pressure of a collapsing granular pile". In: *Powder Technology* 303 (2016), pp. 147–155 (cit. on p. 107).

[201] Thanh-Trung Vo et al. "Evolution of wet agglomerates inside inertial shear flow of dry granular materials". In: *Physical Review E* 101.3 (2020), p. 032906 (cit. on p. 109).

[202] Joel Torres-Serra, E Romero, and Antonio Rodrıguez-Ferran. “A new column collapse apparatus for the characterisation of the flowability of granular materials”. In: *Powder Technology* 362 (2020), pp. 559–577 (cit. on p. 109).

[203] Anaıs Abramian, Lydie Staron, and Pierre-Yves Lagrée. “The slumping of a cohesive granular column: Continuum and discrete modeling”. In: *Journal of Rheology* 64.5 (2020), pp. 1227–1235 (cit. on p. 116).

[204] Frédéric Restagno, Lydéric Bocquet, and Elisabeth Charlaix. “Where does a cohesive granular heap break?” In: *The European Physical Journal E* 14.2 (2004), pp. 177–183 (cit. on pp. 117, 118, 133).

[205] Delwyn G Fredlund and J Krahn. “Comparison of slope stability methods of analysis”. In: *Canadian geotechnical journal* 14.3 (1977), pp. 429–439 (cit. on p. 117).

[206] Jian Chen, Jian-Hua Yin, and CF Lee. “Upper bound limit analysis of slope stability using rigid finite elements and nonlinear programming”. In: *Canadian Geotechnical Journal* 40.4 (2003), pp. 742–752 (cit. on p. 117).

[207] RL Michalowski. “Slope stability analysis: a kinematical approach”. In: *Geotechnique* 45.2 (1995), pp. 283–293 (cit. on p. 117).

[208] J Michael Duncan, Stephen G Wright, and Thomas L Brandon. *Soil strength and slope stability*. John Wiley & Sons, 2014 (cit. on p. 117).

[209] Ronald Midgley Nedderman. *Statics and kinematics of granular materials*. Cambridge University Press, 2005 (cit. on p. 118).

[210] Elliot J Fern and Kenichi Soga. “Granular column collapse of wet sand”. In: *Procedia Engineering* 175 (2017), pp. 14–20 (cit. on p. 118).

[211] Vincent J Langlois, Amélie Quiquerez, and Pascal Allemand. “Collapse of a two-dimensional brittle granular column: Implications for understanding dynamic rock fragmentation in a landslide”. In: *Journal of Geophysical Research: Earth Surface* 120.9 (2015), pp. 1866–1880 (cit. on p. 126).

[212] Zhong Zheng et al. “Flow of buoyant granular materials along a free surface”. In: (2018) (cit. on p. 127).

[213] Franco Tapia et al. “Rheology of concentrated suspensions of non-colloidal rigid fibres”. In: *Journal of Fluid Mechanics* 827 (2017) (cit. on pp. 139, 140).

[214] Franco Tapia, Olivier Pouliquen, and Élisabeth Guazzelli. “Influence of surface roughness on the rheology of immersed and dry frictional spheres”. In: *Physical Review Fluids* 4.10 (2019), p. 104302 (cit. on p. 139).

[215] M Trulsson, E DeGiuli, and M Wyart. “Effect of friction on dense suspension flows of hard particles”. In: *Physical Review E* 95.1 (2017), p. 012605 (cit. on p. 141).

[216] Richard Stribeck. “Die wesentlichen eigenschaften der gleit-und rollenlager”. In: *Zeitschrift des Vereines Deutscher Ingenieure* 46 (1902), pp. 1341–1348 (cit. on p. 143).

[217] Brian Armstrong-Helouvry. “Stick-slip arising from stribeck friction”. In: *Proceedings., IEEE International Conference on Robotics and Automation*. IEEE. 1990, pp. 1377–1382 (cit. on p. 143).

[218] Pierre Dupont, Brian Armstrong, and Vincent Hayward. “Elasto-plastic friction model: contact compliance and stiction”. In: *Proceedings of the 2000 American control conference. ACC (IEEE cat. no. 00CH36334)*. Vol. 2. IEEE. 2000, pp. 1072–1077 (cit. on p. 143).

[219] Joshua W Robinson et al. “Probing the molecular design of hyper-branched aryl polyesters towards lubricant applications”. In: *Scientific reports* 6.1 (2016), pp. 1–10 (cit. on p. 144).

[220] Stephan Herminghaus, Karin Jacobs, and Ralf Seemann. “Viscoelastic dynamics of polymer thin films and surfaces”. In: *The European Physical Journal E* 12.1 (2003), pp. 101–110 (cit. on p. 144).

[221] Oliver Bäumchen and Karin Jacobs. “Slip effects in polymer thin films”. In: *Journal of Physics: Condensed Matter* 22.3 (2009), p. 033102 (cit. on p. 144).

[222] Marceau Hénot et al. “Friction of polymers: from PDMS melts to PDMS elastomers”. In: *ACS Macro Letters* 7.1 (2018), pp. 112–115 (cit. on p. 144).

Appendix

Appendix A

Empirical measurements of powders

This Appendix present some usual measurements on dry and cohesive powders.

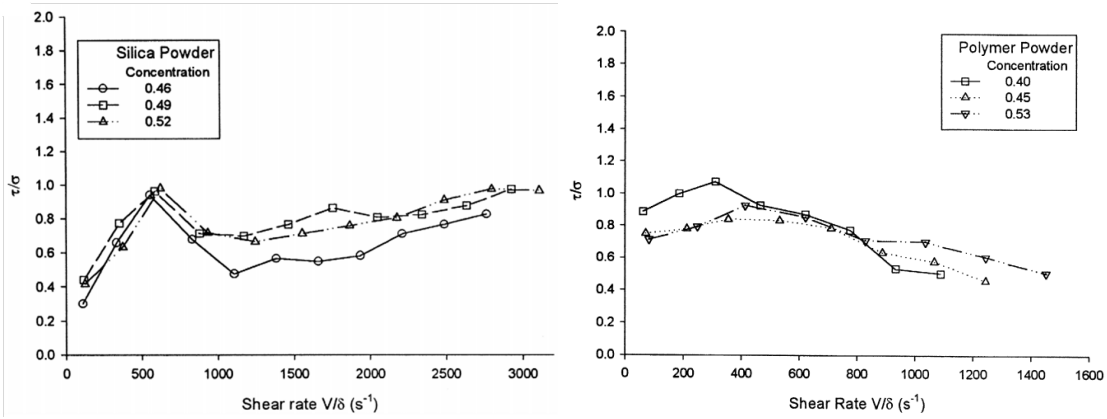

(a) (b)

Figure .1 – Ratio of the tangential stress over the normal stress τ/σ, as a function of the shear rate for (a) silica powder and (b) polymer powder, extracted from [75]

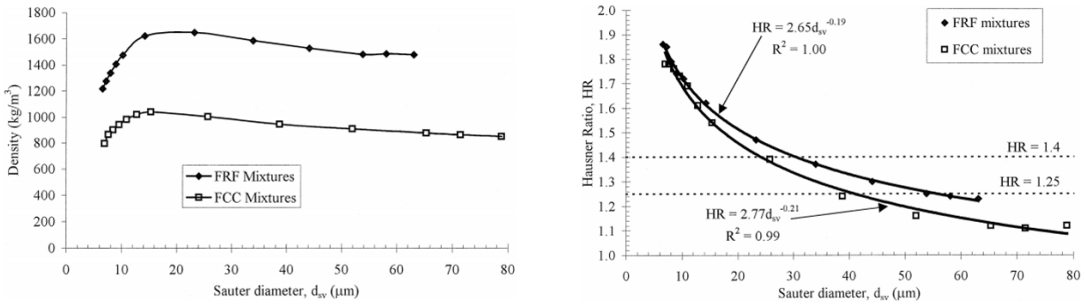

(a) (b)

Figure .2 – Tapped density (a) and Hausner ratio (b) as a function of the Sauter diameter for Fire Retardant Filler (FRF) powder and Fluid Cracking Catalyst (FCC) powder. Extracted from [76]

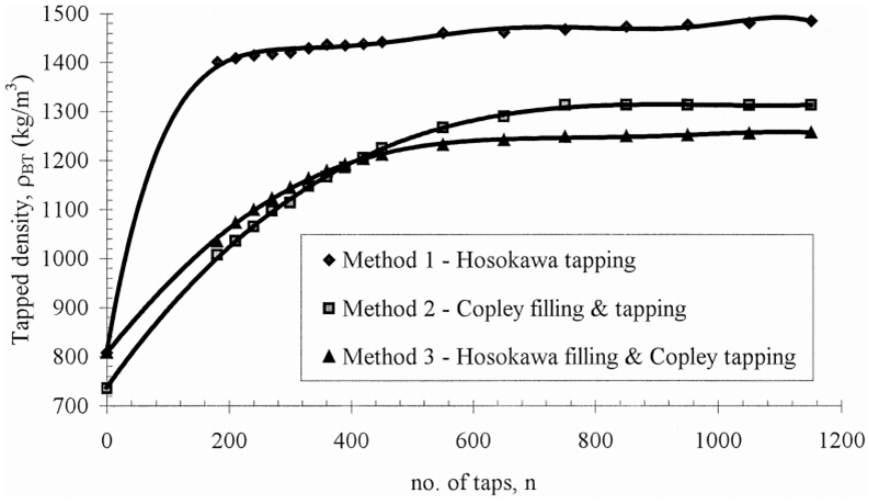

Figure .3 – Tapped density as a function of the number of taps for several tapping methods, using FRF powder.

Appendix B

Stability of a cohesive granular heap

As seen in chapter 5, the criterion of stability of a cohesive granular heap is :

$$f(\alpha) = \left(\frac{1}{\tan\alpha} - \frac{1}{\tan\theta}\right)(\sin\alpha - \tan\theta_c \cos\alpha)\sin\alpha \leq \frac{2\ell_c}{H}$$

Note that choosing $\theta = \pi/2$ gives the criterion on stability of a granular column.

In the following development, we rewrite the function f and calculate its maximum value.

$$\left(\frac{1}{\tan\alpha} - \frac{1}{\tan\theta}\right)(\sin\alpha - \tan\theta_c \cos\alpha)\sin\alpha \leq \frac{2\ell_c}{H}$$

$$\left(\frac{1}{\tan\alpha} - \frac{1}{\tan\theta}\right)(\sin\alpha - \tan\theta_c \cos\alpha)\sin\alpha\cos\theta_c\sin\theta \leq \frac{2\ell_c}{H}\cos\theta_c\sin\theta$$

$$\left[\cos\alpha - \frac{\sin\alpha}{\tan\theta} - \tan\theta_c\frac{\cos^2\alpha}{\sin\alpha} + \tan\theta_c\frac{\cos\alpha}{\tan\theta}\right]\sin\alpha\cos\theta_c\sin\theta \leq \frac{2\ell_c}{H}\cos\theta_c\sin\theta$$

$$\cos\alpha\sin\alpha\sin\theta\cos\theta_c - \sin^2\alpha\cos\theta\cos\theta_c - \sin\theta_c\sin\theta\cos^2\alpha + \sin\theta_c\cos\theta\cos\alpha\sin\alpha \leq \frac{2\ell_c}{H}\cos\theta_c\sin\theta$$

$$\cos\alpha\sin\alpha(\sin\theta\cos\theta_c + \sin\theta_c\cos\theta) - \left(\sin^2\alpha\cos\theta\cos\theta_c + \cos^2\alpha\sin\theta\sin\theta_c\right) \leq \frac{2\ell_c}{H}\cos\theta_c\sin\theta$$

$$\cos\alpha\sin\alpha\sin(\theta+\theta_c) - \left(\frac{1-\cos 2\alpha}{2}\cos\theta\cos\theta_c + \frac{1+\cos 2\alpha}{2}\sin\theta\sin\theta_c\right) \leq \frac{2\ell_c}{H}\cos\theta_c\sin\theta$$

$$\frac{1}{2}\sin 2\alpha\sin(\theta+\theta_c) - \frac{1}{2}\left[\cos\theta\cos\theta_c + \sin\theta\sin\theta_c + \cos 2\alpha(\sin\theta\sin\theta_c - \cos\theta\cos\theta_c)\right] \leq \frac{2\ell_c}{H}\cos\theta_c\sin\theta$$

$$\sin\alpha\sin(\theta+\theta_c) + \cos 2\alpha\cos(\theta+\theta_c) - \cos(\theta-\theta_c) \leq \frac{4\ell_c}{H}\cos\theta_c\sin\theta$$

$$\cos(2\alpha-\theta-\theta_c) - \cos(\theta-\theta_c) \leq \frac{4\ell_c}{H}\cos\theta_c\sin\theta$$

$$\sin(\alpha-\theta_c)\sin(\theta-\alpha) \leq \frac{2\ell_c}{H}\cos\theta_c\sin\theta$$

$$f(\alpha) = \frac{\sin(\alpha-\theta_c)\sin(\theta-\alpha)}{2\cos\theta_c\sin\theta} \leq \frac{\ell_c}{H}$$

The maximum value of f is reached for $\frac{\partial f}{\partial \alpha} = 0$.

$$\begin{aligned}
\cos(\alpha-\theta_c)\sin(\theta-\alpha)-\sin(\alpha-\theta_c)\cos(\theta-\alpha)&=0\\
\cos(\alpha-\theta_c)\sin(\theta-\alpha)&=\sin(\alpha-\theta_c)\cos(\theta-\alpha)\\
\cot\alpha-\theta_c&=\cot\theta-\alpha\\
\alpha-\theta_c&=\theta-\alpha\\
\alpha_m&=\frac{\theta+\theta_c}{2}
\end{aligned}$$

Note that choosing $\theta=\pi/2$ gives $\alpha_m=\theta_c/2+\pi/4$. For the specific case of $\theta=\pi/2$ the maximum limit of stability writes :

$$\frac{2\ell_c}{H}=\sin^2\alpha_m-\mu\cos\alpha_m\sin\alpha_m$$

In the following we rewrite this limit using $\alpha_m=\theta_c/2+\pi/4$

$$\begin{aligned}
H&=\frac{2\ell_c}{\cos\alpha\sin\alpha-\mu\cos^2\alpha}\\
H&=\frac{2\ell_c}{\cos\frac{1}{2}\left(\theta_c+\frac{\pi}{2}\right)\sin\frac{1}{2}\left(\theta_c+\frac{\pi}{2}\right)-\mu\cos^2\frac{1}{2}\left(\theta_c+\frac{\pi}{2}\right)}\\
H&=\frac{2\ell_c}{\frac{\sin\left(\theta_c+\frac{\pi}{2}\right)}{2}-\mu\cos^2\frac{1}{2}\left(\theta_c+\frac{\pi}{2}\right)}\\
H&=\frac{2\ell_c}{\frac{\cos\theta_c}{2}-\mu\frac{1+\cos\left(\theta_c+\frac{\pi}{2}\right)}{2}}\\
H&=\frac{4\ell_c}{\cos\theta_c+\mu\sin\theta_c-\mu}\\
H&=\frac{4\ell_c}{\cos\theta_c(1+\mu^2)-\mu}\\
H&=\frac{4\ell_c}{\frac{(1+\mu^2)}{\sqrt{1+\tan{\theta_c}^2}}-\mu}\\
H&=\frac{4\ell_c}{\sqrt{\mu^2+1}-\mu}
\end{aligned}$$

Then the maximum height for a stable cohesive granular column only depends on ℓ_c and μ.